Structural insights into selective autophagy and cellular membrane remodeling

Inaugural-Dissertation

zur Erlangung des Doktorgrades
der Mathematisch-Naturwissenschaftlichen Fakultät
der Heinrich-Heine-Universität Düsseldorf

vorgelegt von

Siavash Mostafavi
aus Teheran, Iran

Düsseldorf, August, 2022

aus dem Institut für Biologie
der Heinrich-Heine-Universität Düsseldorf

Gedruckt mit der Genehmigung der
Mathematisch-Naturwissenschaftlichen Fakultät der
Heinrich-Heine-Universität Düsseldorf

Berichterstatter:

1. Prof. Dr. Carsten Sachse

2. Prof. Dr. Gunnar Schröder

Tag der mündlichen Prüfung: 29/11/2022

Statutory declaration in accordance with Heinrich-Heine-Universität Düsseldorf doctoral regulations, PO § 5 section 1b; § 6 section 5:

Ich versichere an Eides Statt, dass die Dissertation von mir selbständig und ohne unzulässige fremde Hilfe unter Beachtung der „Grundsätze zur Sicherung guter wissenschaftlicher Praxis an der Heinrich-Heine-Universität Düsseldorf“ erstellt worden ist.

I swear under oath that the Dissertation has been written by me independently and without impermissible outside help in compliance with the "Principles for ensuring good scientific practice at Heinrich Heine University Dusseldorf”.

Acknowledgments

I would like to thank Prof. Dr. Carsten Sachse for his scientific mentorship, as well as providing the resources and vibrant environment in which to advance scientific knowledge. Despite the challenges of moving the lab to a new facility, and the challenges posed by a global pandemic, he made sure that the lab was always safe, and functional.

I would also like to thank Prof. Dr. Gunnar Schröder for serving as my mentor, as well as the entire Sachse lab for their years of advice and support. In particular I would like to thank Dr. Daniel Mann, whose efforts in setting up our computational resources were invaluable. In addition, I am thankful to Dr. Julio Ortiz and Dr. Thomas Heidler, who worked tirelessly to maintain our microscopes in working order. I would also like to thank Dr. Sabrina Berkamp and Dr. Benedikt Junglas for their scientific advice.

Moving to a new country for a PhD was not easy, and the advice and help from Lisa Jungbluth and Claire Ortmann de Percin in everyday matters was crucial, and for this, I am very thankful to them. I would like to thank Dr. Simon Mortensen, Nuno Bustorff, and Ilona Ritter for their personal and professional help.

Finally, I would like to thank my parents, Dr. Hamid Mostafavi and Dr. Batol Aleali for their lifelong support and encouragement.

Summary

In autophagy, large cellular debris is captured and packaged into membrane bound cellular structures called autophagosomes, after which it is shuttled to the lysosome or vacuole, degraded, and recycled. First, I set out to understand how autophagy cargo is specifically recognized by cellular receptors. Therefore, I determined a structure of the full length human selective autophagy receptor p62/SQSTM1. Second, I wanted to understand the structural mechanisms of membrane remodeling, a necessary process for many cellular functions including autophagy. Therefore, I focused on the yeast ESCRT pathway machinery involved in many membrane processes of the cell including autophagy and how ESCRT-III core proteins interact with each other and with membranes. The work carried out in the first part of this thesis has produced a high-resolution structure of full-length p62/SQSTM1 and shows that the protein assembles into a tubular helical scaffold with substantial flexibility. The filaments show local and global flexibility and show open and closed forms. While only the PB1 domain is well-resolved, the other domains appear as blobs or nonspecific density present on the inside of the tube. Experiments with p62 binding partners show that despite being buried inside the tube, the other domains are still available for interaction. In addition, the individual monomers of the filament may be able to dissociate and reassociate within the helical assembly. The work in the second part of this thesis has produced the first known structures of membranes remodeled by a protein coat consisting of yeast ESCRT-III complex subunits. In total, seven structures of the core ESCRT-III proteins bound to membranes show that the proteins form a coat around membranes and remodel them into tubular assemblies, a critical step in the function of the ESCRT-III complex. Furthermore, the structures show that by the addition or removal of protein subunits in the helical lattice, membranes remodeled into tubular structures can be effectively constricted down a width of less than 300 Å. Together, the determined structures of p62/SQSTM1 and ESCRT-III provide structural examples of active helical assemblies that perform important tasks in membrane trafficking processes such as autophagy and endocytosis.

Table of Contents

1 General Introduction

1.1 Autophagy

One of the most important functions in the eukaryotic cell is the regulated degradation of cellular objects and recycling of molecular building blocks. They can include misfolded proteins, damaged organelles, and intracellular pathogens [1]. This function is generally performed by two distinct, but not entirely independent pathways [2]. The first pathway is facilitated by the proteasome - a large protein complex that unfolds and degrades mostly soluble polypeptide substrates, while larger substrates must be removed through the autophagy pathway instead [3]. Autophagy, meaning 'self-eating', is a cellular process during which cargo is delivered to the lysosomes, where it is denatured due to the harsh environment of the lysosome, and subsequently degraded by a variety of enzymes [4]. Autophagy consists of three distinct forms [5]. The first, called microautophagy, is when a cargo is engulfed directly by the lysosomal membrane and digested [5]. The second type, called chaperone-mediated autophagy is when a protein is specifically recognized by a receptor and delivered to the lysosomal membrane, where it is unfolded and translocated into the lysosome by the LAMP2A protein [5]. The third type of autophagy, which is used for very large cargoes, such as organelles, protein aggregates, and intracellular pathogens is called macro-autophagy.

In this pathway, the cargo is engulfed by a double lipid membrane vesicle called an autophagosome [6]. The autophagosome is then transferred to the lysosome where the two organelle membranes fuse and the contents of the autophagosome are delivered into the lysosome [2]. Since it is the most common form of autophagy, from now on in this document, the word 'autophagy' refers specifically to macro-autophagy.

Autophagy is further divided into selective and bulk autophagy [4, 7]. In selective autophagy, specific cargo is recognized by a receptor and delivered to the lysosomes, whereas in bulk autophagy any cellular material present in that cytosolic region is encapsulated into an autophagosome and shuttled to the lysosome. Bulk autophagy processes have been experimentally studied by inducing starvation, or mimicking starvation

by the use of rapamycin, in yeast and mammalian cells [8]. In addition, the cytoplasm-to-vacuole (*Cvt)* pathway in yeast, which uses many of the same proteins involved in autophagy to deliver digestive enzymes encapsulated into so-called Cvt vesicles to the vacuole, has been used as an early experimental model system to study autophagy [8].

Autophagy is important for many cellular functions, such as the response to stress, survival or apoptosis, differentiation, and the response to extracellular signals, pathogens or starvation [4]. Consequently, malfunctions in autophagy can manifest as many different diseases such as cancer [9], inflammatory diseases [10], osteoarthritis [11], and neurodegenerative diseases [12]. For this reason, a complete understanding of the autophagy pathway, as well as the specific functions of each component is of fundamental importance.

1.1.1 The basic steps of autophagy

The autophagy pathway itself is usually described as having 5 distinct stages called nucleation, expansion, maturation, fusion, and recycling (Figure 1.1) [7]. In yeast, over forty individual gene products are known to be involved at various stages in the process, and many of these genes have conserved homologs in higher eukaryotes [13]. The functions of the various genes are summarized in a review by Suzuki, et. al 2010 [8]. A subset of these genes required for autophagosome biogenesis are called the core autophagy machinery [8]. The remaining genes are involved in specific types of autophagy such as mitophagy, ribophagy and the Cvt pathway [8].

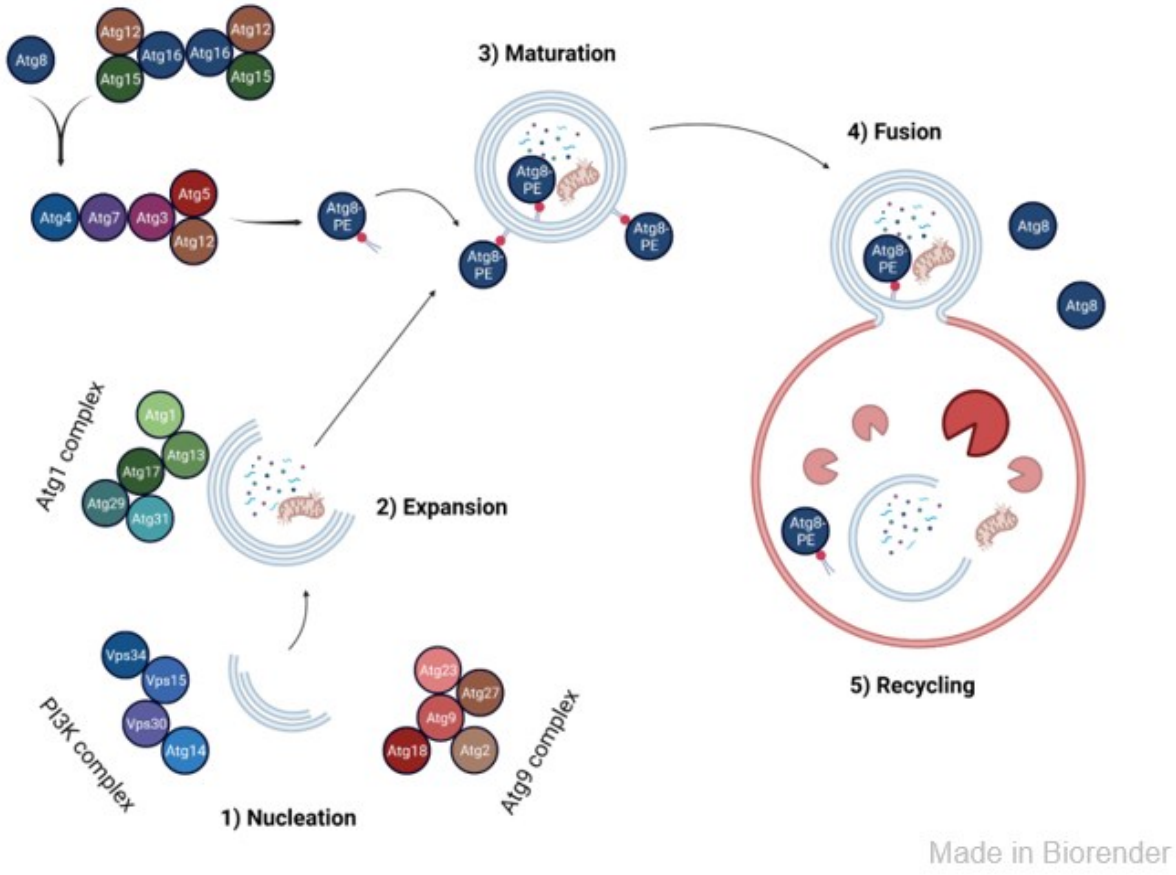

Figure 1.1: The five stages of autophagy
After triggering autophagy, an isolation membrane begins to form around cargo and is gradually expanded and decorated with autophagy proteins. The isolation membrane eventually closes to form an autophagosome. The *de novo* formed organelle is brought to the vacuole where the contents are degraded.

The first two steps in autophagy, nucleation and expansion, where a lipid membrane starts to form around the cargo, occurs at a specific cellular location in yeast called the pre-autophagosomal structure (PAS) [8]. In mammals, the PAS has not yet been identified, and it is possible that there are multiple nucleation points throughout the cell [14]. In both yeast and mammals, three groups of protein complexes are required for this process [15], and in yeast they are called the Atg1 complex (composed of Atg1, Atg13, Atg17, Atg29 and Atg31), the Atg9 complex (composed of Atg2, Atg9, Atg18, Atg23 and Atg27) and the PI3K complex (composed of Atg14, Vps15, Vps30 and Vps34). In addition, there are two protein conjugation complexes composed of Atg3/Atg7/Atg8 and Atg5/Atg12/Atg16 [8, 15] that

function together to covalently attach Atg8 to phosphatidylethanolamine to form Atg8-PE [8], and thus physically anchor Atg8 to the lipid membrane [16].

Under starvation conditions, Atg17 acts as a scaffold to recruit the remaining components of the Atg1 complex, however this function is replaced by Atg11 in the case of the Cvt pathway [8]. Atg13 is normally phosphorylated under nutrient rich conditions. When dephosphorylated it binds to Atg1 kinase, and this interaction upregulates the kinase activity of Atg1 [17]. Atg13 is also required for the recruitment of the PI3K complex, via its interaction with Atg14. In addition, Atg17 and Atg11 are both known to recruit Atg9 [8], a lipid scramblase that translocates lipids from the cytoplasmic to the luminal lipid layer of the isolation membrane [18]. The PI3K complex contains the kinase Vps34 that converts phosphatidylinositol into phosphatidylinositol-3 phosphate [13, 19], which is required for the recruitment of Atg18 [20] and the PI3P-binding protein Atg21. While Atg21 is responsible for the recruitment of the Atg5/Atg12/Atg16 complex through its interaction with Atg16 [21], Atg18, in turn, is bound to Atg2, which tethers the growing isolation membrane to the endoplasmic reticulum, and acts as a lipid transporter to supply lipids from the endoplasmic reticulum to the growing isolation membrane [22]. Atg12 is activated by the E1 ligase-like protein Atg7 [23], and conjugated to Atg5 by the E2-like protein Atg10 [24]. The Atg5-Atg12 complex then associates with the dimeric protein Atg16 [25]. Subsequently, Atg8 is conjugated to phosphatidylethanolamine by the serial reactions of Atg4, the E1-like protein Atg7, the E2-like protein Atg3 and finally by the Atg5-Atg12 complex, which acts as an E3-like conjugate [26]. Atg8-PE is then anchored to the membrane and is thought to be involved in autophagosomal membrane stabilization [27]. In yeast, the autophagosome is formed near the vacuole and does not need to be trafficked very far [13], however in mammalian cells where there are multiple nucleation points, the mammalian homolog of Atg8, called LC3, assists in the cellular trafficking by binding to microtubules [28]. Once the isolation membrane has formed around the cargo, it must then be sealed. This is performed by the ESCRT-III family of proteins [29], see the section below for more details.

The completion of this process is called maturation [7]. At this stage the cargo is fully engulfed in a vesicle and completely isolated from the rest of the cell [7]. The combination of the vesicle and the cargo is now called the autophagosome. Prior to fusion, the Atg proteins

decorating the autophagosome must first be dissociated and recycled [30]. This is thought to be driven by the deconjugation of phosphatidylethanolamine from Atg8-PE that faces the external surface of the autophagosome, which is performed by Atg4 [31], while Atg8-PE that was facing the autophagosomal lumen is degraded in the vacuole. In addition, the PI3P that was required for the recruitment of earlier Atg proteins must be removed for the maturation of the autophagosome [32]. This is mediated by the hydrolase Ymr1 [19].

In the fourth stage, fusion, the autophagosome is trafficked to the lysosome, or vacuole, and the outer membranes of the two begin to fuse, and the contents of the autophagosome are delivered to the inside of the lysosome [7]. This process is mediated by the Rab-like protein Ypt7 and its interaction homotypic vacuole fusion and protein sorting (HOPS) complex, and SNAREs [30]. The final stage, recycling, consists of the cargo being degraded by the lysosome [7].

1.1.2 Cargo recognition in selective autophagy

In contrast to bulk autophagy, in selective autophagy cargo receptors bind to cellular components, and subsequently recruit the autophagy machinery by binding to Atg8-family proteins or to the scaffolding protein Atg11 [33–36]. Selective autophagy can be active at basal levels, such as in the Cvt pathway in yeast [37], or it can be induced in response to internal or external stimuli such as infection by intracellular pathogens, or by oxidative, hypoxic or osmotic stress [38]. Examples of the types of cargo with known receptors include protein aggregates [39], ciliophagy [40], xenophagy [41], ER-phagy [42], mitophagy [43], nucleophagy [44], pexophagy [45] and ribophagy [46]. Some of these cargos are recognized directly by a receptor protein that binds to the target, such as Atg19 binding to prApe1 in the Cvt pathway [47], or through binding to ubiquitinated cargo via a ubiquitin binding domain as is the case in p62/SQSTM1 [48].

1.1.3 Membrane remodeling events during autophagy

After cargo recognition and sequestration, the formation of a membrane around the cargo requires the recruitment of membrane material to the autophagosome, as well as extensive membrane remodeling events such as fusion, constriction and fission. In yeast,

some of these functions are carried out by endosomal sorting complex required for transport (ESCRT) proteins. The ESCRT proteins are a family of evolutionarily conserved, eukaryotic [49, 50] protein complexes that are involved in cellular membrane remodeling events. The ESCRTs were initially discovered as proteins that recognize ubiquitinated cargo and facilitate their sorting into cellular structures called multivesicular bodies (MVBs) [51]. Multivesicular bodies are formed in the later stages of the endosome lifecycle, where the limiting membrane of the endosome invaginates and buds inwards towards the lumen of the endosome, forming an intraluminal vesicle (ILV) [52]. As the MBV is delivered to the lysosome, the contents inside the ILVs are degraded by the lysosome [52]. Since then, ESCRT family proteins have been implicated in many more cellular functions that require membrane remodeling, such as cytokinesis [53], membrane repair [54], vesicle budding [55], endosome formation and maturation [56], viral replication [57], and autophagy [58, 59]. Within the context of autophagy, ESCRT-III proteins are required for autophagosome sealing, and their depletion causes the accumulation of open autophagosomes inside cells [29, p. 5, 60].

1.2 Introduction to transmission electron microscopy

1.2.1 Basic setup of an electron microscope

Transmission electron microscopy (TEM) is a technique used for imaging of specimens using electrons instead of light. Due to the much shorter de Broglie wavelength of electrons, the level of detail that can be imaged using TEM is substantially greater than what can be achieved by light microscopy. Whereas light microscopes are limited to about 200 nanometer resolution, electrons accelerated to 200 KeV have a wavelength of 2.5 picometers and a practical resolution limit of 40 picometers [61].

There are some key differences between light and electron microscope. First, the electron beam path must be in high vacuum in order to prevent the interaction of the electrons with air [62]. Second, the lenses used in an electron microscope are circular magnets that can alter the electron path by modulating a magnetic field. Lastly, the detection of electrons must be done by either photographic film, a fluorescent screen, or through a direct electron detector [63]. The basic principles of operation aside from those differences are

similar to a light microscope. Electrons are generated by an electron gun, then pass through a successive series of charged plates that accelerate them to the desired voltage, typically 100-300 KeV [64]. The electron beam is then focused onto the sample using a pair of condenser lenses, which are circle-shaped magnets that can alter the path of electrons by modulating a magnetic field. The beam then passes through an objective lens that forms the first image, followed by a projection lens, which magnifies the image and projects it onto a detector [63].

Image formation happens through the interaction of the electrons with the sample. When an electron hits the sample, one of four potential things can happen. First, the electron could pass though without any interaction. Second, it could be scattered elastically, meaning the path changes but the electron does not lose energy. Third, it could be scattered inelastically, meaning it will change its path as well as lose some energy, or forth, it can be absorbed by the sample [65]. These interactions with the sample give rise to two ways in which contrast is formed, amplitude contrast, which is due to the number of electrons hitting the detector after some have been absorbed or inelastically scattered, or phase contrast, which is due to electrons interacting with each other due to having different phases before they hit the detector [66]. Due to the fact that more electrons interact with a sample as the thickness increases, there is generally a need to keep the sample quite thin, ideally less than 100 nanometers [67].

1.2.2 Electron microscopy for biological samples

Biological samples present special challenges for electron microscopy. First, they are made of relatively light atoms that will have poor amplitude contrast under an electron beam. Second, they are relatively fragile and radiation damage can happen quickly even with low electron doses [66]. There are several approaches to overcome these issues. To increase contrast and radiation resistance, biological samples can be negatively stained using heavy atoms [68]. In negative staining, the sample is deposited onto a grid, and a solution typically containing uranyl acetate is added to the sample and allowed to incubate before being removed. The uranyl acetate stain forms a shell around each particle, e.g., a protein, and due to the heavy uranium atoms, this shell inelastically scatters or absorbs many electrons and

thus significantly increases amplitude contrast [68]. There are drawbacks however, since the actual object being imaged is only the outline of the actual sample, high resolution information is lost, and the resolution typically does not extend past 20 Å [68]. In addition, the process of negatively staining the sample can change the shape of the molecule since it is no longer hydrated, leading to artifacts of larger objects such as viruses or liposomes to collapse under their own weight.

An alternative approach is cryo-EM, in which the sample is frozen in vitreous ice (i.e., non-crystalline and amorphous) and kept at cryogenic temperatures typically below 110 °K. In order to freeze the sample and ensure that the ice formed is vitreous, the freezing must be performed very quickly, at about 1 x 10^4 to 1 x 10^6 °K per second [66]. To achieve this, 2-5 µL of the sample is added to a grid, excess liquid is removed by blotting to produce a thin sample, and the grid is quickly plunged into a pool of liquid ethane [66]. This procedure is typically automated using a Vitrobot (Thermo Fisher scientific), which provides a temperature and humidity-controlled sample chamber to prevent excessive liquid evaporation from the sample leading to sample drying or increases in ionic strength, as well as automated blotting and plunging to improve reproducibility.

Samples embedded in vitreous ice suffer from less radiation damage of the electron beam. However, they remain fragile and require low electron doses, and they still give rise to low contrast. To improve the contrast during imaging, a defocus is typically applied to the sample [69], however this leads to alterations in the image which are present in the power spectra of micrographs in the form of Thon rings (Figure 1.2). These are described by the contrast transfer function (CTF) of the microscope [70]:

$$\mathrm{CTF}\,(r) \;=\; -\sin\left(\frac{\pi}{2} C_s \lambda^3 r^4 \;+\; \pi f \lambda r^2\right) \qquad (1)$$

The CTF is a function that describes the distortions applied to the image as a function of r, the spatial frequency, and is affected by C_s, which is the spherical aberration arising from lens imperfections, λ, the electron wavelength, and f, the defocus value applied (Figure 1.2). The CTF can be described as a scalar function that is multiplied by the Fourier transform of the image. The CTF is a function that oscillates between -1 and 1 (phase reversal leading to contrast inversion) and crosses zero several times (thus leading to loss of contrast and

information), while gradually attenuating towards the higher spatial frequencies [70]. In a perfect microscope the CTF would be a straight line at 1.0, and in a real-world microscope the oscillatory effect of the CTF can be minimized by collecting the micrograph closer to focus, however this leads to lower contrast and the image is too noisy to be useful [71]. In order to reduce the information loss due to the CTF, several corrections can be applied. First, images should be collected at different defocus values in order to compensate for information loss where the CTF crosses zero on another micrograph [72]. Second, a Wiener filter is applied to the data. Initially in this process, the Fourier transform of the image is multiplied by the CTF. Since the original image was already multiplied by the CTF, multiplying it again by the CTF leads to the negative phases to be turned positive. The Fourier transform is then divided by CTF^2 including a Wiener constant, theoretically approaching closely to the reconstruction of the original image [73]. One additional correction must still be applied to account for the overall signal attenuation at higher frequencies, this is done through multiplying higher frequency information by a B-factor [74].

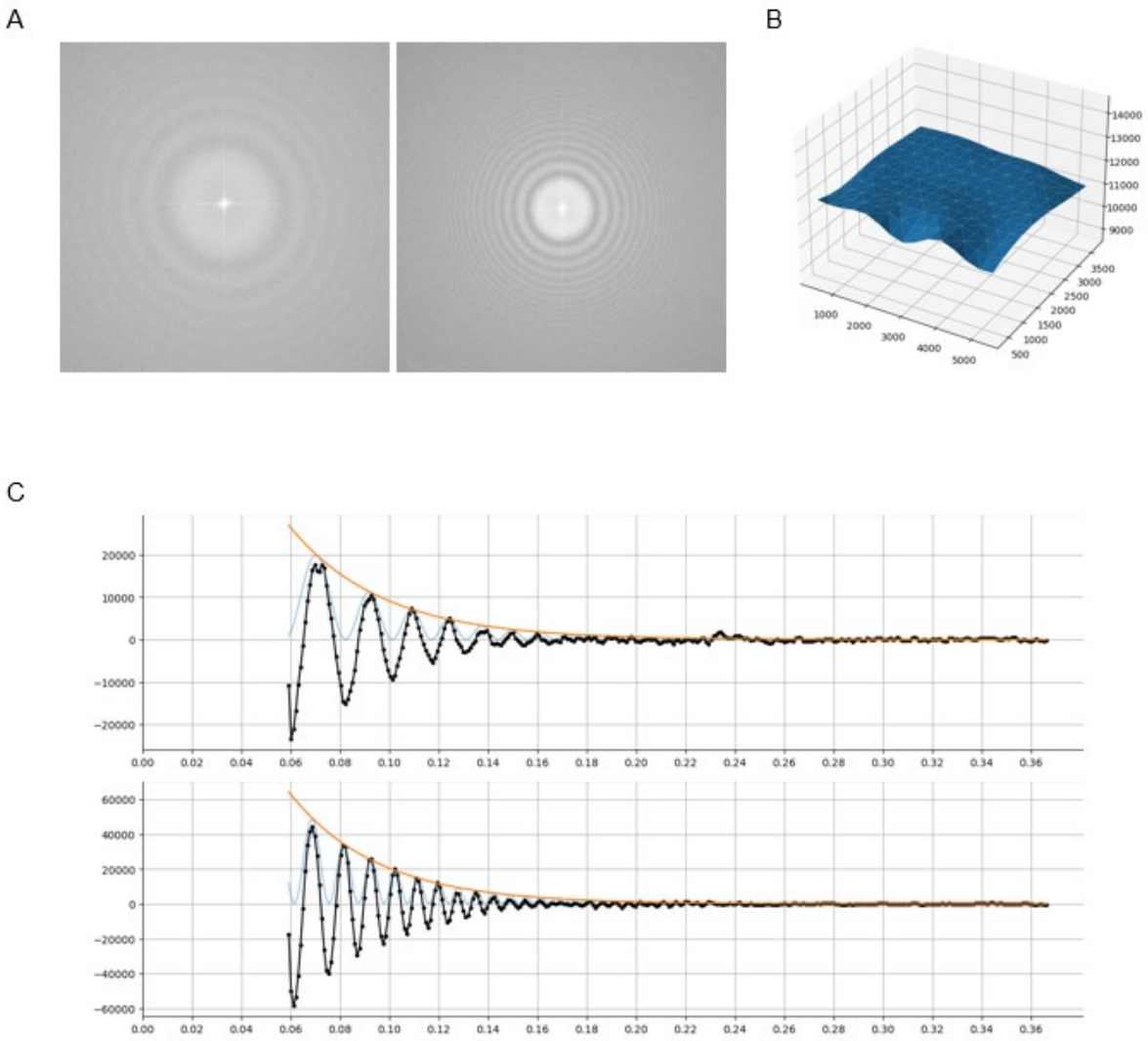

Figure 1.2: Defocus and CTF
(A) Power spectra of two micrographs collected at 1 µm defocus (left) and 2.5 µm (right), showing the effect of defocus on the Thon rings. (B) Since the objects generating contrast are often located within different heights in the ice, as well as the uneven thickness of the ice, modern CTF estimation algorithms such as 'Patch CTF' in CryoSPARC, break up each micrograph into smaller patches and perform local CTF estimation on those patches. (C) The CTF of a micrograph with low defocus (top) and high defocus (bottom) plotted as a function of contrast (and thus information) present in the power spectrum on the Y-axis, against spatial resolution on the X-axis. The graph clearly shows resolution dependent contrast inversion and information loss at points where the CTF crosses zero. By collecting a dataset with different defocus values, the effect of this information loss can be compensated.

While introducing a defocus improves contrast, the electron doses used are still low and the images obtained are noisy. In order to improve the signal to noise ratio, the detection

system for electrons must be very sensitive. The quality of a detector in distinguishing signal from noise as a function of spatial frequency is described by the detective quantum efficiency (DQE) [75]. In the past, the detectors used for electrons included photographic film, fluorescent screens, and charged couple detectors (CCD) [75]. These detection methods suffer from low DQE due to low sensitivity, the introduction of noise from the detector itself, and additional noise from electron backscattering. In addition, slow detection is of particular concern since samples embedded in ice can move in response to interaction with the beam, as well as from vibrations present on the microscope stage [76]. Recent technological advances have allowed the use of direct electron detectors, that have substantially improved DQE as well as faster imaging, which allows movies comprised of 20-40 frames to be collected. The frames can then be aligned [69] using motion correction algorithms present in pre-processing software packages such as CryoSPARC [77], WARP [78], or RELION [79].

Despite the improved radiation resistance and contrast afforded by the use of cryogenic temperatures, defocused data collection followed by CTF correction, and improved detectors, biological samples still have very low contrast. In order to overcome this issue, many images of the sample are collected and averaged in order to improve the signal to noise ratio. In addition, since the images obtained by cryo-EM are 2D projections of 3D molecules, collecting many images that contain different views of the sample is critical for reconstruction of a 3D volume. This reconstruction is based on the Fourier slice theorem [62], stating that a single slice through the 3D Fourier transform of an object represents a single 2D projection of that object. The algorithms used for reconstruction generally go through an iterative process where the Fourier transform of each 2D projection is matched to a slice in the 3D Fourier transform of a model to determine its orientation and alignment also known as projection matching, followed by the averaging of signal from many particles from each orientation, leading to a final high-resolution reconstruction [62].

1.2.3 Single particle analysis for reconstruction of biological samples

Following the collection of a dataset consisting of several hundred to several thousand motion-corrected, CTF-estimated micrographs, the next step is picking the locations within each micrograph that contain particles of interest. These particles can either

be picked manually or automatically using blob picking, template matching, or neural networks present in a variety of cryo-EM data processing packages [80]. After the particle locations within each micrograph are selected, smaller boxes that are typically about twice the size of the particle are extracted from the micrographs and subjected to 2D classification. The aim of 2D classification is to discard incorrectly selected particles such as containing, for example ice contamination, as well as assess the overall quality of the dataset. In general, if 2D classes show features consistent with secondary structure such as α-helices or β-sheets, there is a good chance that a high-resolution structure reconstruction will be successful [81]. In addition, 2D classification allows the dataset to be separated based on structural heterogeneity [81, 82]. Since the final reconstruction will be an average of all of the particles used, any heterogeneity deteriorates the resolution of the final reconstruction. After 2D classification, the particles are typically used for the generation of an initial, low resolution 3D model, or the initial model may be generated from a similar protein with a previously determined structure. The quality of the initial model is critical due to the dependence of the reconstruction algorithms on projection matching [81], and it is also important that the model not does have any high-resolution features which may lead to overfitting. After initial model generation, the particles are typically classified in 3D in order to obtain a more homogeneous particle pool [79, 81]. This final particle pool is then used for the final reconstruction of a volume. Typically, the particle pool is divided into two halves and the reconstruction is performed separately for each half in order to prevent overfitting [83]. The final resolution is estimated from the Fourier shell correlation (FSC) between the two halves, with a typical cutoff of either 0.143 or 0.5 [83]. During the 2D and 3D classification, as well as the final refinement, the particle averages are CTF corrected by the Wiener filter, however they still suffer from spatial resolution dependent contrast attenuation. This is present in the final reconstruction as a smearing of high-resolution features, and thus the final map must be sharpened by B-factor multiplication [74], typically between -100 to -1000 Å^2. In addition, the CTF estimation was performed on the whole micrograph, while individual particles may have slightly different CTFs due to their specific location in the Z axis in the ice, as well as slightly different local motion trajectories, and at this stage a per-particle CTF estimation as well as local motion correction can be performed.

1.2.4 Helical reconstruction

Helical symmetry is a special type of geometric assembly present in many viral capsids [84], cytoskeletal protein complexes [85] and other helical protein assemblies such as ESCRT-III complexes [86] and p62/SQSTM1 [48]. Complexes with helical symmetry are generally composed of one or more repeating units arranged in a tubular or filamentous assembly [87]. Complexes possessing helical symmetry offer a special advantage in cryo-EM, because each tube or filament has many different views of the repeating subunits [87]. Helical symmetry is usually defined using one of two sets of parameters, pitch, and the number of units per turn, or helical rise and twist. The pitch of a helix is the distance along the Z axis between two subunits that have the same orientation, while the number of units per turn is the number of repeating subunits present in this distance. On the other hand, helical rise is the distance between two subsequent subunits in the helix along the helical axis, and the twist is the rotation between the two subunits (Figure 1.3A). Each set of parameters can fully describe the helical symmetry present, and they can be interconverted [87]. There are two main approaches for helical reconstruction, the older Fourier-Bessel reconstruction that relies on Fourier space indexing, and the later real space methods such as IHRSR and derivatives of it.

1.2.4.1 Symmetry determination

In order for a 3D reconstruction to be successful, it is critical that the correct helical symmetry parameters are determined. There are a variety of approaches to this, only one of which may be successful for any given helical assembly. The first approach is by indexing the layer lines as implemented in PyHI [88], which are analogous to the diffraction spots in the Fourier spectra of a 2D crystal, but instead of single points, they are a series of parallel streaked lines (Figure 1.3B). Since the 2D projection of a 3D helical lattice contains both the front and rear subunits, the Fourier spectra also shows two sets of layer lines that are mirror symmetric along the meridian, or the vertical axis in the Fourier spectra [87]. Each layer line has a height along the vertical axis, h, and is assigned a number, l. The distance between each layer line along the meridian is the reciprocal distance of the helical repeat c, which can be, though not always, the same as the pitch. The distance between the first peak in each layer

line from the meridian as well as the streaking pattern are described by oscillating Bessel functions $J_v(X)$ of integer orders v, as a function of the helical radius r and the reciprocal radius R [87].

$$J_v(2\pi * R * r) \qquad (2)$$

After assigning a Bessel order and layer line height for each layer line, they can be plotted as a series of real space helical waves, and the intersections of these waves defines the subunit positions in the helical array [87]. In a real-world setting, however, cryo-EM images of helical assemblies suffer from high background noise, potentially overlapping layer lines, layer lines with high Bessel orders that are difficult to properly index, and misleading layer line positions due to in-plane tilt of the helix within the ice [87]. For these reasons, it can be difficult or even impossible to analytically index some helical lattices.

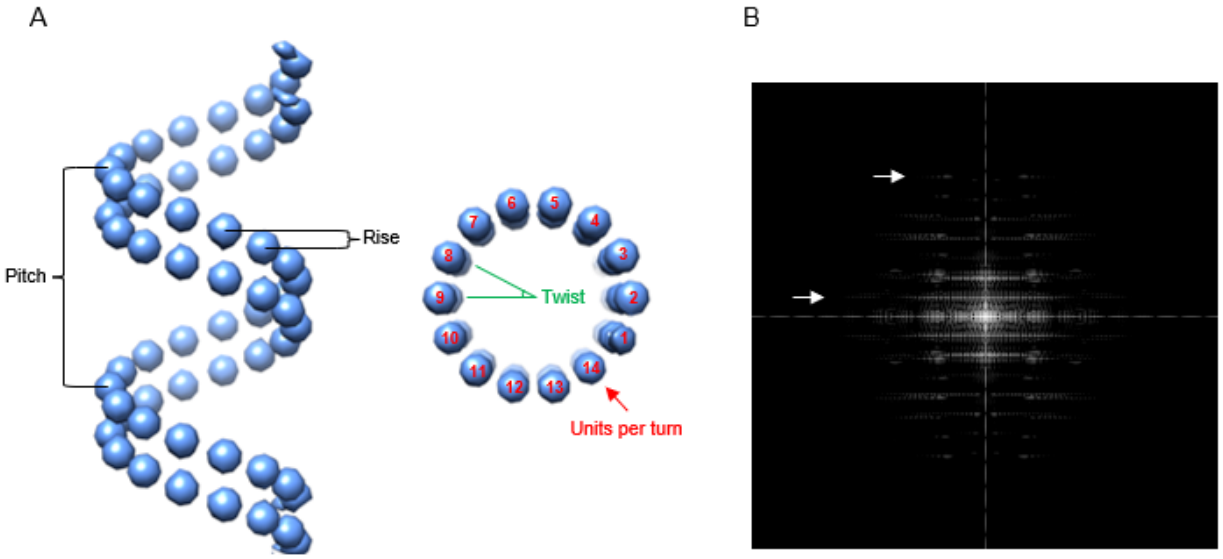

Figure 1.3: Definition of helical symmetry
(A) The helical symmetry parameters rise and twist describe the inter-subunit distance and rotation, respectively. The helical symmetry can also be expressed in terms of pitch and number of units per turn, which describe the distance between two subunits that are in the same position except a translation parallel to the helical axis. (B) The Fourier power spectra of a helical assembly shows reflections present as streaked lines with different maxima and different distance to the meridian from the first peak (Y-Axis), two such lines are indicated by arrows.

A second approach to determining symmetry parameters involves low resolution reconstructions of the helix without symmetry imposition using either real space reconstruction methods or sub-tomogram averaging, followed by manual determination of the symmetry parameters in real space. Both of these methods have the advantage that they do not require the indexing of the layer lines, however both of these methods can fail if the individual subunits are too small to allow proper alignment [87]. The third approach, as implemented in the software package SPRING [89], involves the 3D reconstruction of many potential symmetrized volumes from a single 2D class average with different symmetry candidates imposed, and the subsequent comparison of the 2D projection of the 3D reconstructions with the original 2D class average. This method will generally produce several potential symmetry candidates that must all be tested individually for a high-resolution reconstruction. Symmetry determination presents the most significant obstacle for helical reconstruction methods, since the imposition of the incorrect symmetry can lead to structures that converge to medium resolution but are completely incorrect [90]. For this reason, generally a symmetry candidate can not be considered correct unless side chain density, or at the very least convincing secondary structure can be validated in the final reconstruction.

1.2.4.2 High-resolution helical reconstruction using single particle methods

Once helical symmetry parameters have been determined, a variety of software packages including SPRING [89], RELION [79] or CryoSPARC [77] can be used for single particle-like reconstruction (Figure 1.4). In this method, individual overlapping segments of each helix present in the micrograph are selected and extracted, typically with a 90% overlap in each segment. The segments are then treated similarly to single particles extracted and can be subjected to 2D and 3D classification. For refinement, the particles are split into two independent halves, and then used in a projection matching procedure against 2D reprojections of a 3D initial model, which can be a low-resolution reconstruction, a stimulated helical lattice or even a featureless cylinder. Since each segment contains all views of the subunits (except the top view), this allows the determination of five alignment parameters for each segment, the x and y translation, the out of plane tilt, the in-plane

rotation, and the azimuthal angular orientation [87]. After the alignment of each overlapping segment, the helical symmetry parameters are used to multiply the contribution of each segment by the number of 'new' asymmetric units present in the inter-box distance, offset by a rise and twist value that correspond to the symmetry parameters. Since many helical assemblies are flexible and not perfectly straight (thus breaking symmetry), generally only the central portion of each extracted segment combined with a local search of symmetry parameters is used for this symmetry imposition step. This process is repeated until the reconstruction has converged for the two halves [91].

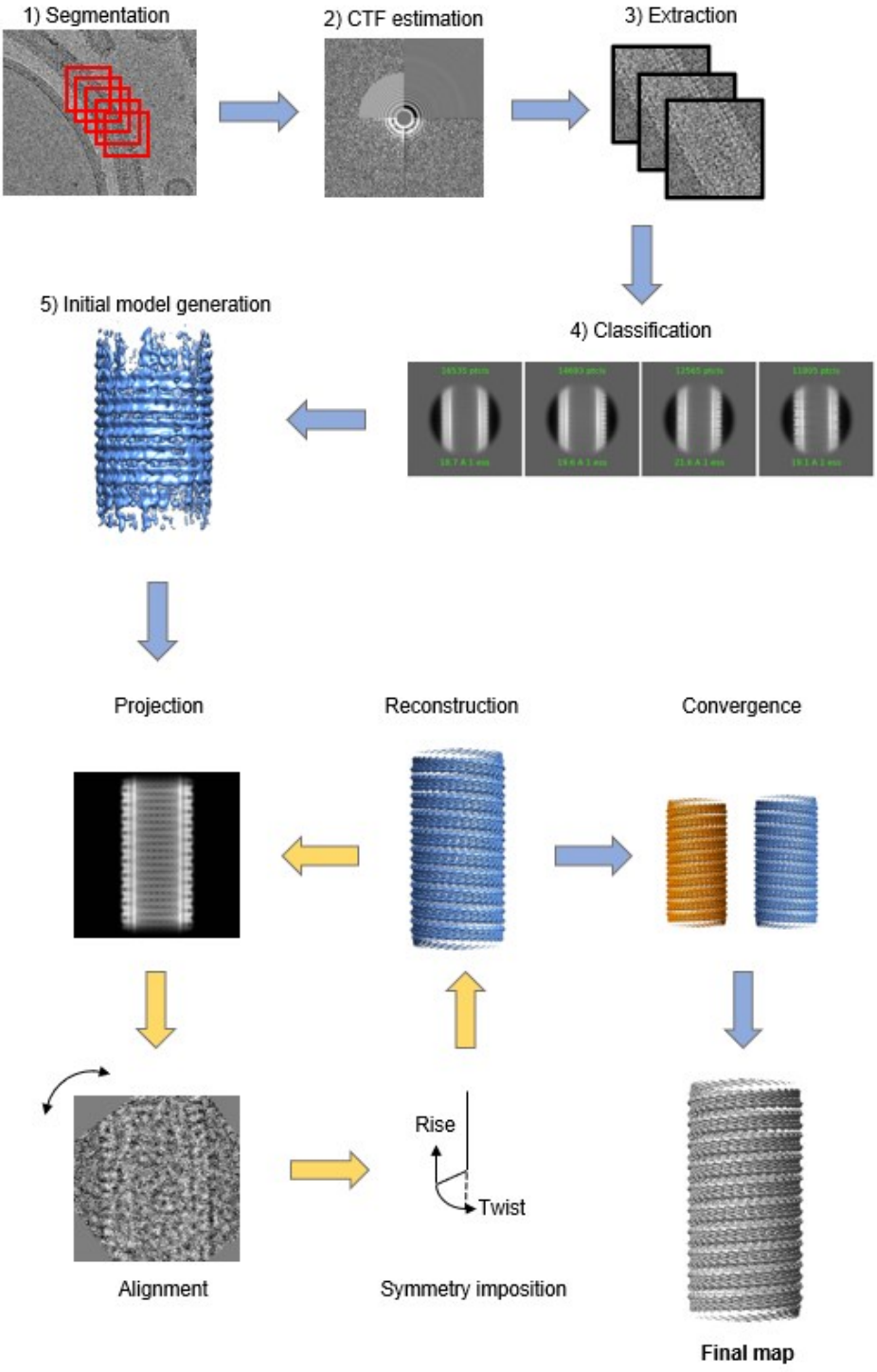

Figure 1.4: Helical reconstruction pipeline
In helical reconstruction, overlapping segments of each helix from the micrographs are selected and extracted. In parallel the CTF is estimated. The segments are then aligned and classified to remove unwanted particles or contamination, and to obtain a homogeneous particle pool. Either these particles, or another method such as a featureless cylinder or

simulated helical lattice, is used to generate a 3D initial model. The segments are then separated into two independent halves, and the following steps are performed for each half independently. The initial model is projected into a 2D alignment scaffold against which the particles are aligned. After alignment, the symmetry parameters are imposed in Fourier space. The aligned segments are then used to reconstruct the next iteration of the map that can be symmetrized in real space. This process is repeated until the two half maps have converged and the resolution has stopped improving. The two half maps are then combined to yield a final map. This map is then post-processed to sharpen it and improve the clarity of high-resolution information that can be visualized.

2 Aims

The overall goal of the PhD work was to study and structurally characterize protein assemblies involved in selective autophagy. An important component of selective autophagy are autophagy receptors such as p62/SQSTM1 [4]. Thus, the goal of the first portion of the PhD work was the determination of a full-length structure of p62/SQSTM1, a protein that contains numerous binding motifs and domains and acts as a multifunctional hub of cargo recognition [92]. In addition, the characterization of the interaction between p62 filaments with various binding partners involved in autophagy was pursued.

Another important aspect of autophagy is the packing of autophagic cargo into membrane-bound cellular bodies [7]. After cargo recognition and sequestration, the autophagic cargo must be encapsulated into membrane-bound cellular structures such as autophagosomes. This encapsulation process involves extensive recruitment and remodeling of subcellular membranes [56]. In yeast, this function is carried out, in part, by the ESCRT-III family of proteins [86]. The exact structural details of these remodeling events are not fully known, and there is no structure of a yeast ESCRT-III subunit interacting with a membrane. The goal of this part of the PhD work was to capture a structural snapshot of the interaction of ESCRT-III subunits with membranes.

For all structural studies in this thesis, Cryo-electron microscopy was used for data collection, followed by helical processing for structure determination. A variety of biochemical methods, as well as negative-staining electron microscopy, were used to elucidate protein-protein and protein-lipid interactions for both p62/SQSTM1 and the ESCRT-III complex.

3 The autophagy receptor p62/SQSTM1 and selective autophagy

3.1 Introduction

Note: Some of the figures in this section were taken from the publication [92]. All of these figures were prepared by me, and they are indicated by a star (*) sign in the figure legend. The article was published under the Creative Commons Attribution 4.0 International License (https://creativecommons.org/licenses/by/4.0/).

p62 is a multidomain, multifunctional human protein involved in many of the steps in autophagy. Its main functions are cargo recognition and membrane scaffolding [10]. The protein contains 3 structurally ordered domains, a PB1 domain, a ZZ domain and a ubiquitin binding domain (Figure 3.1). In addition, it contains short sequences that can bind to various other proteins. The protein is known to form filamentous tubes *in vitro* [10] and is known to co-localize along with autophagy cargoes inside cells in larger clusters called p62 bodies [93]. There is some evidence that the filamentous form exists inside neurons in a mouse model with impaired autophagy [94], as well as in RPE-1 cells [48].

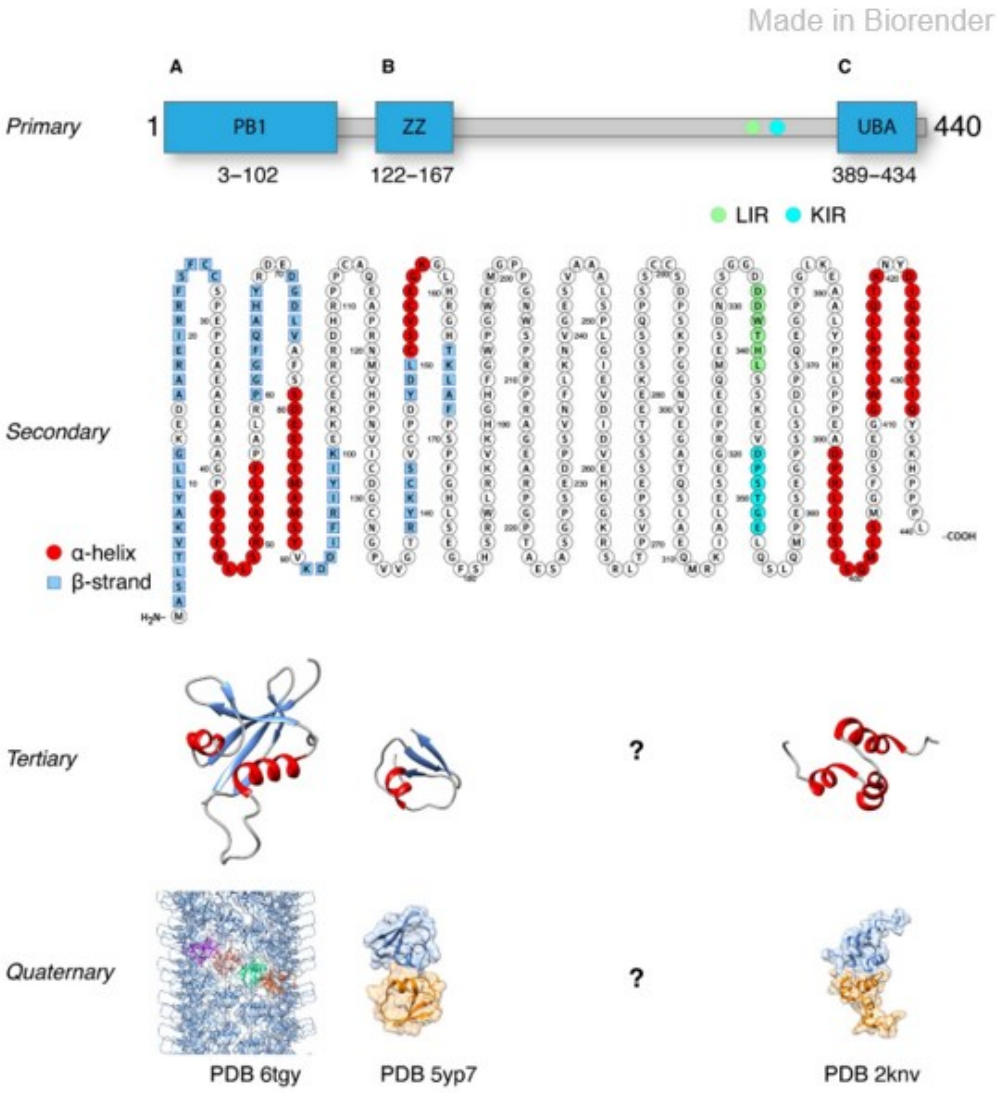

Figure 3.1*: Overall structural view of p62
The three folded domains of p62 include the PB1 domain (A, PDB ID 6TGY), the ZZ domain (B, PDB ID 5YP7), and the UBA domain (C, PDB ID 2KNV). The structures of these domains have been solved using a variety of methods, including cryo-EM, NMR and X-ray crystallography. All of these domains also form oligomeric structures, with the PB1 domain forming helical assemblies, and the ZZ and UBA domains forming dimers. *Note: This figure was taken, in unmodified form, from Fig. 1 in [92], in which I am co-author. The original figure was prepared by me.*

The PB1 domain of p62, which consists of residues 1-102, is part of a larger family of such domains that are present in a number of other proteins [95]. The PB1 domain in general consists of a ubiquitin-like fold and has two surface patches on opposite sides that can be both acidic, both basic, or one acidic and one basic [95]. This charged surface allows PB1 domains to dimerize or multimerize depending on their type [95]. In the case of p62, the PB1 domain contains an acidic and a basic surface that drives polymerization into long, filamentous structures that can adopt several polymorphs as shown by several experimentally determined structures (Figure 3.2) [10, 48, 95]. In addition, these filaments can be 'capped' at either end by other PB1 domain containing proteins, such as PKCs, MEKKs or NBR1 [48]. The ability of p62 to form filaments is critical for its function in the cell, since mutations that prevent this polymerization lead to a lack of p62 localization to the autophagosomal formation site [96].

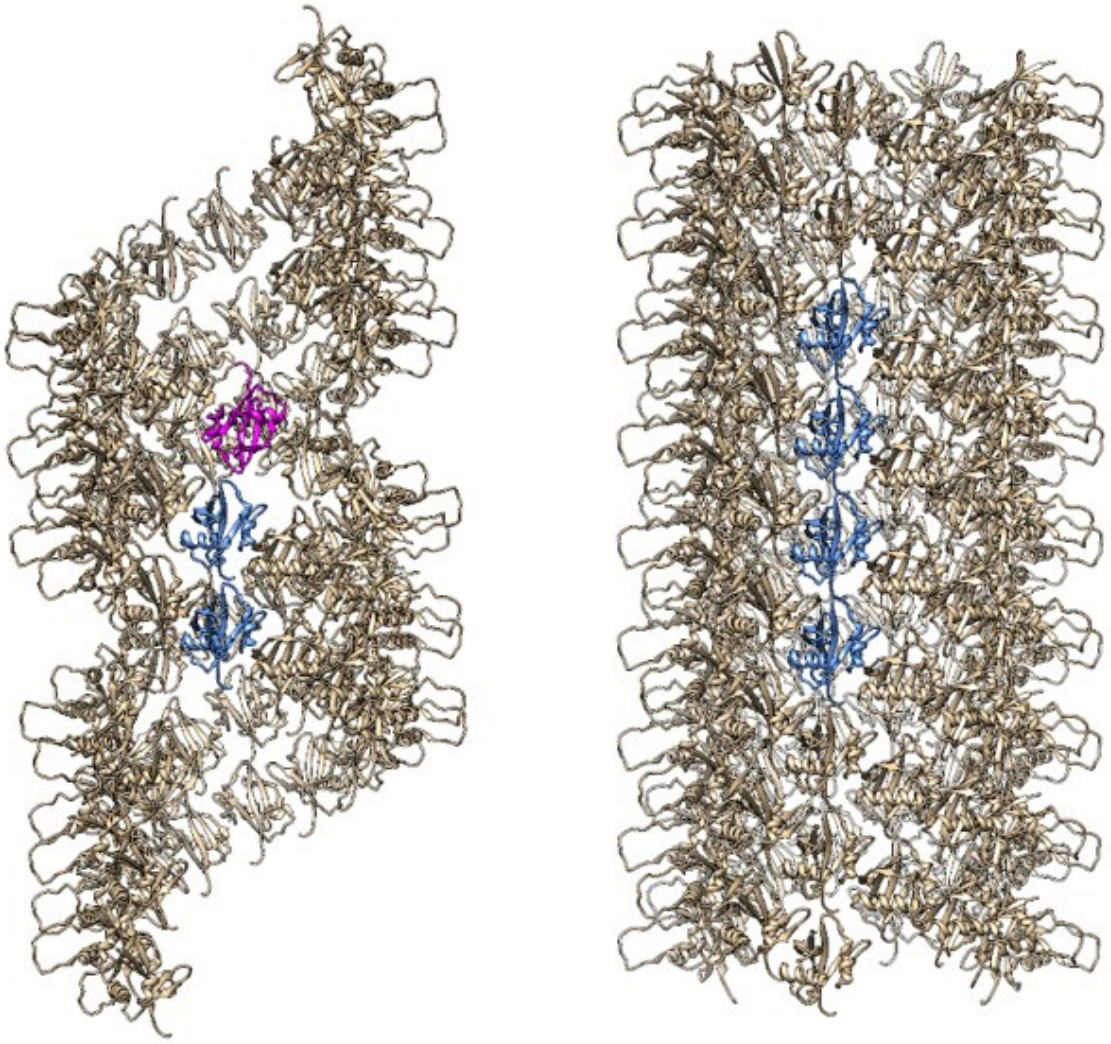

Figure 3.2: Known architectures of PB1-domain p62 polymers
The PB1 domain of p62 can form homo-polymers consisting of either three (left, PDB ID 6TH3) or four strands (right 6TGY). In the three stranded structure, there are two strands that run parallel to each other, in blue, and one strand that runs anti-parallel, in magenta. In the four stranded structure, all four strands run parallel to each other.

The N-terminal PB1 domain is followed by a 22-amino acid linker region that is thought to stabilize the filamentous form of the protein [10]. The linker region also contains two cysteine residues that are implicated in the sensing and response to oxidative stress [97]. Following this linker region, there is a 47-residue long ZZ domain. The ZZ domain is known to bind to the RIP1 protein [98]. The ZZ-domain is also known to bind to N-terminally

arginylated substrates which promote its aggregation [99]. The ZZ domain also interacts with vault RNAs, and this interaction is a negative regulator of autophagy in cells [100].

After the ZZ domain there is a large region without any known structure that contains binding sites for many proteins such as RAPTOR [101], TRAF6, Keap1, and LC3 [4, 102]. It is thought that one of the functions of p62 is to bind to and bring various proteins close together so that they can interact [102]. The C-terminal end contains a ubiquitin binding domain (UBA) which is thought to recognize cargo destined for lysosomal destruction, as well as promoting phase separation and the formation of p62 bodies [103]. The binding of free polyubiquitin to the UBA domain destabilizes the filaments formed by p62 [10], however triple ubiquitinated model cargo induces the cross-linking and formation of condensates [104].

3.1.1 Interactions of p62

The selective autophagy-related functions of p62 are ultimately dependent on its LC3 binding domain [4], mediated by its LIR domain consisting of the conserved motif (W/F/Y)-X-X-(L/I/V) [105] The many binding partners of p62 (Figure 3.3) include important components of four well-known cellular signaling pathways, the *Wnt* pathway, the Nrf2 pathway, the mTORC pathway and the NFkB pathway [102].

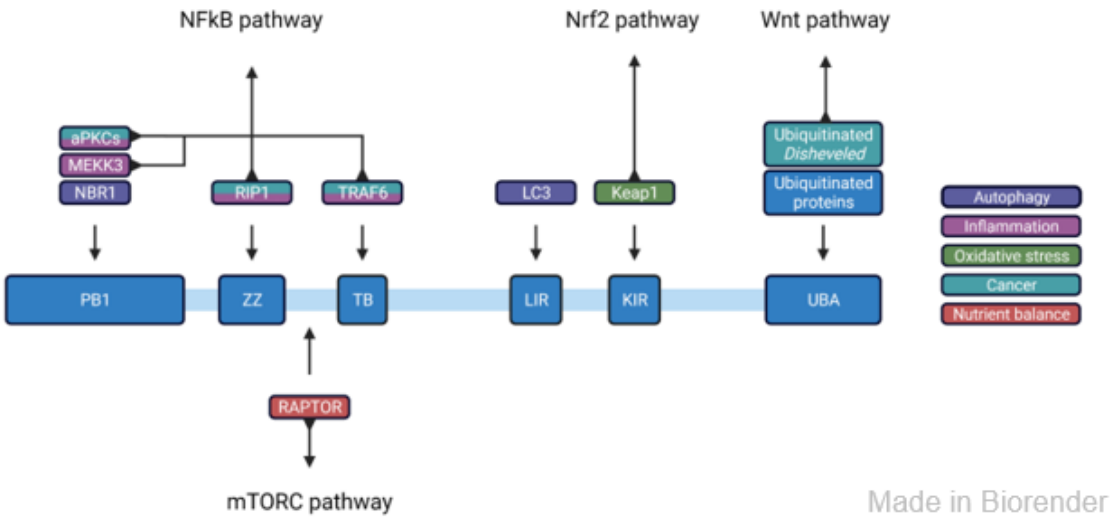

Figure 3.3: Binding partners of p62 and their functions
p62 is a central signaling hub for many pathways involved in cell proliferation and cancer, autophagy and nutrient balance, oxidative stress response and inflammation. In some pathways such as the Wnt pathway, the function of p62 is degradation of ubiquitinated pathway components, leading to their autophagic degradation and inhibition of the pathway; whereas in other pathways such as the NFkB pathway, p62 functions as a bridge to bring together multiple pathway components and facilitate downstream signaling.

The *Wnt* pathway is an outside-in signaling pathway that controls cell differentiation, migration and survival. It is important in embryonic development, cancer, diabetes, and various other diseases [106]. The pathway starts when a transmembrane G-protein coupled receptor of the *Frizzled* family binds to an extracellular *Wnt* protein. This interaction causes a signaling cascade beginning with the *Disheveled* (*Dsh*) protein and ultimately results in *β-catenin*, a transcriptional co-activator, translocating to the nucleus and triggering the expression of other proteins [106]. The role of p62 in this pathway is to bind to ubiquitinated *Dsh* protein via the UBA domain on p62, triggering its lysosomal destruction by autophagy and preventing the *Wnt* pathway signaling cascade from progressing further [102].

The Nrf2 pathway is involved in the cellular response to oxidative stress. Under normal conditions, Nrf2 is bound to the protein KEAP1, which facilitates its ubiquitination and binds to the KIR motif of p62, located in the unstructured middle region [107]. This binding triggers the p62 mediated autophagic degradation of the KEAP1/Nrf2 complex. Under conditions of oxidative stress, this degradative pathway is not triggered, and Nrf2

signaling is activated leading to the activation of further downstream pathways that counteract oxidative stress [107].

The mTORC pathway is a nutrient and stress sensing pathway. It is involved in cell differentiation, proliferation, and response to starvation [108]. The protein complex mTORC1 is activated when the cell has sufficient nutrients and amino acids for the regular functioning of the cell. If amino-acid levels are depleted, regardless of the presence of energy sources, mTORC1 signaling stops [102, 108]. When amino acid levels are sufficiently high again, mTORC1 is translocated via its interaction with RAPTOR to the lysosomal surface [102]. At the lysosomal surface, mTORC1 is activated again via its interaction with the protein Rheb. In this pathway, under normal nutrient conditions, p62 binds to RAPTOR and brings it (and mTORC1) to the lysosomal surface where mTORC1 is activated [102]. It is important to note that this does not result in the lysosomal degradation of mTORC1, as p62 only functions as an adaptor to bring its cargo to the lysosomal surface without triggering autophagy [102].

The NFkB pathway is involved in cell differentiation and proliferation. This pathway can be triggered in response to TNF-α signaling to the cell as well as by RANKL mediated signaling [98]. During activation by TNF-α, the downstream effector protein RIP1 can bind either to MEKK family proteins or to aPKCs in order to eventually activate NFkB signaling [98, 102, 109]. The MEKK and aPKC families of proteins contain a PB1 domain that can interact with the PB1 domain of p62. If RIP1 binds to p62 at the ZZ domain when p62 is bound to either aPKCs or MEKKs, NFkB signaling is continued [98, 102, 109]. In the case of RANKL mediated signaling, the downstream protein TRAF6 binds to p62, where it can interact with an aPKC protein bound to the PB1 domain of p62. In this context, p62 serves the function of bringing interaction partners close together in order to facilitate downstream signaling [109].

The vast variety of the interactions of p62 makes it a very central player in the maintenance of cellular homeostasis and response to various extracellular signals, however structural information for the full-length protein, or any truncation of the protein containing more than one domain is entirely absent.

3.1.2 Phase separation and p62

Within the context of cellular biology, phase separation is defined as the re-organization of macromolecules such as proteins into dense and dilute regions [110]. Phase separation inside the cell can lead to the formation of biomolecular condensates, which are punctate structures composed of dense arrangements of macromolecules that are not surrounded by a membrane [110]. The formation of these condensates can be facilitated by sequestration of a large number of macromolecules around some kind of central scaffold. It is reasonable to surmise that the filament forming properties of p62, as well as the large number of binding sites present on the protein make it a good driver of phase separation. Indeed, one example of these condensates are p62 bodies [92], which contain, in addition to p62, NBR1 and various ubiquitinated and ubiquitin binding proteins [111]. The properties of the condensates formed around p62 can be modulated by a wide variety of post-translation modifications (PTMs), many of which are reviewed by Berkamp, et al. 2020 [92]. The disordered regions of p62 contain many of the sites for these PTMs, as well as the binding sites to many proteins. Some of these modifications, such as ubiquitination by TRIM21 at Lys7 in p62 would disrupt the helical scaffold, and are also known to reduce the number and size of the p62 bodies formed inside cells [112, p. 21]. Other modifications such as acetylation by TIP60 in the UBA domain of p62 increase its affinity for poly-ubiquitinated cargo, as well leading to the formation of larger and more numerous p62 bodies [113]. This suggests a central role for the quaternary structure of p62, and the probable involvement of an oligomeric assembly of p62, such as a filament, within the context of cellular phase separation.

3.2 Results

3.2.1 Purification of SQSTM1/p62

Full length human p62/SQSTM1 was successfully expressed and purified by nickel affinity chromatography followed by dialysis to remove excess imidazole (Figure 3.5). The purified protein was then concentrated to 2 mg/mL and the MBP tag was removed following digestion with 3C protease. After tag removal, the protein forms long, flexible filaments with

a width of approximately 15 nm, as visualized by negative staining (Figure 3.5). For further cleanup and concentration, the filaments were then centrifuged at 20,000 × *g* for 30 minutes and resuspended in the appropriate buffer (section 5.2).

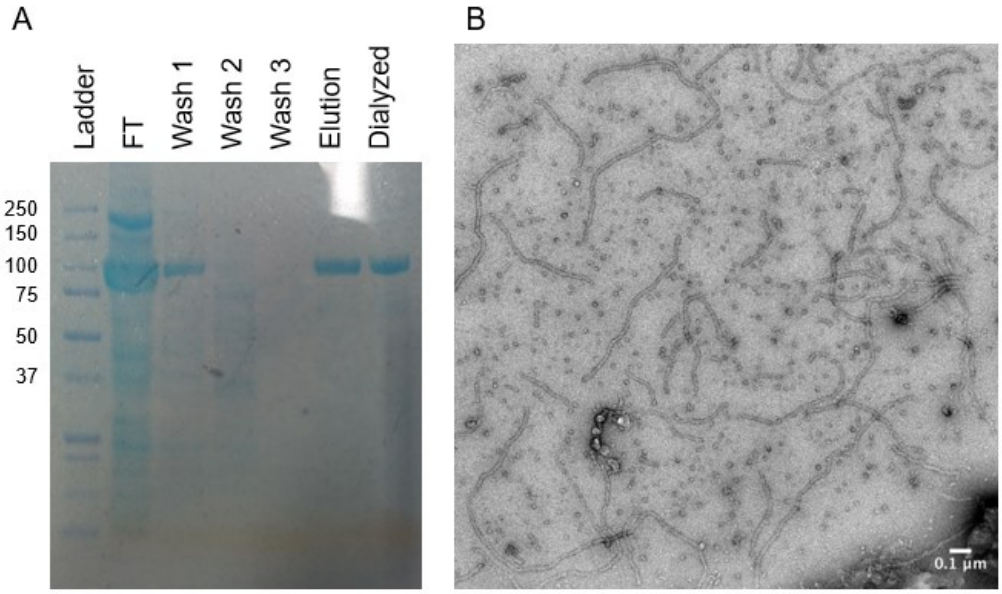

Figure 3.5: Purification and filament formation of full-length p62
(A) SDS-PAGE analysis of the purification of p62 shows that full-length *H. sapiens* p62/SQSTM1 was effectively purified by nickel affinity chromatography. (B) A negatively stained micrograph of purified p62 protein after MBP tag removal shows that the protein forms long, flexible filaments.

3.2.2 SQSTM1/p62 structure determination

3.2.2.1 p62 structure at pH 6

In order to resolve the structure of the full length p62 filaments at pH 6, the filaments were formed, centrifuged, and resuspended in 50mM sodium acetate pH 6, 50mM NaCl, and plunge frozen as described in the Materials and Methods section. Around 4000 micrographs were collected on a Talos Arctica 200 keV instrument equipped with a K3 camera and GIF at 100,000x magnification in counted super-resolution in SerialEM [114], with a defocus range of -0.5 to -3 µm (Figure 3.6A). The micrographs were motion corrected in WARP [78] using default parameters, and particles were picked using crYOLO [80]. The picked particle locations and micrographs were imported into RELION [79] where they underwent CTF estimation using CTFFIND4 [115] and particle locations were extracted as around 5 x 10^6

segments with a box size of 352 Å, with 90% overlap. Two rounds of 2D classification were performed in order to remove junk particles. Classes with clearly defined PB1 domains were then selected, leading to a total of 1.6 x 10^6 segments.

Several pieces of useful information were clear from the 2D classes. The filaments have a large amount of heterogeneity in their pitch (Figure 3.6B), ranging from ~135 Å to over 160 Å (Figure 3.6C). The PB1 domain showed features resembling secondary structure (Figure 3.6D). The rest of the protein, however, appeared as a grey blob, sandwiched between the PB1 domains (Figure 3.6D). In addition, two strands of PB1 domains with apparent D1 symmetry are visible (Figure 3.6D).

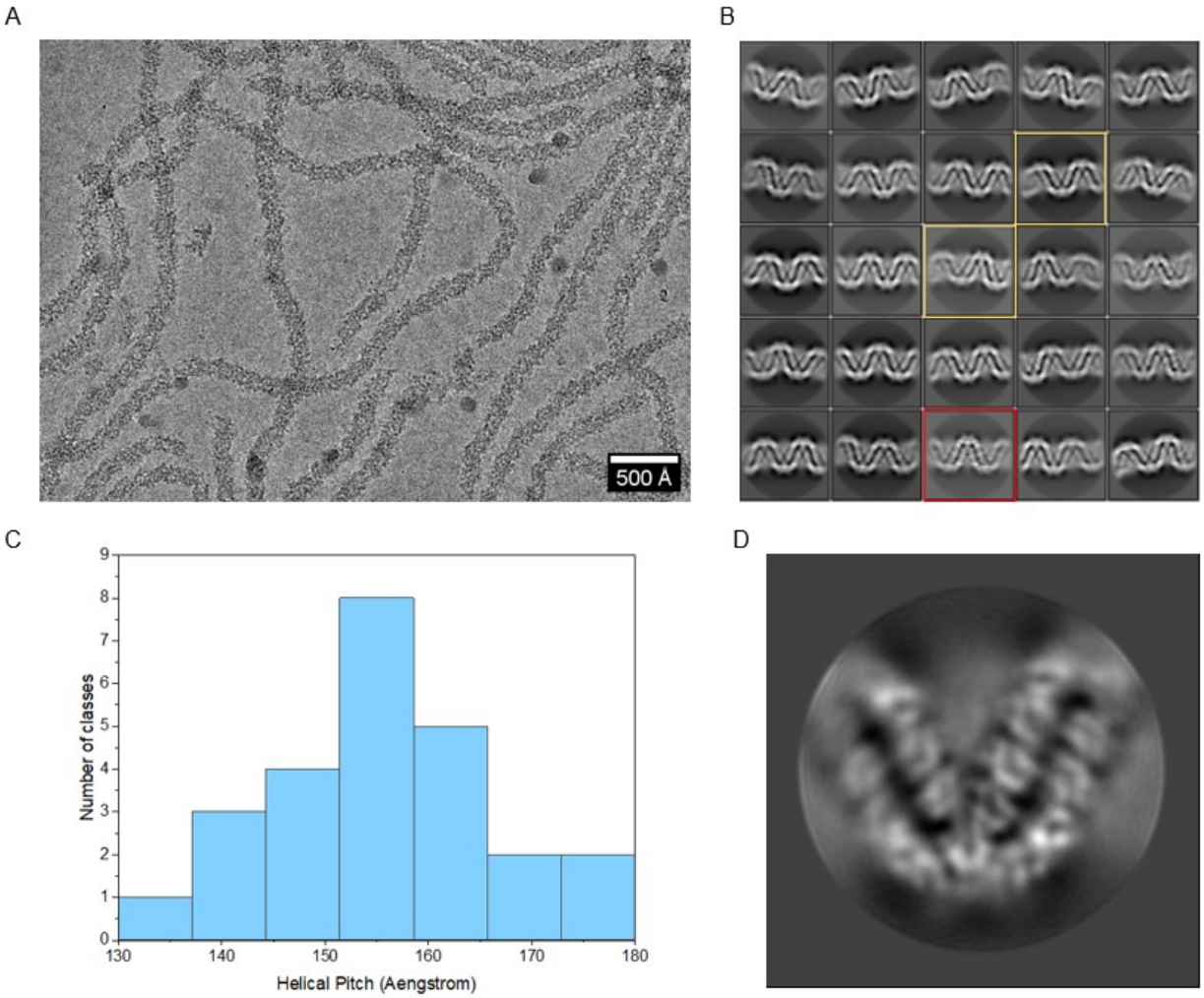

Figure 3.6: Full-length p62 dataset collection and initial processing
(A) Representative micrograph showing general distribution and overall appearance of the filaments under cryo-EM. (B) Initial 2D classes after cleanup showing apparent variation in pitch, with classes in yellow showing a higher helical pitch than the class in red. (C) Histogram of the measured helical pitch of 2D classes. (D) A magnified 2D class with a tight mask, in which individual PB1 domains are clearly visible with apparent D1 symmetry, including secondary structure details. In addition, there is fuzzy density on the inside of the tube which probably corresponds to the C-terminal domains.

The PB1-domain only structure of p62 which was resolved by Jakobi, et al. 2020 [116], who showed that the S-type filament had around 14.0 units per turn. This configuration was used as a starting point and simulated helical lattices corresponding to 14.0 units per turn (including D1 symmetry), and a helical pitch ranging from 135 Å to 180 Å were generated (Figure 3.7A). These starting models were used for supervised 3D classification in RELION

(Figure 3.7B). The results showed two classes with clearly defined secondary structure in the PB1 domain, with pitch values of 135 Å, with ~158,000 segments, and 150 Å, with ~127,000 segments, (Figure 3.7B). The particles from these classes were subjected to 3D auto-refinement in RELION (Figure 3.7C), where the symmetry parameters converged to 10.044 Å rise, -26.3387° twist, and 11.13 Å rise, -26.22° twist, respectively. The resolution of the 135 Å pitch species was determined to be 4.8 Å by FDR-FSC (Figure 3.7D) as part of the software package SPOC [117]. This map was used for further structure analysis.

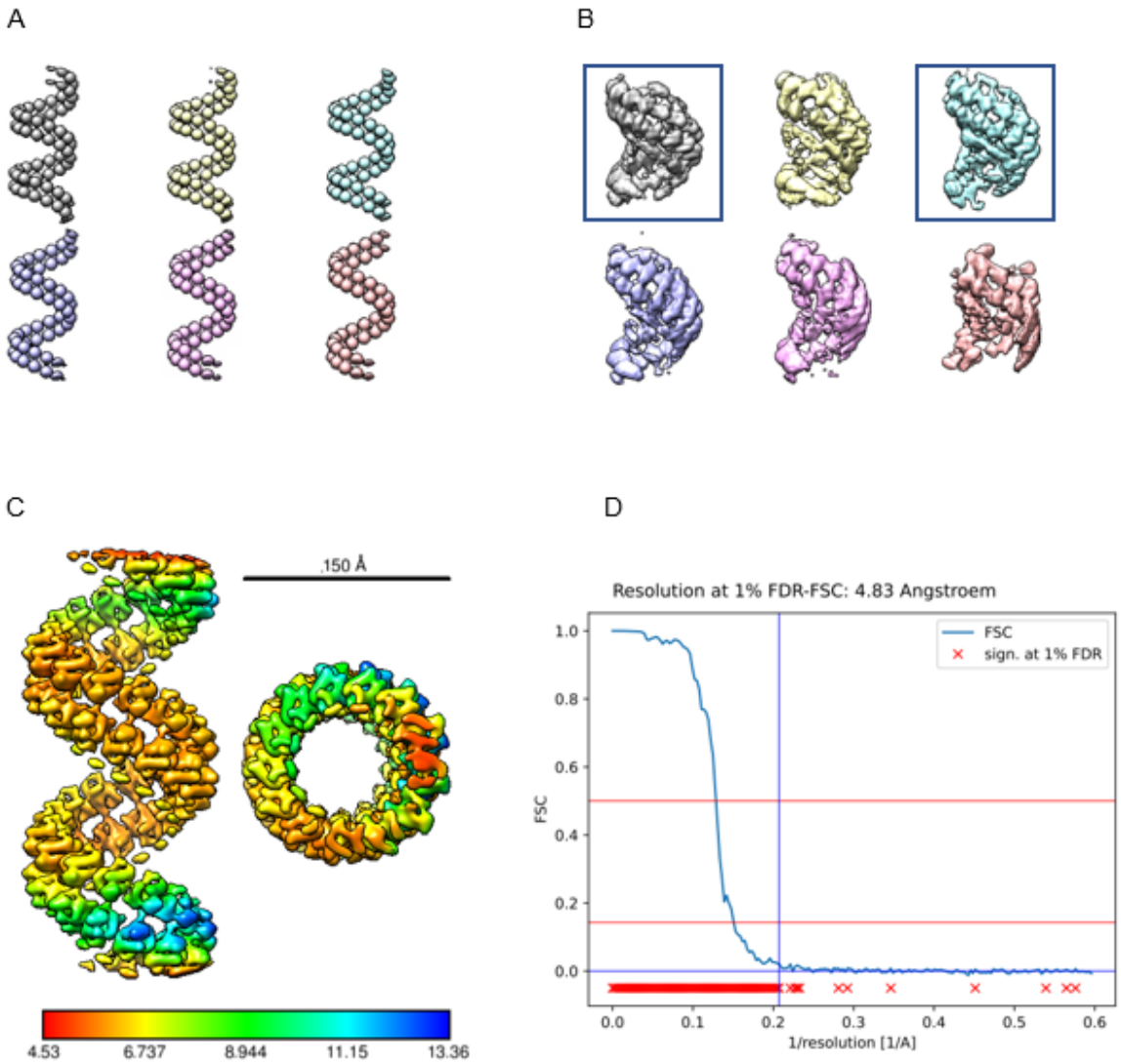

Figure 3.7: Full-length p62 classification and structure determination
(A) Simulated helical lattices were generated with different helical rise for use as initial models, corresponding to 14.0 units per turn and pitch values of 135, 140, 150, 160, 170 and 180 Å. (B) Supervised classification using the simulated initial models yielded two classes with well-defined PB1 domains (blue boxes). (C) Helical refinement of the best class in RELION yielded a structure showing PB1 domains arranged in a double stranded, anti-parallel architecture in a tube with a width of ~150Å. The map is colored according to local resolution as determined by SPOC (D) The FDR-FSC curve generated by SPOC shows a global average resolution of 4.83Å.

The refined structure shows the PB1 domains arranged as two anti-parallel strands with D1 symmetry (Figure 3.8A). The ZZ-type ring finger domain is only visible as a blob at 7-8 Å resolution, while other domains are not well-resolved (Figure 3.8A). In addition, there

is no density on the outside of the tube, meaning that all the other domains and motifs present on p62 are buried on the inside of the tube (Figure 3.8B). The atomic model of the PB1 domain of p62 (PDB: 6TGY) fits in the density of the PB1 domain (Figure 3.8C) well. The map features match the calculated global resolution, as helices are clearly visible, but higher resolution features like β-sheet separation are not observed.

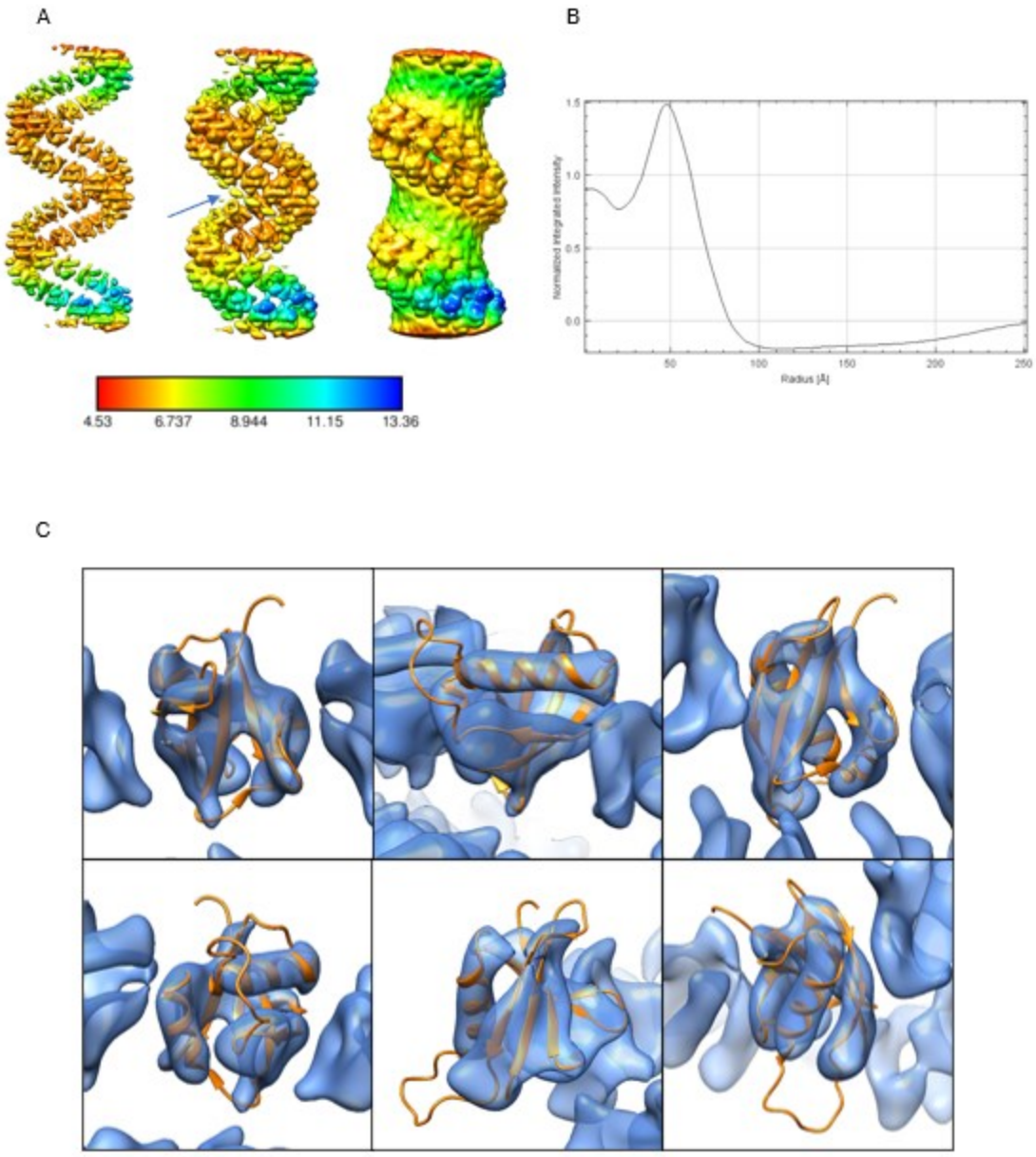

Figure 3.8: Overall features of full-length p62 map
(A) The map rendered at different thresholds (0.0521, 0.041, and 0.0276) shows that the PB1 domain is well-resolved, the ZZ domain appears as a featureless blob (arrow) and the other domains are not well resolved. (B) The radial intensity of the unfiltered map shows that all of the density present is on the inside of the tube, with no density present outside of the PB1 scaffold. (C) The atomic model of the PB1 domain of p62 fits well into the PB1 density.

The docked in PB1 domains are positioned to make numerous inter and intra-strand connections. Each resulting PB1 strand is presumably stabilized by the interaction of several

charged residues on the following subunit within the strand (Figure 3.9A). The two strands are also interacting with each other via a reciprocal interaction of charged residues Lys-91 and Asp-92 (Figure 3.9B).

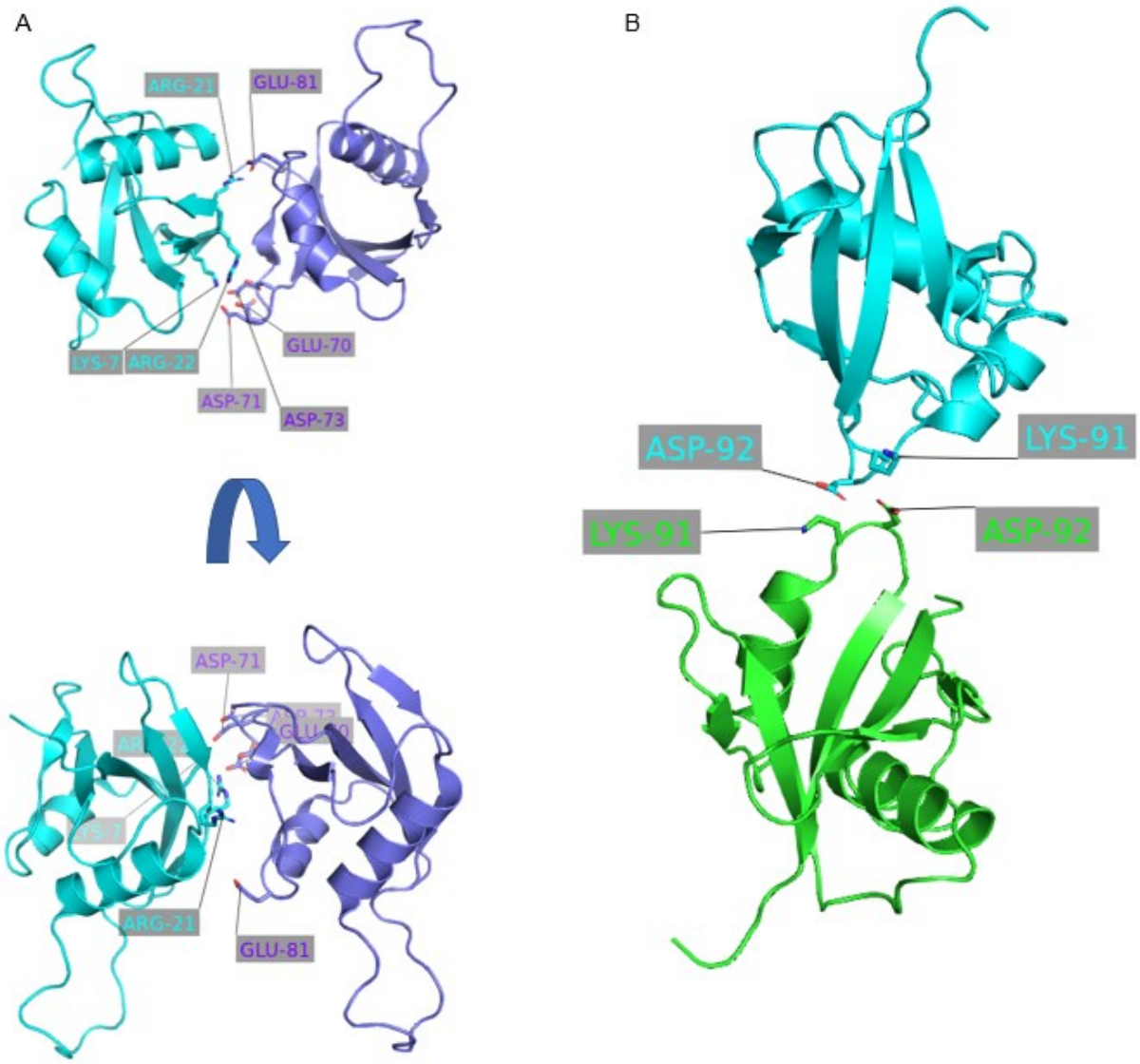

Figure 3.9: Residue interactions between subunits in full-length p62 filaments
(A) Within each strand, the two subunits interact using a series of charged residues, the positively charged Lys-7, Arg-21 and Arg-22 on one subunit interact with the complementary negatively charged Glu-70, Asp-71, Asp-73 and Glu-81 residues on the next subunit (B) The two strands also interact with each other using a reciprocal pair of charged residues, Lys-91 and Asp-92.

3.2.2.2 p62 structure at pH 8

In order to study the effect of pH on the morphology of the filaments, the pre-formed filaments were centrifuged and resuspended into 20mM HEPES, pH 8, 50mM NaCl and plunge frozen as described in the Materials and Methods section. Around 960 micrographs were collected on a Talos Arctica 200 keV instrument equipped with a K3 camera and GIF at 100,000x magnification in counted super-resolution mode in EPU (Thermo Fisher Scientific), with the defocus range of -0.5 to -3 µm. The micrographs were motion corrected in WARP, and CTF estimation and particles were picked using the filament tracer in CryoSPARC, resulting in ~436,000 picked particle locations. The particles were extracted with a box size of 503 Å, with 96% overlap. After two rounds of 2D classification to remove junk particles, ~100,000 particle segments remained. The 2D classification results showed that in many of the classes, corresponding to about 60% of the segments, the two strands were unwinding (Figure 3.10). It is noteworthy, however, that the smeared inner-tube density was still inside of the tube and did not seem to be present on the outside of the tube (Figure 3.10). The heterogeneity of this dataset prevents high resolution structure determination.

Figure 3.10: Full-length p62 at pH 8 shows unwinding of the two strands
The results of 2D classification show that at pH 8, 60% of the particles show an unwinding of the two strands (red), whereas 40% of the particles still show a closed form of the filament (blue).

3.2.3 p62 interaction with binding partners

The interaction of full-length p62 filaments with LC3b is facilitated by its LIR motif [118]. Full length p62 filaments dissociate into smaller monomers or oligomers upon interaction with affinity matured LC3b, in a dose dependent manner as shown by negative staining (Figure 3.11A). At lower concentrations (< 1:2 molar ratio LC3b:p62), the effect is small, however at higher ratios almost all filaments have dissociated (Figure 3.11B). A similar effect was previously described when p62 filaments prepared from the PB1 domain-only construct interact via the PB1 domain with the PB1 domain of NBR1 [116]. The full-length p62 protein shows the same behavior (Figure 3.11A, B). A similar effect is also observed during the interaction of p62 with both vault RNA 1-1 and 1-2 (Figure 3.12). The effect is more prominent with the 1-1 vtRNA, this is to be expected since it is a stronger binder [119]. This interaction is driven by the ZZ-type ring finger domain on p62. Taken together, these results suggest that the various binding domains of p62, while located in the inside of the tube, are still available for interaction and binding to other proteins or ligands.

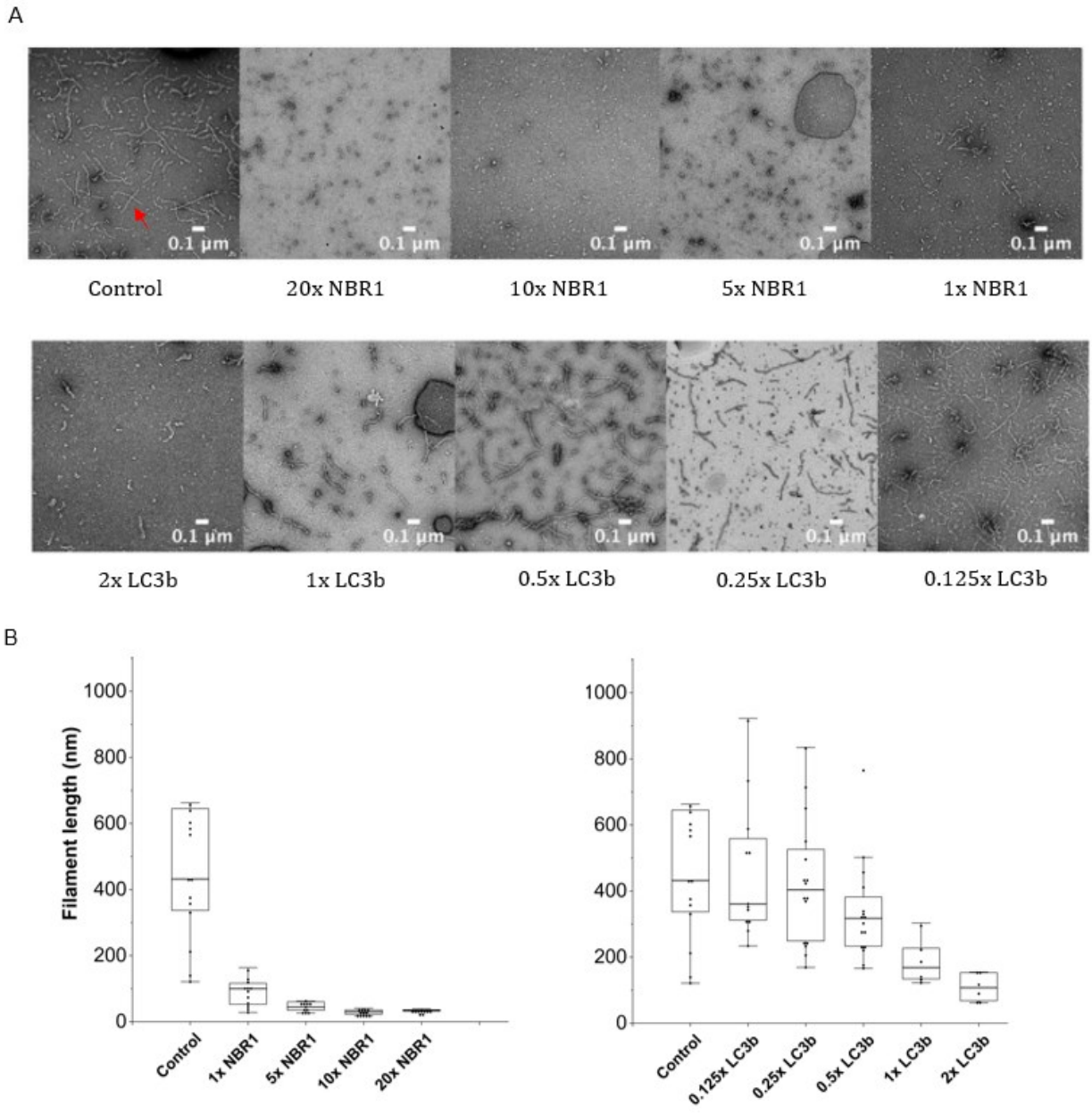

Figure 3.11: p62 interaction with LC3b and NBR1-PB1 leads to filament shortening and disassembly

(A) p62 filaments can interact through the PB1 domain with NBR-PB1, leading to a dose-dependent depolymerization of the filaments at high NBR1-PB1 to p62 ratios. In addition, the interaction of the filaments through the LIR domain on p62 with LC3b leads to a dose-dependent depolymerization of the filaments. A single filament is pointed out by a red arrow. (B) Box plots showing the quantified depolymerization. The filaments were measured in ImageJ. The box ends demarcate the 25 and 75 percentiles. The median line is drawn through the box. The vertical lines represent the region containing data points within 1.5 IQR.

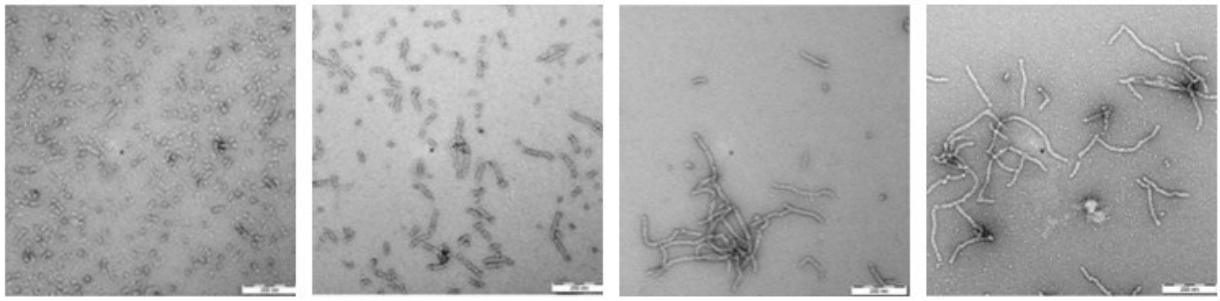

Figure 3.12: p62 interaction with vault RNAs hinders filament formation
p62 can also interact with vault RNAs 1-1 and 1-2 through the ZZ domain on p62. If the vtRNAs are incubated with p62 during filament formation, they both lead to shorter filaments overall, however the effect is much stronger with the 1-1 vtRNA.

3.3 Discussion

3.3.1 Full length p62 forms flexible, tubular assemblies

The cryo-EM structure of full length human p62/SQSTM1 shows that the protein is driven to assemble into double stranded, tubular structures by the interactions of the PB1 domain. The tubular structure is both locally and globally flexible. The global flexibility is apparent on the micrograph level, which shows that the filaments are not straight and make frequent twists and turns. On the other hand, the presence of multiple pitch values in the datasets show that the assemblies also have local flexibility. The previously published structures of the PB1-domain only constructs [116] show that there are three and four-stranded assemblies, while the full length construct only forms double stranded assemblies. In addition, the PB1-domain only structures do not appear to show as much global flexibility as the full length construct (compare Figure 3.6, panel A in this work with Figure 2, panel B in [116]). The PB1 domain-only constructs also do not show as much local flexibility, this is evident from the fact that the PB1-domain only structures do not show the presence of multiple pitch values. This increased flexibility in the full-length structure may be related to the fact that each monomer makes fewer contacts with the next monomer in each strand in the full length structure (compare Figure 3.9 panel A to Figure in this work to Figure 3, panel E in [116]).

3.3.2 The strands in the assembly show an open and closed form modulated by pH

An additional source of flexibility in the full-length structure is that the two strands themselves seem to dissociate at pH 8, leading to filament opening. This behavior is perhaps not entirely surprising, since the two strands are stabilized by the reciprocal interaction of charged residues Lys-91 and Asp-92 on opposing strands. While pH 6 and pH 8 may represent the extremes of this strand opening, inside the cytosol which is at pH 7-7.4 [120], there may exist a wide spectrum of open and closed states. Concurrently, the structure shows that all of the density is on the inside of the tube, and none of the domains seem to be available for interaction with binding partners. This opening and closing of the filament strands could be a mechanism by which the other binding domains become more exposed and available for interaction.

Whether the open or closed form of the p62 filaments are present inside cells is not known, and the cellular relevance of the open and closed form of the filaments in response to pH changes is uncertain. However, while the overall pH of a cell is neutral, there are local variations in pH throughout the cytoplasm as well as organelles. It has been previously suggested [121] that the lower pH of the autophagosome induces the formation of p62 filaments and increases the binding affinity of p62 to its cargo. The authors based this hypothesis on the fact that they observed only small oligomeric structures of p62 at neutral pH, while at pH 5.5-6.5 they were able to produce longer p62 filaments *in vitro*. Their results are inconsistent with the results of this thesis, since the full-length filaments used for structure determination were formed at pH 8. Nevertheless, it is still possible that variations in cellular pH, which induce the opening and closing of the filaments, can still affect the binding affinity of p62 to its cargo.

p62/SQSTM1 also has many sites for post translational modifications [92]. One particularly relevant modification as it relates to filament opening and closing is Lys-91, which is ubiquitinated in response to the activation of antibacterial autophagy [122]. Additionally, Lys-7, which is involved in stabilizing the intra-strand interaction, is also ubiquitinated in response of oxidative stress [112]. The disruption of the filament scaffold by these modifications could be another mechanism by which the other domains can be

exposed and become capable of interacting with binding partners. Within the context of phase separation and p62 body formation, other PTMs such as phosphorylation by TAK1 or acetylation by TIP60 can modulate the size and number of p62 bodies formed in cells [92]. The pH-driven conformational change in the filaments may be relevant in this context, in the sense that filament opening can expose residues on p62 so that they can be modified by enzymes.

3.3.3 Interactions with binding partners cause filament disassembly

While it is known that the polymerization behavior of p62 is required for it to carry out its function within the context of autophagy [123], all of the binding partners tested in this work (NBR1, LC3b, vault RNA) depolymerize the filaments. Since all three proteins bind to different regions of p62, it may be expected that the interaction and filament disassembly process is different for each binding partner. Furthermore, the fact that LC3b and vault RNA are both capable of binding to the filaments at pH 6 when the filaments are in the closed form, strongly suggests that even though the non-PB1 domains of p62 are structured within the helical assembly, there still exists a mechanism by which they can interact with their binding partners.

NBR1 interacts with p62 through its PB1 domain, and binds to the ends of p62 filaments [116]. The fact that filaments actively depolymerize upon addition of NBR1 suggests that individual p62 monomers may be able to leave and rejoin the helical scaffold. After an individual p62 monomer has left the helical assembly, an NBR1 molecule could take its place and lead to the breaking of the helical scaffold. At high NBR1 concentrations, the repeated breaking of the helical scaffold would eventually lead to full disassembly of the filaments.

In the case of LC3b, binding happens through the LIR motif on p62. This motif must somehow be accessible in the solution for LC3b to be able to interact with it. However, due to the low resolution of the structure in this region, the mechanism of the interaction cannot be determined. Nevertheless, the binding of LC3b to the filaments would introduce steric stress on the assembly, and it is not surprising that the helical scaffold would collapse at high LC3b concentrations. An important caveat is that the experiments were done with LC3b that was in free solution, which is not the native state of LC3b inside cells. Inside cells, since LC3b is anchored to the growing isolation membrane, this depolymerization may not happen as

readily since the local concentration of the dissociated p62 monomers would be very high, and they could re-form their helical assembly. This partial disassembly followed by re-assembly could serve as an addition potential mechanism by which the other domains of p62 can be exposed and interact with binding partners.

The depolymerization of p62 in response to LC3b or NBR1-PB1 binding may be relevant within the context of phase separation. It has previously been shown that the interaction between p62 and octa-ubiquitin also causes filament shortening [10]. It is possible that the filament disassembly effect is a regulatory mechanism that prevents the formation of excessively long filaments inside cells, and thus prevents the formation of p62 bodies that are too large.

3.4 Outlook

While the structure of the full length p62 protein shed some light on the overall quaternary structural architecture and potential mechanisms of its interaction with binding partners, a number of open questions remain, such as the relative orientation of p62 domains with respect to one another. While the structural disorder in p62 may preclude the determination of a complete full-length structure, the fact that p62 functions as a signaling hub to bring together proteins from various pathways into close proximity to facilitate their interaction can be used as a basis for further structural work. For example, a structure of the ternary complex of p62, RIP1 and aPKCs could reveal potentially druggable interaction surfaces.

On broader structural level, studying slices of cells thinned by Cryo-FIB milling followed by Cryo-electron tomography visualization can reveal whether the filaments exist in cells, and may even show whether they exist in the open or closed states. It is also currently unknown how these filaments may interact with actual cellular cargo, and whether they can wrap around cargo, or facilitate membrane recruitment by acting as a scaffold. Experiments with artificial cargo such as ubiquitinated organelles can shed some light on this. In the long run, the full pathway of cargo recognition, sequestration and membrane recruitment could be reconstituted *in vitro* so that each step can be visualized by cryo-EM.

4 The Endosomal sorting complex required for transport (ESCRT) pathway interaction with membranes

4.1 Introduction

The ESCRT machinery can be divided into five distinct, but interacting complexes, called the ESCRT-0 to ESCRT-III complexes, and the ATPase Vps4 [50]. ESCRT-0 functions to cluster ubiquitinated cargo, ESCRT-I then hands the cargo to ESCRT-II, which recruits and associates with ESCRT-III, a protein complex that causes the constriction of the membrane, followed by abscission (Figure 4.1) [124]. ESCRT-III proteins are thought to be able to remodel both positively and negatively curved membranes, however structural studies so far have only shown ESCRT-III complexes on negatively charged membrane tubes [125].

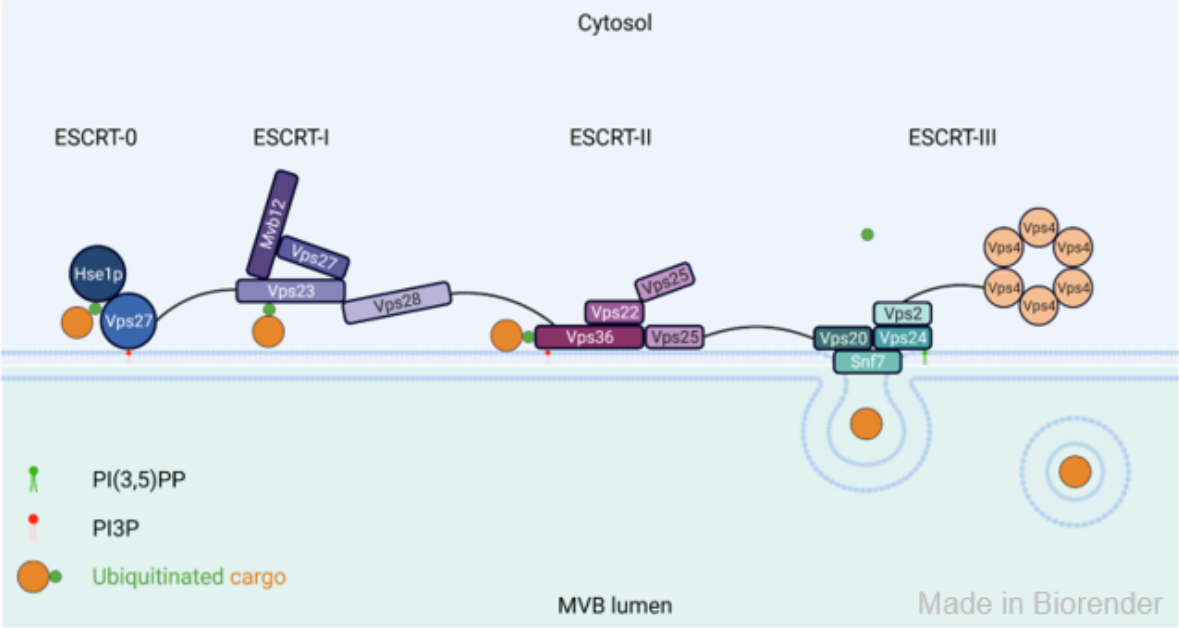

Figure 4.1: Overview of the function of ESCRT proteins in MVB formation
The ESCRT-0 to ESCRT-II complexes function to capture ubiquitinated cytosolic cargo. Following the removal of ubiquitin, and the recruitment of the ESCRT-III complex, the membrane is pinched and invaginated by the ESCRT-III complex. After the depolymerization of the ESCRT-III complex by Vps4, the cargo is packaged inside a membrane-bound vesicle and is delivered to the lumen of the multi-vesicular body. The recruitment of each successive ESCRT complex is driven by specific protein-protein interactions, which are represented as connecting lines between individual proteins in the figure. Several components of the ESCRT complexes bind to ubiquitin as well as Phosphatidylinositol 3-phosphate (PI3P), which localizes them to the membrane. The ESCRT-III subunit Vps24 specifically binds to Phosphatidylinositol 3,5-bisphosphate (PI(3,5)PP) [126]. The remodeling of the membrane is thought to be driven by formation of hetero-polymers composed of the different ESCRT-III subunits.

4.1.1 ESCRT-0, ESCRT-I, and ESCRT-II

In yeast, the ESCRT-0 complex is a heterodimer of Vps27 and Hse1p [127], which interacts to form a three-helix bundle called the GAT domain [124]. Vps27 contains a double Zinc-finger FYVE domain that it uses to bind to the phosphatidylinositol 3-phosphate that is present in endosomal membranes, thus localizing the heterodimer to the endosomes [128]. Both proteins contain ubiquitin binding domains that bind to ubiquitinated cargo, and it is thought that Hse1p acts synergistically with Vps27 in this function [129]. Vps27 also contains a C-terminal PTVP motif that recruits the ESCRT-I component Vps23.

The ESCRT-I complex is composed of Vps23, Vps28, Vps37 and Mvb12 [130]. The structure of the complete complex shows an elongated protein complex composed of a globular core headpiece containing three pairs of helical hairpins from Vps23, Vps28 and Vps37. This is then followed by a 13-nm long linker composed of Vps23, Vps37 and Mvb12, and is terminated by the N-terminus of Vps23, that contains a ubiquitin E2 variant (UEV) domain, and binds to the PTVP motif in Vps27 [129, 130] as well as to ubiquitin [51]. The C-terminal four-helix bundle on Vps28 interacts with one of the two NZF zinc finger domain present on the GLUE domain of the ESCRT-II subunit Vps36 [131, 132].

The ESCRT-II complex is composed of Vps22, Vps25 and Vps36 [133]. The overall structure of the complex shows eight repeats of a common structural domain called a winged helix [133], and is a Y-shaped complex with two non-contacting copies of Vps25, and one copy each of Vps22 and Vps36 [133]. Both Vps22 and Vps36 contain a PPXY motif that they use to bind to each Vps25 copy [133]. The Vps25 subunits directly interact with Vps20 [133], an ESCRT-III subunit. The GLUE domain of Vps36 consists of a PH domain interrupted by a yeast-specific insertion that contains two NZF domains. NZF-N is non-functional and does not bind to ubiquitin, but binds to Vps28, whereas NZF-C is functional and interacts with ubiquitin, but not Vps28 [132]. The PH domain itself is a common structural domain in ESCRT proteins that, among other functions, binds to lipids [134]. The PH domain on Vps36 is able to bind to phosphatidylinositol 3-phosphate *in vitro* [132]. Thus, Vps36 is a central binding hub that binds to ESCRT-I through NZF-N binding to Vps28, ubiquitin through its NZF-C domain, and phosphatidylinositol 3-phosphate binding through the PH domain. These interactions are not mutually exclusive and can happen together [132], while Vps25 recruits Vps20 and thus links the ESCRT-II complex to the ESCRT-III complex [135] (Figure 4.1).

4.1.2 ESCRT-III proteins and Vps4

The yeast ESCRT-III complex is formed by four proteins, Vps2, Vps20, Vps24 and Snf7. The function of these proteins is the remodeling of the membrane, creating a constricted neck and leading to abscission of the membrane [136–138]. The four proteins are thought to exist in an inactivated form inside the cytoplasm [139] and assemble on the membrane after the recruitment of Vps20 by Vps25, after which Snf7 is activated and recruited by Vps20,

followed by Vps24 recruitment and finally Vps2 recruitment [140]. The ESCRT-III proteins form polymers that are disassembled by Vps4 [141], a AAA ATPase thought to be responsible for recycling of the subunits [142].

The yeast ESCRT-III subunits Vps24 [49] and Snf7 [135] are known to form homo-oligomeric complexes in vitro. In the case of Vps24, the polymers appear as well-ordered filaments that were successfully used for structure determination to 3.2 Å resolution [49]. On the other hand, Snf7 polymers are extremely heterogenous and can appear as filaments or ring-shaped spirals that can form either on lipid monolayers [135] or as sheets, rings and strings that can form in solution [143]. In contrast, Vps2 and Vps20 are not known to form oligomeric structures on their own, however Vps2 is known to co-pellet with Vps24 [49].

4.1.2.1 Common structural features of ESCRT-III proteins

All four proteins share the basic secondary structure (Figure 4.2) including an N-terminal region composed of helix α0. In the case of Snf7, this α0 helix is known to bind to membranes and is thought to function as an anchoring point [144]. The N-terminus is followed by the core domain consisting of four additional α-helices, called helices α1 to α4, separated by short linkers. The core domain is flanked by one additional helix, α5, and a C-terminal MIT-interacting motif [135] responsible for binding to the MIT domain present on Vps4. In Vps24, this MIM domain is degenerate and does not interact with Vps4 [131]. Although for Snf7, the full length protein does not bind to Vps4, Snf7 truncations bind to Vps4 [145]. There are several structures of yeast Vps24 and Snf7 and show that the proteins do indeed have a very similar overall structure. In the case of Snf7, the N-terminal helix α1 and helix α2/ α3 form a hairpin structure, while helix α4 is positioned further away from the hairpin [146] (Figure 4.3). In the case of Vps24, helices α1 and α2 also form a hairpin structure, however helix α3 is positioned farther away from this hairpin [49]. The AlphaFold2 predicted structure of the Vps24/Vps2 complex from yeast [147] also shows a similar overall fold for Vps2, with helices α1- α3 being nearly superimposable with Vps24 (Figure 4.3). It should be noted, however, that the computed structure of Vps24 is slightly different from the experimental structure, in particular the stretch after helix α3 (Figure 4.3).

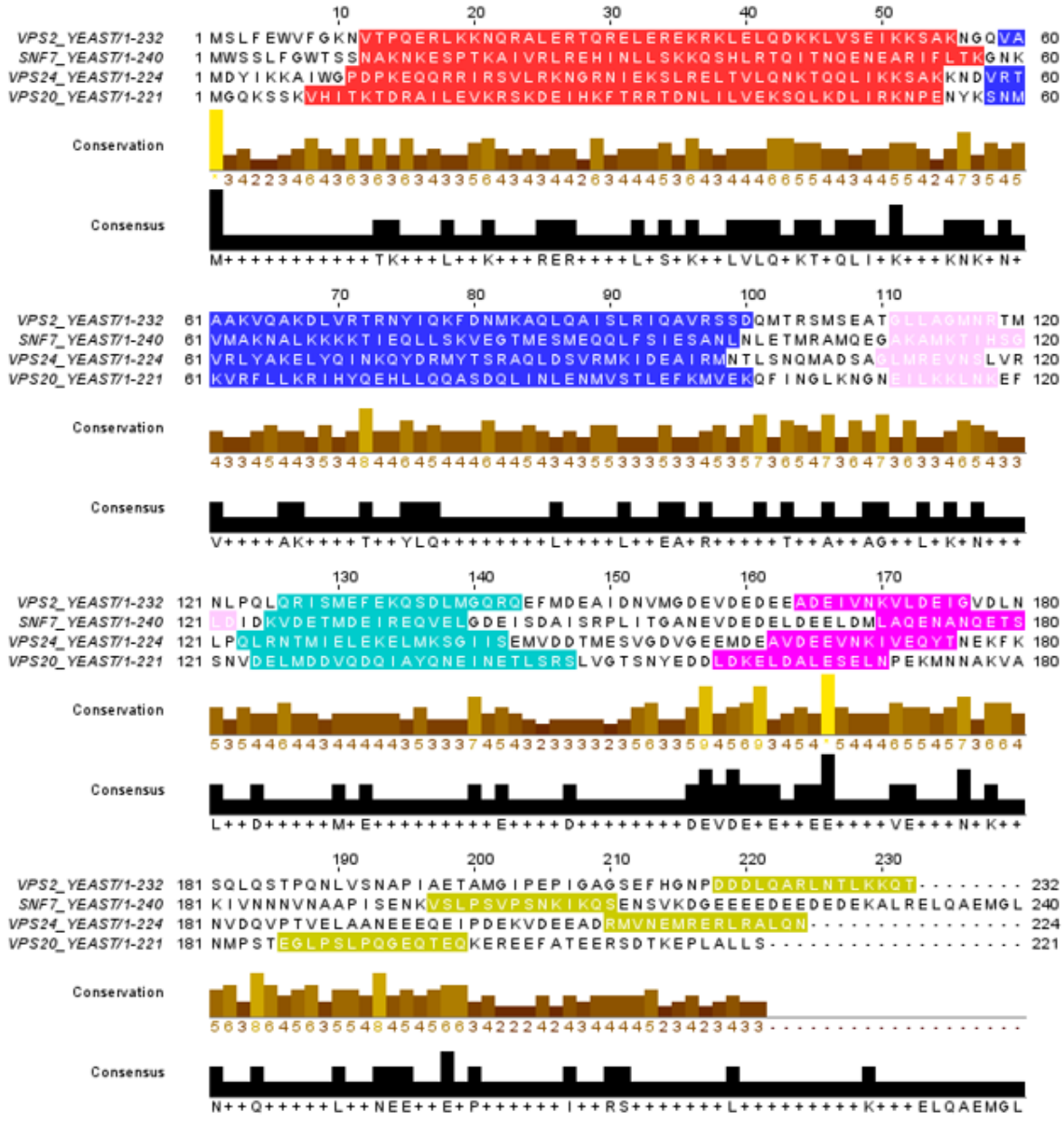

Figure 4.2: Sequence alignment of yeast ESCRT-III core proteins
The sequence alignment of the yeast ESCRT-III core proteins shows that despite relatively low sequence homology, the secondary structure is well conserved. The helices α1 through α5 and the MIM are colored thusly: α1 in red, α2 in blue, α3 in pink, α4 in cyan, α5 in hot pink and the MIM in yellow.

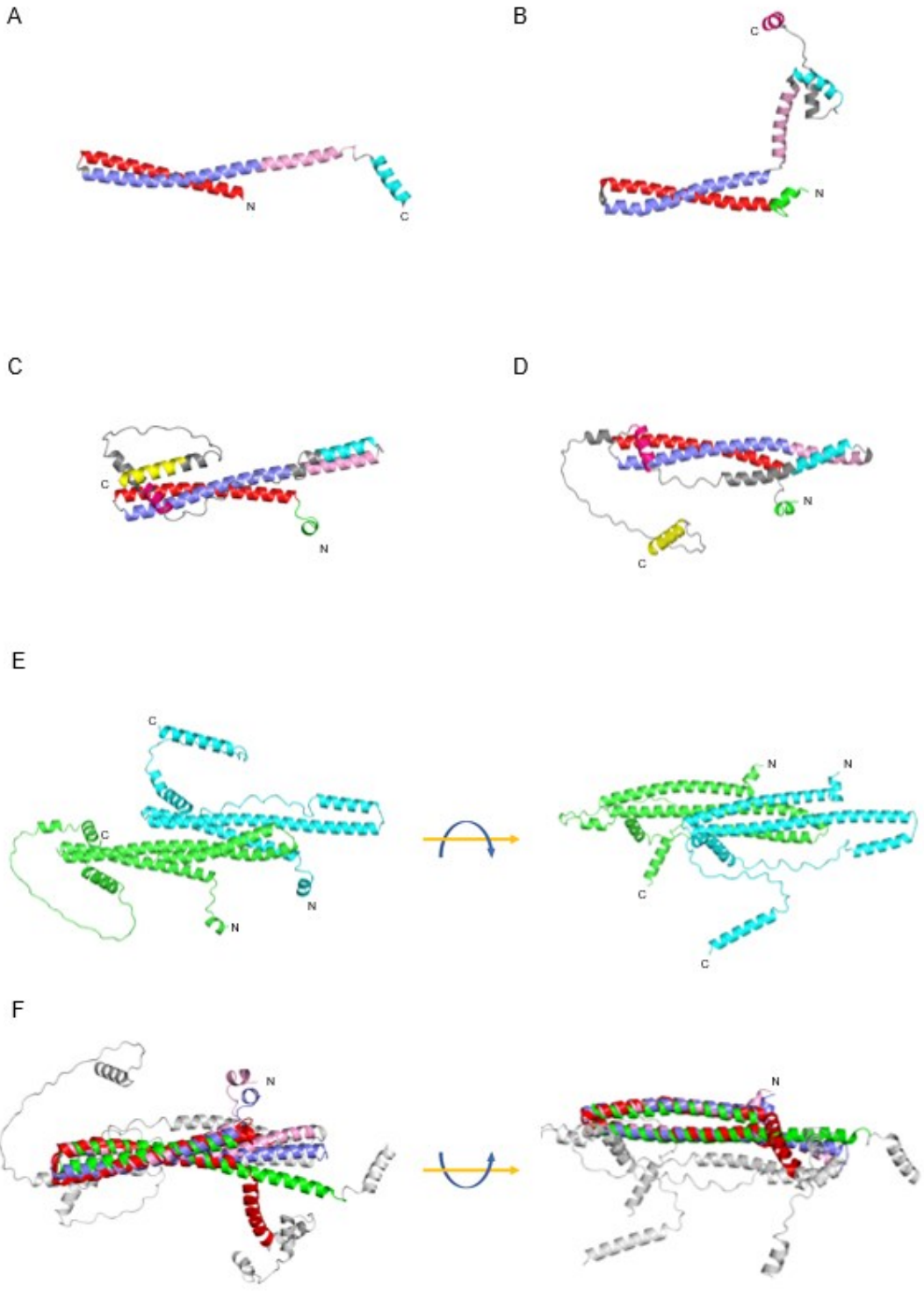

Figure 4.3: Published structures of yeast ESCRT-III proteins
(A)-(D) The published structures of yeast ESCRT-III proteins, **Snf7** (**A**, PDB ID 5FD7, [146]), **Vps24** (**B**, PDB ID 6ZH3, [49]), computed **Vps24** structure (**C**, Model Archive ID ma-bak-cepc-0391, [147]) and computed **Vps2** structure (**D**, Model Archive ID ma-bak-cepc-0391, [147]), colored according to secondary structure elements, with helix α0 in green, α1 in red, α2 in

blue, α3 in pink, α4 in cyan, α5 in hot pink and the MIM in yellow. (E) The computed structures of Vps2 and Vps24 were computed as a dimer with Vps2 in cyan, and Vps24 in green. All of the structures share the same β-hairpin consisting of helix α1, α2 and α3, with the exception of the experimental Vps24 structure that shows α3 moving away from the hairpin. This is shown in panel (F), with the overlay of all four structures, with Vps24 in red, Snf7 in green, computed Vps24 in blue and computed Vps2 in pink. Note that only α1, α2 and α3 are colored for each protein, with the remaining portions represented in grey.

Some of the ESCRT-III subunits including Snf7 [146], and Vps24 [49], and the human ESCRT-III subunit CHMP1B [86] show a distinct open or extended conformation, whereas human CHMP3 [148, 149] and yeast IST1 [150] show a closed conformation (Figure 4.4). The closed conformation is thought to represent the autoinhibited form of the protein [142, 150]. The movement between the closed and open states involves a hinge between helices α2 and α3, in the closed form, helices α3 and α4 form a short hairpin and fold back to dock onto helices α1 and α2, while helix α5 folds back to dock near the demarcation region between helices α1 and α2 (Figure 4.4).

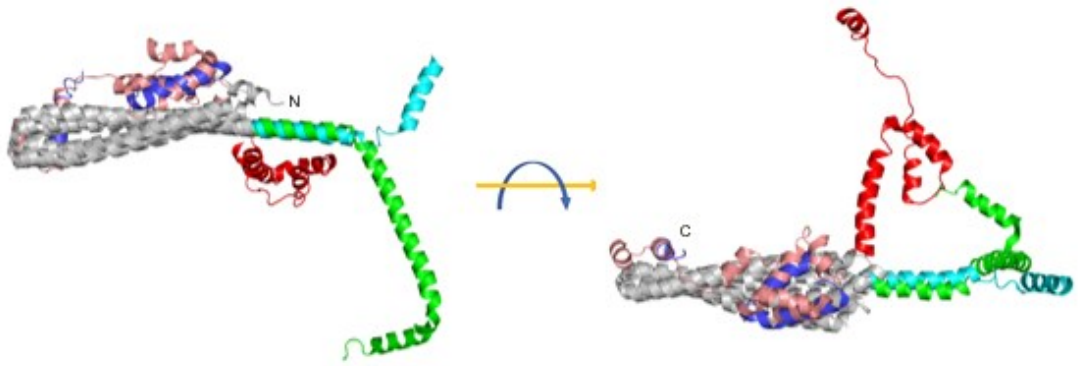

Figure 4.4: Open and closed forms of the ESCRT-III proteins
Compared to yeast Snf7 (PDB ID 5FD7), and yeast Vps24 (PDB ID 6ZH3), and human CHMP1B (PDB ID 3JC1), the yeast IST1 (PDB ID 3GGY) and the human CHMP3 (PDB ID 3FRT), show a closed conformation. In the closed conformation, which is thought to be the inactive form of the protein, a hinge region between helices α2 and α3 enables helix α3 and helix α4 to turn back and dock onto helices α1 and α2. In addition, in the closed form of the structures, helix α5 also folds back to dock onto the hinge region between helices α1 and α2.

The human ESCRT-III homolog CHMP1B deforms negatively charged liposomes into tubular shapes *in vitro* (Figure 4.5), and the resulting tubes show widths of 26-30 nanometers [125]. In these tubes, whose structure was solved to ~ 6 Å, the CHMP1B subunits are present in an open state, and the intralumenal distance between the inner lipid headgroups on opposite sides of the tube is 12 nanometers. The addition of IST1 to this mixture causes further membrane constriction, yielding tubes with a width of 24-25 nanometers, and the distance between the inner lipid headgroups is further reduced to 4.4-4.8 nanometers [125]. The CHMP1B-IST1 copolymer shows an inner lipid tube constricted by a CHMP1B protein coat that is in turn surrounded by an IST1 protein coat [125].

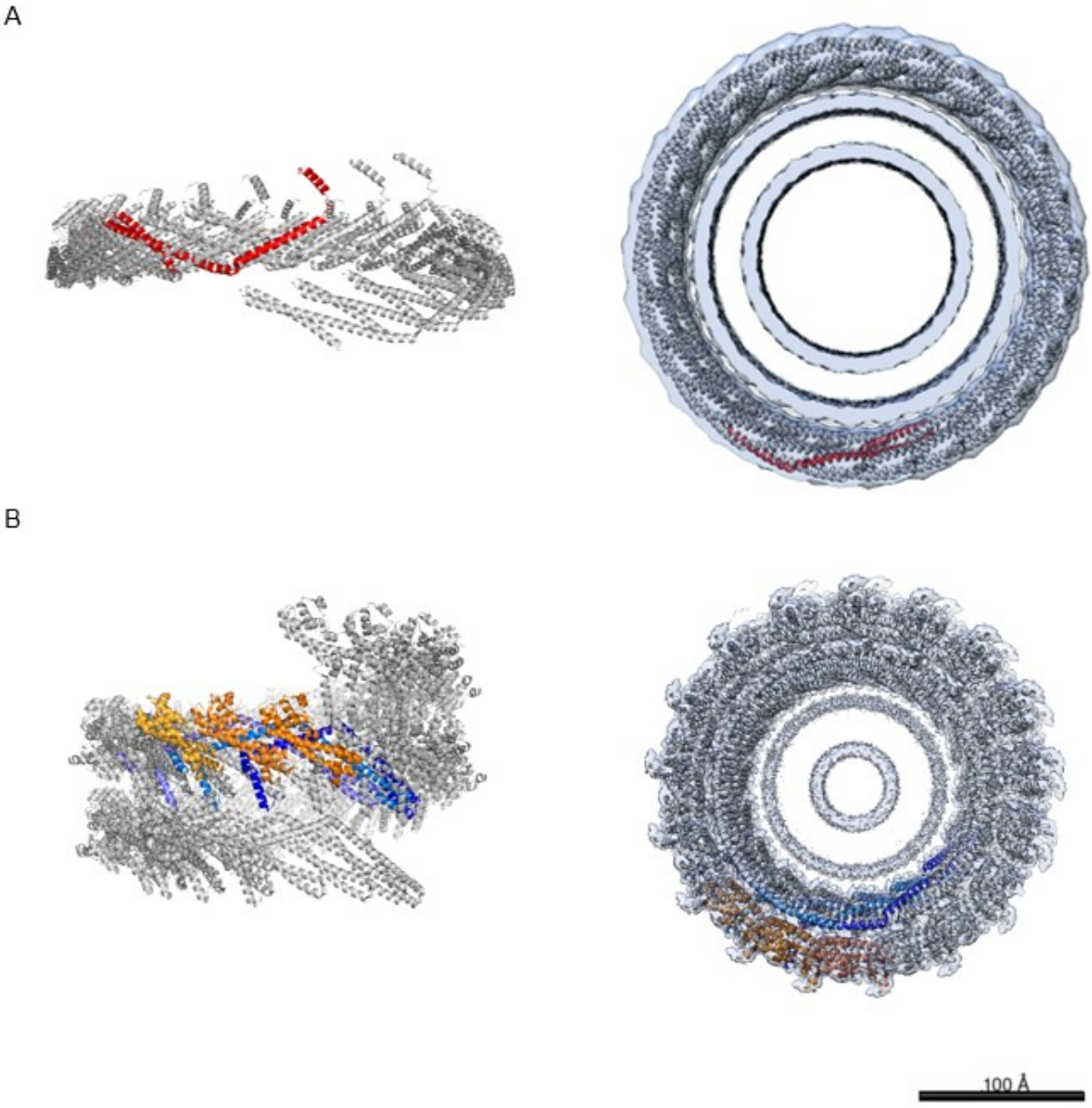

Figure 4.5: Structures of ESCRT-III polymers in complex with lipids
(A) Side and top views of human CHMP1B protein wrapped around a lipid bilayer (PDB ID 6TZ9 [125]) with a single monomer highlighted in red. The top view includes the experimental EM map that shows density for the lipid bilayer. In this structure, the CHMP1B protein is in the open state. (B) Side and top views of the CHMP1B/IST1 heterodimeric polymer wrapped around a lipid bilayer (PDB ID 6TZ5 [125]), with CHMP1B monomers are in the open state and highlighted in shades of blue, while IST1 monomers are in a closed state and highlighted in shades of orange. The top view also shows the experimental EM map which shows density for the lipid bilayer. Note the significant constriction of the lipid bilayer compared to the CHMP1B-only structure.

4.1.2.2 Vps4 and its interaction with ESCRT-III subunits

Vps4 is a AAA ATPase that catalyzes the exchange of ESCRT-III subunits [142]. Vps4 can exist as a monomer or dimer at low protein concentrations, however at higher concentrations and upon binding to the co-factor Vta1 forms hexamers, that is thought to be the catalytically active form of the protein [151]. The structures and functions of Vps4 domains are reviewed by McCullough, 2018 [142]. The N-terminus contains a MIT domain that binds to the C-terminal MIM motif of ESCRT-III proteins, this is followed by the core ATPase domain, and a β-domain insert that binds to Vta1. Vps4 is known to bind to peptide substrates and progressively pass them through the central cavity present in the hexamer as each monomer hydrolyzes ATP, leading to a complete unfolding ESCRT-III proteins as determined by hydrogen-deuterium exchange experiments [152]. It is thought that this protein unfolding activity combined with the passing of a polypeptide chain through the central pore in the hexamer is the mechanism by which ESCRT-III subunits are exchanged or recycled [142]. Interestingly, there is also some evidence that Vps4 is also involved in the assembly of ESCRT-III polymers through subunit cycling. When fluorescently tagged Snf7 polymers are grown on a lipid bilayer in a microfluidics chamber, the addition of Vps2 and Vps24 inhibits further growth, while the addition of Vps4 and ATP negated this inhibitory effect, and in fact induced a dose-dependent increase in Snf7 polymer growth [153].

The yeast ESCRT-III subunits Vps24, Vps2, Vps20 and Snf7 are known to cooperate to form heteropolymers that are involved in membrane remodeling processes [124]. In contrast to the human homologs, there are no high-resolution structures of the yeast ESCRT-III proteins interacting with membranes, and it is unknown which protein, or proteins, may assemble, or co-assemble, around membranes and constrict them, and what the structural mechanism of this constriction could be. The investigation of these unknowns is the subject of this part of the PhD work.

4.2 Results

Note: Some of the figures in this section were taken from the publication [49]. All of these figures were prepared by me, and they are indicated by a star (*) sign in the figure legend. The

4.2.1 Protein purification

The Vps24, Vps20 and Snf7 constructs used were full-length, while the Vps2 construct used was truncated to use only residues 10-166, which does not contain the N-terminal helix α0, nor the C-terminal MIM that is required for interaction with Vps4. This truncated construct will from now on be referred to as Vps2ΔNC [131]. In the case of Vps2ΔNC, Vps24 and Snf7, following expression of each individual protein in E. coli and a subsequent nickel affinity purification (or amylose resin affinity in the case of Vps2ΔNC), the samples were not pure enough (Figure 4.6A). After tag removal and a reverse nickel affinity step, however, most contaminants remain bound to the nickel resin and the clean proteins were present in the flow through. The proteins migrate at a higher apparent molecular weight than their true size on SDS-PAGE (Figure 4.6B). This behavior is most likely due to the large number of charged residues in the proteins [139, 154]. During gel filtration on a superdex S200 16/600 column, the proteins elute as a single peak slightly earlier than expected (Figure 4.6C), probably given their elongated shape. Full length Vps4 was effectively purified by amylose resin and following tag removal, runs as expected on SDS-PAGE. The protein eluted as a single peak on gel filtration (Figure 4.6C).

Initial attempts of purifying Vps20 using an MBP fusion were unsuccessful because after tag removal, Vps20 and MBP co-eluted on gel filtration. This behavior is most likely due to the presence of large, charged patches on both proteins. After expression as a GST fusion, and purification by nickel affinity chromatography, the tag was cleaved and removed by a reverse nickel step. The resulting protein was clean and after gel filtration eluted as a single peak (Figure 4.7)

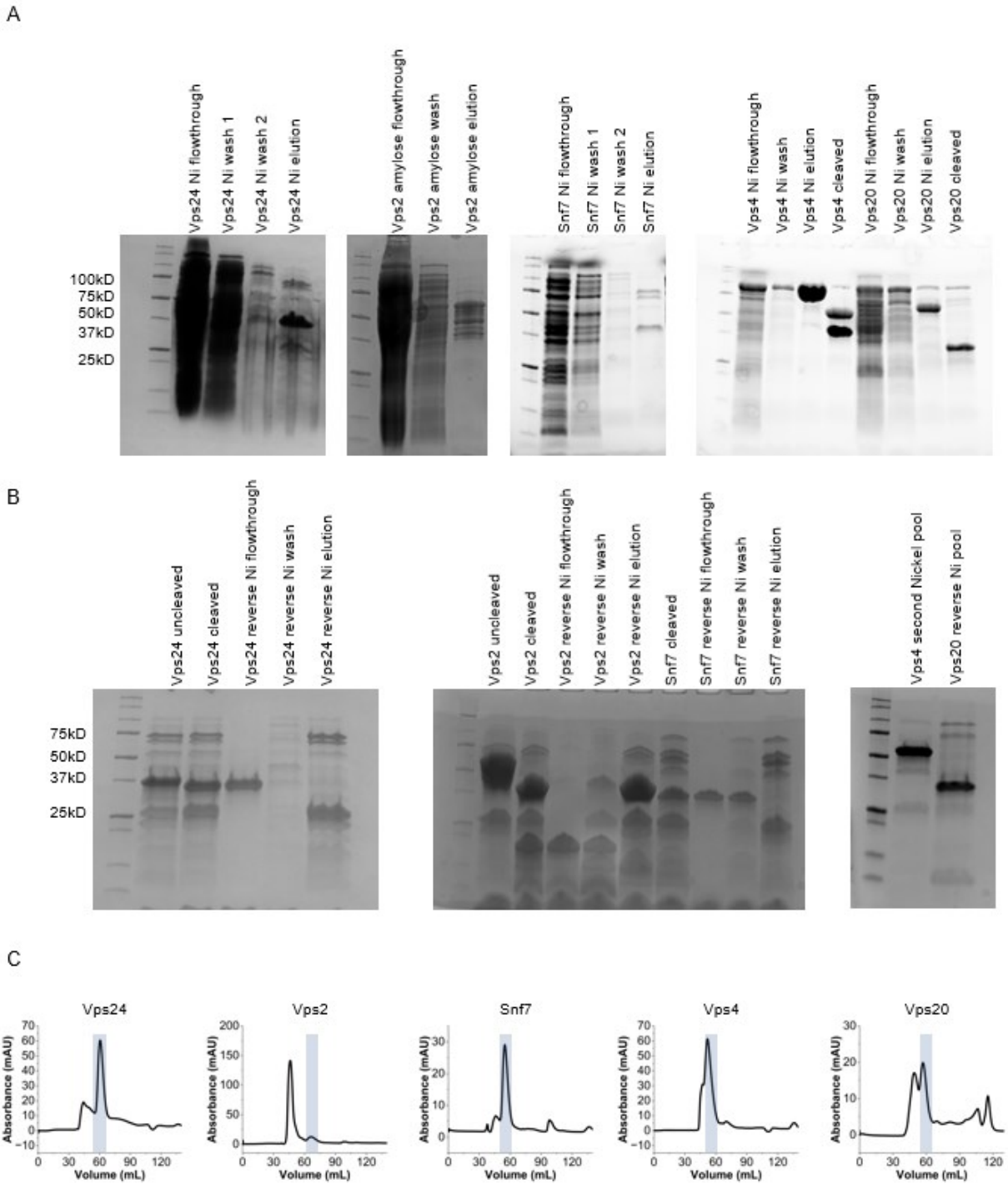

Figure 4.6: Protein purification results for ESCRT-III proteins

(A) SDS-PAGE analysis of the affinity purification of ESCRT-III proteins. (B) SDS-PAGE analysis of the reverse nickel chromatography steps following tag cleavage. Note that Vps4 has an uncleavable His-6x tag and will not flow through during this step, however the cleaved MBP tag is removed. (C) Chromatograms of the polishing gel filtration step. The fractions

pooled are shaded in blue. Note that Vps2ΔNC has a 0.1% absorption of 0.08, and thus the relative quantity as measured by A280 absorbance compared to contaminants is very low.

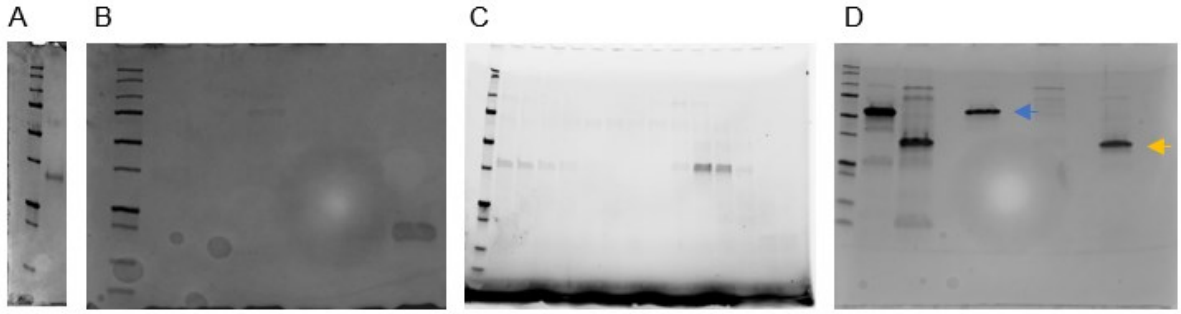

Figure 4.7: SDS-PAGE gels of purification of ESCRT-III proteins
(A) The Vps24 pooled sample after gel filtration. (B) Gel filtration fractions of Vps2ΔNC, the vast majority of the protein is present in a single fraction. (C) Gel filtration fractions of Snf7, the four fractions on the right side of the gel contain most of the protein. (D) Pooled fractions of Vps4 (blue arrow), and Vps20 (orange arrow).

4.2.2 ESCRT-III interaction with LUVs

4.2.2.1 Vps2ΔNC prevents Vps24 from forming filaments

In order to study the interaction between Vps24 and Vps2ΔNC, the two proteins were mixed in equimolar amounts and concentrated to 0.5, 1.0, 2.0 and 4.0 mg/mL, and then incubated for either one hour or overnight at 4 °C before being visualized by negative staining. As a control, Vps24 was concentrated in the same manner before being examined by negative stain. The results showed that Vps24 forms small filaments at 0.5 mg/mL after a one-hour incubation time, while after one day the filaments are larger and more abundant. In addition, after one day of incubation, patches of aggregated protein can be found on the grid. As the concentration of the protein increases, the number and length of the filaments increases with both incubation times. In contrast, the Vps24/Vps2ΔNC sample shows the formation of mostly aggregates at all concentrations and regardless of incubation time, and the noted absence of any filaments (Figure 4.8). These results suggest that Vps2ΔNC and Vps24 do indeed interact with each other, however the hetero-complex formed in this scenario is not filamentous.

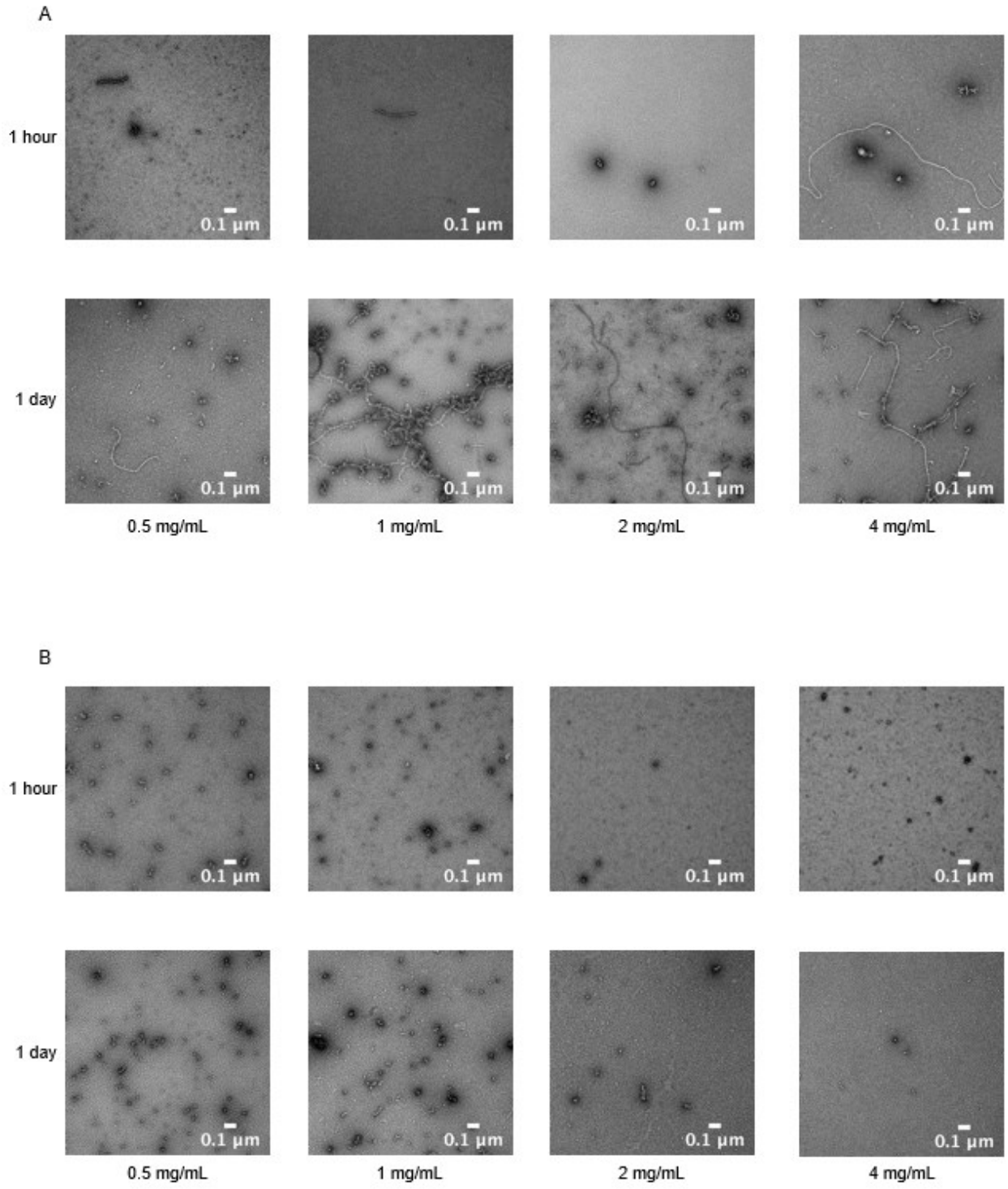

Figure 4.8*: Vps24 forms filaments at lower concentrations, while the addition of Vps2ΔNC prevents filament formation by Vps24.
(A) After Vps24 is concentrated, it is then incubated for either one hour or one day and then visualized by negative staining. After one hour, only the samples at the highest concentration formed filaments, however after one day of incubation, all tested concentrations were

sufficient for filament formation. (B) In contrast, when Vps24 and Vps2ΔNC are mixed before concentration and incubation, no filaments are formed regardless of incubation time and protein concentration. *Note: The top row of panel A in this figure uses the same micrographs as Figure S2 in [49], in which I am co-author. The micrographs and the original figure were made by me.*

4.2.2.2 ESCRT-III core complex proteins show interactions with LUVs in flotation and pelletation assays

In order to elucidate the functions of the yeast ESCRT-III core complex proteins, Vps2ΔNC, Vps24, and 6xHis-Snf7, the proteins were mixed in different permutations and concentrated to 3 mg/mL per protein. The samples were subjected to a liposome flotation assay. Initially, they were mixed with either a buffer control or large multilamellar vesicles (LUVs) prepared from a 3:1 molar ratio of DOPS:POPC. Subsequently, the sample was then added to the top of a sucrose gradient, and centrifuged at 174,000 × *g*, after which the sucrose gradient was fractionated into the top, bottom, and pellet fractions. LUVs, due to their low density, would be expected to be found at the top of the gradient, along with any other proteins that may bind to them. The samples were then separated by SDS-PAGE (Figure 4.9).

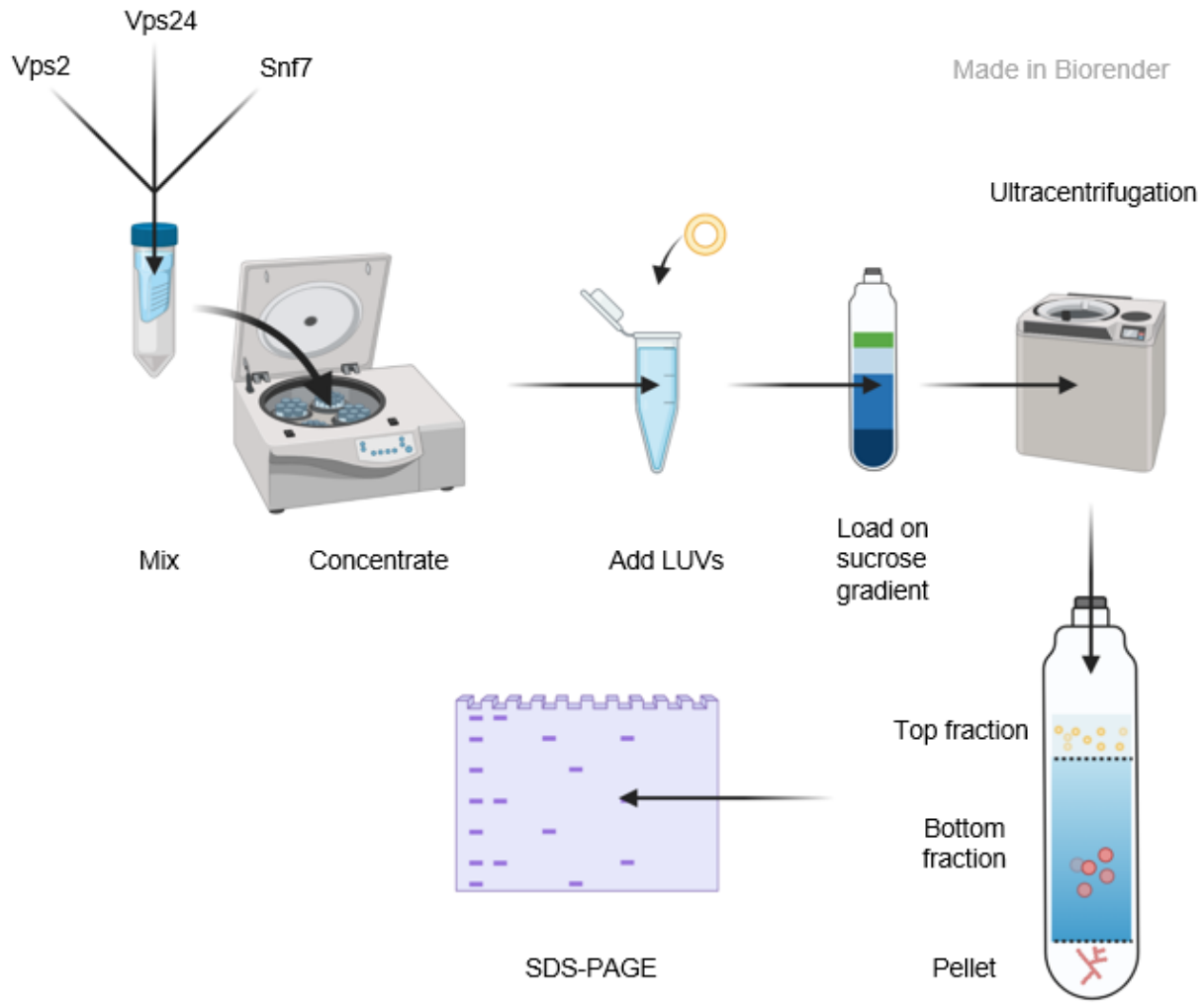

Figure 4.9: Overview of LUV flotation assay protocol
After the proteins are mixed and concentrated, they are incubated with LUVs and then loaded on a sucrose gradient. After ultracentrifugation, the sample is fractionated and analyzed by SDS-PAGE.

The results showed that with no LUVs added, all the proteins were found in the pellet (Figure 4.10). However, samples with LUVs showed that Vps2ΔNC and Vps24 either alone, or in combination with 6xHis-Snf7 would co-migrate with the LUVs into the top fraction, however 6xHis-Snf7 always remained in the pellet (Figure 4.10). This result was somewhat unexpected, as Snf7 is known to form spirals on membranes [155], however it should be noted that the protein shows aggregation visible to the eye when concentrated past ~0.2 mg/mL. The top fractions of the Vps24 sample and the triple complex of Vps2ΔNC/Vps24/Snf7 were

also examined by negative staining. The results showed that Vps24 exists as filaments in the top fraction alongside LUVs, and that in the case of the triple complex of Vps2ΔNC/Vps24/Snf7, the LUVs in the top fraction have been deformed into irregular tubular shapes (Figure 4.10).

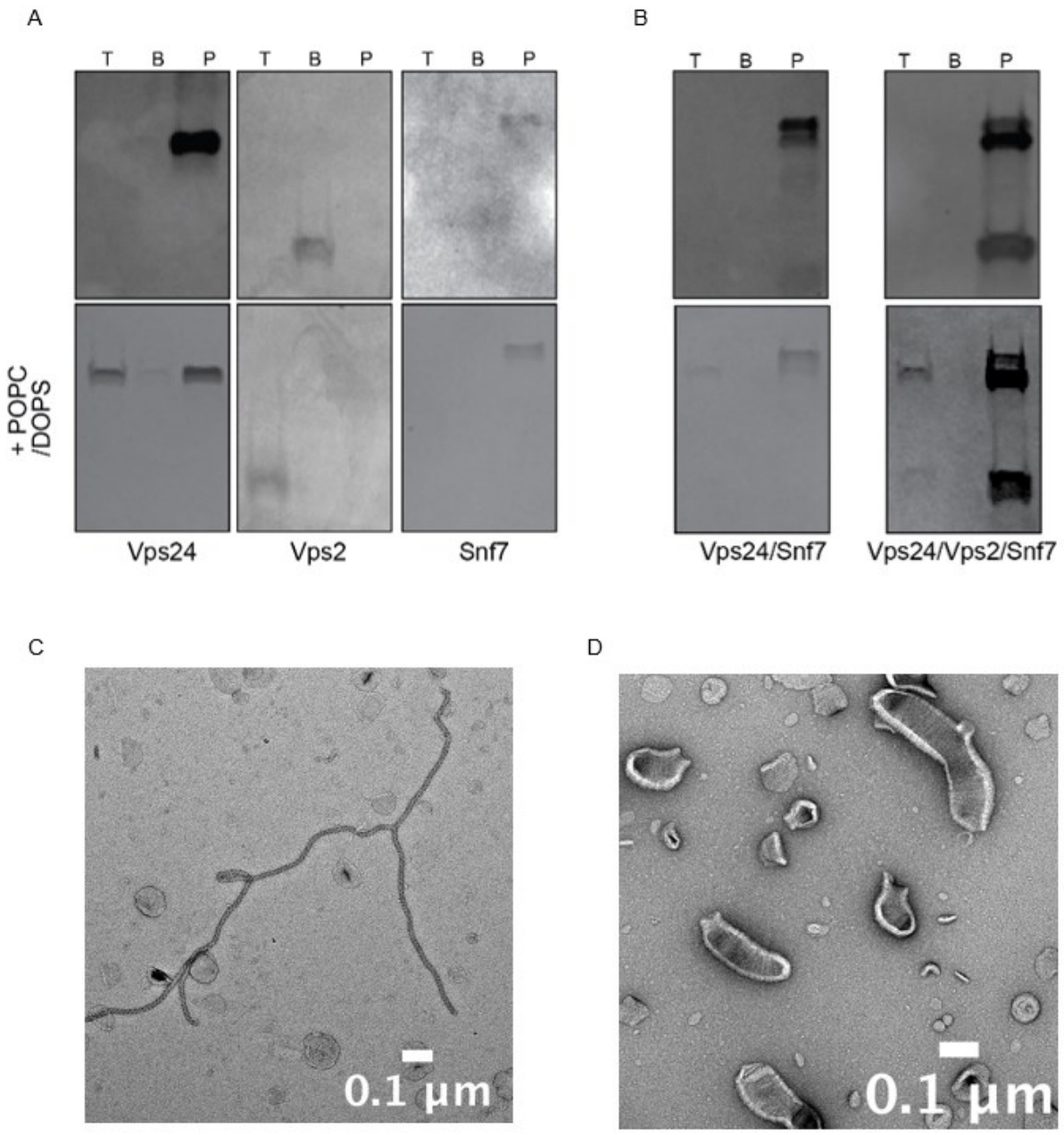

Figure 4.10*: Vps2ΔNC and Vps24, either alone or together, co-migrate with the liposomes to the top fraction in the LUV flotation assay, while the top fraction of the triple complex contains deformed LUVs

(A) When individual proteins are subjected to the assay without LUVs added, Vps24 and Snf7 stay in the pellet (lanes marked by 'P'), while Vps2ΔNC is present in the bottom fraction (lanes marked by 'B'). When LUVs are added, Vps2ΔNC and Vps24 are both present in the top fraction (lanes marked 'T'), while Snf7 is still in the pellet. This shows that Vps2ΔNC and Vps24 individually can interact with liposomes. (B) When all three proteins are mixed together and incubated with LUVs in the assay, only Vps2ΔNC and Vps24 migrate to the top fraction while Snf7 stays in the pellet. (C) Negative staining of the top fraction of the Vps24

flotation assay shows the presence of filaments directly interacting with LUVs, while in (D), the top fraction of the triple complex of Vps2ΔNC/Vps24/Snf7 shows the remodeling of the LUVs into tubular shapes. *Note: panels A and B in this figure were taken from Fig. 5 from [49], in which I am a co-author, and modified by cropping out of panels C and D in the original published figure. The original published figure was prepared by me.*

In addition to the wild-type (wt) Vps24, several charge reversal mutants of Vps24 were also tested for binding to LUVs via a LUV pelletation assay. The two mutants, K5D/K6D, K133D/E134A/K137D, and an additional construct missing the first 9 residues, Δ1-9 Vps24, were tested for filament formation and found not to form filaments at up to 10mg/mL concentration and overnight incubation (Figure 4.11). These proteins, and the wt-Vps24 as a control, were concentrated to 2 mg/mL and mixed with 3:1 DOPS:POPC LUVs (or a buffer control), incubated for one hour at 4 °C and centrifuged at 175,000 × *g* for one hour, then examined by SDS-PAGE which revealed that both the wt-Vps24 as well as the mutated forms were enriched in the pellet in samples with LUVs, compared to the buffer control (Figure 4.11). This shows that Vps24 interacts with negatively charged LUVs through multiple surface patches.

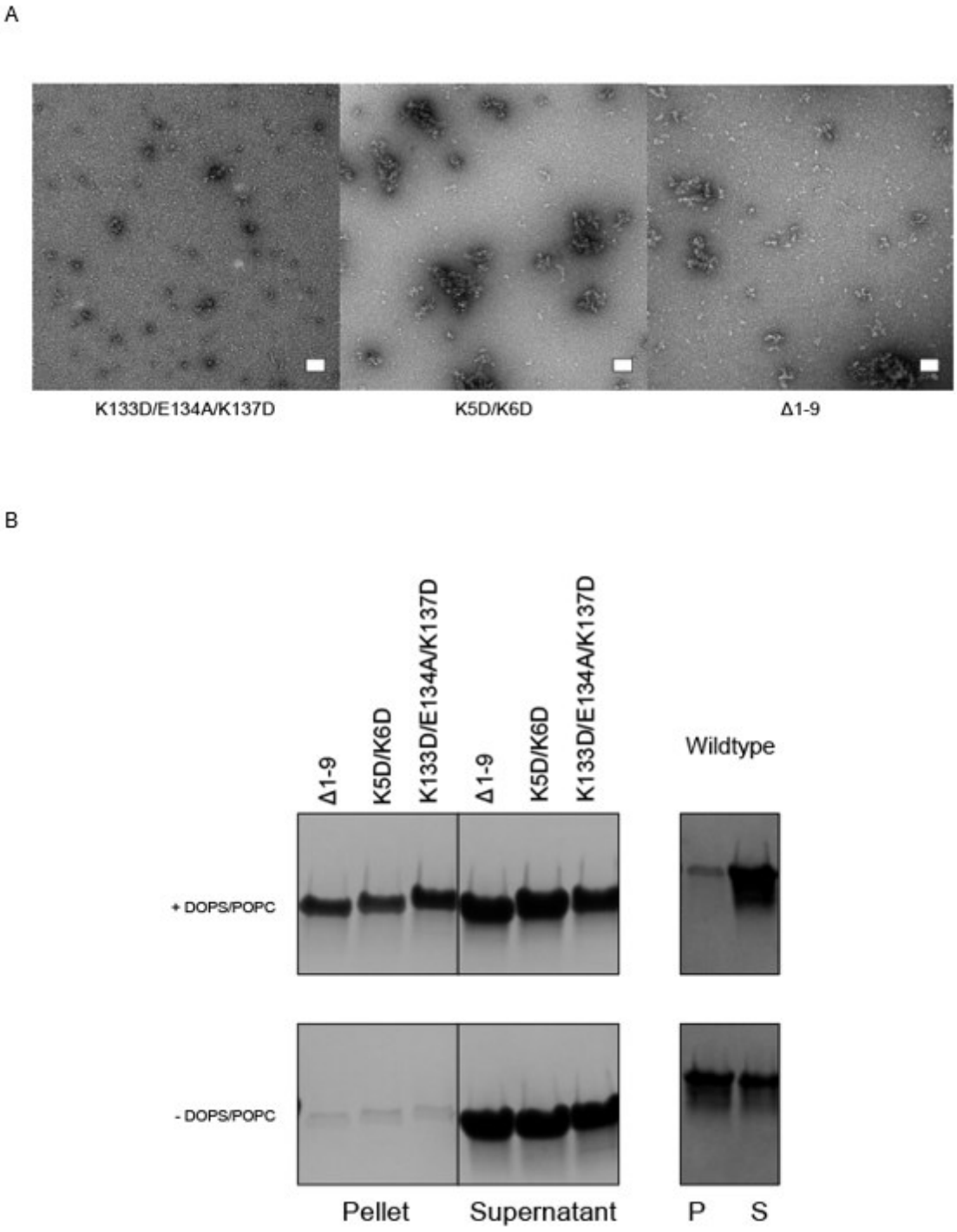

Figure 4.11*: N-terminally truncated or mutated Vps24 still interacts with LUVs
(A) There are no filaments formed when the mutated versions of Vps24 are concentrated and incubated. Scale bars 100 nm. (B) In the LUV pelletation assay, all mutants as well as the wild-type co-pellet with LUVs, showing that the interaction between Vps24 and negatively charged LUVs is driven by multiple distinct surface patches. *Note: the left-most image in panel*

A in this figure contains the same micrograph as the right-most panel in Figure S4 from [49], in which I am co-author. The micrograph and originally published figure were prepared by me. Panel B in this figure is taken from panel H in Fig. 4 in [49], in which I am co-author. The original figure was modified by rearrangement of panels and text.

4.2.2.3 ESCRT-III core complex proteins deform LUVs at low concentrations

During the liposome flotation assays, it was noticed that substantial protein aggregation visible by eye was present during the protein concentration step. For this reason, it was decided to try an alternative approach. In order to elucidate the potential role of Snf7, and its ability to interact with negatively charged LUVs, the three proteins, Vps2ΔNC, Vps24 and 6xHis-Snf7 were mixed with each other in different permutations and concentrated to 0.3 mg/mL per protein before being mixed with 3:1 DOPS/POPC LUVs and incubated overnight. For every 10µL of the protein, 3µL of the LUVs formed from lipids at 3 mg/mL were added, corresponding to a final concentration of 3µg of lipids per 1µg of protein. The samples were then examined by negative staining. The results showed that Vps24 by itself formed filaments alongside the LUVs (Figure 4.12A). They also showed that Vps2ΔNC/Vps24 complex caused the formation of neck-like structures on the LUVs (Figure 4.12A). In addition, the triple complex of Vps2ΔNC/Vps24/Snf7 showed the formation of tubular structures like those seen in the top fraction of the triple complex of Vps2ΔNC/Vps24/Snf7 flotation assays (Figure 4.12A), and under cryo-EM the tubes appear to have striations running alongside their length (Figure 4.12B).

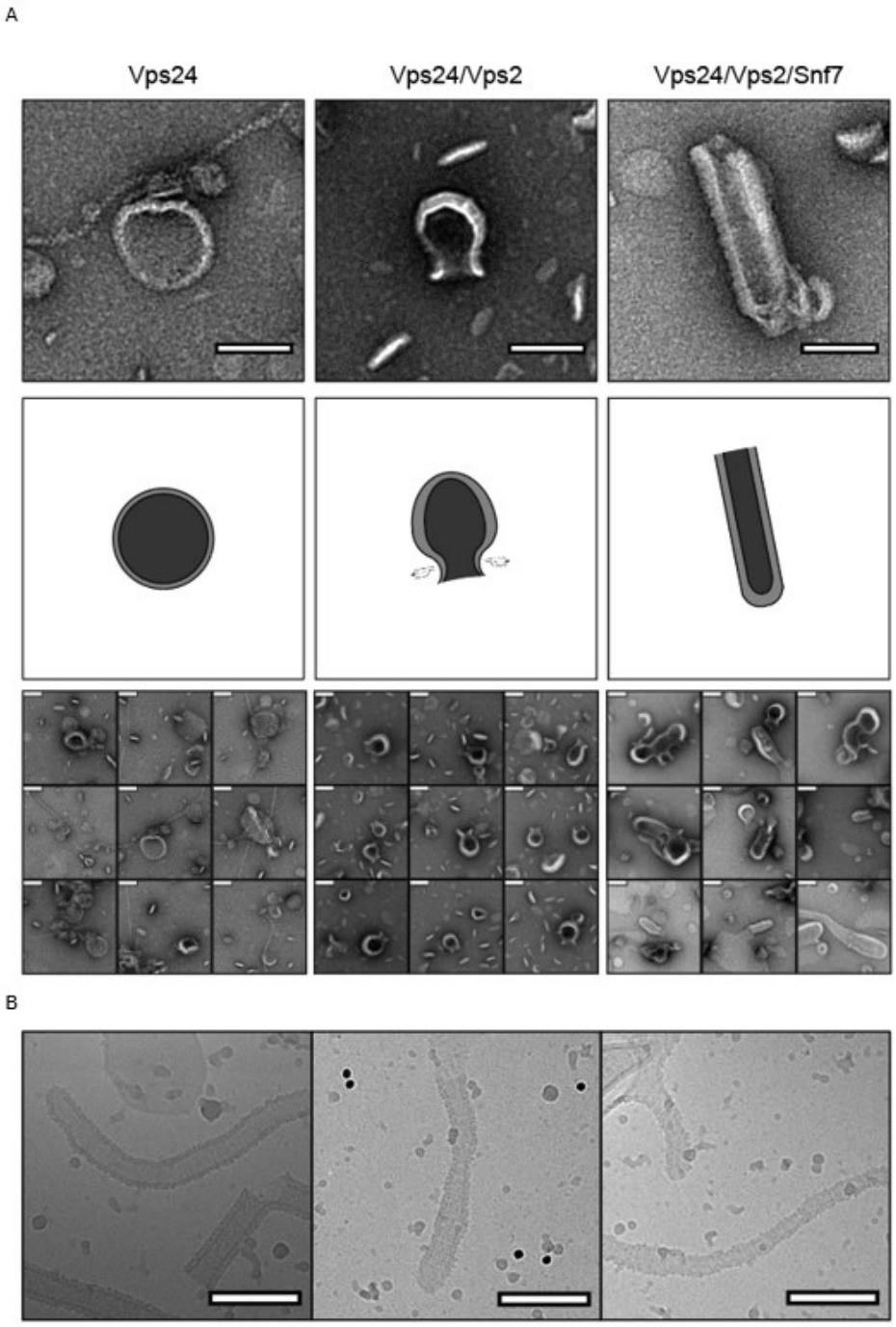

Figure 4.12*: ESCRT-III core complex proteins co-operate to induce neck formation and tubulation of LUVs at low concentration

(A) In the low-concentration assay, Vps24 forms filaments alongside LUVs, while Vps2ΔNC/Vps24 causes the formation of neck-like structures on the LUVs, and the triple complex of Vps2ΔNC/Vps24/Snf7 causes the formation of tubular structures (top), A cartoon diagram of the common shapes observed for each protein sample (middle), a gallery of negative-stained images showing the structures observed (bottom). (B) Cryo-EM images

of the triple complex of Vps2ΔNC/Vps24/Snf7 sample showing striations alongside the tubes as well as a potential double-membrane feature on the tubes. All scale bars 100nm. *Note: this figure was taken from panels C and D in Fig. 5 in [49], in which I am co-author. The original figure was prepared by me.*

4.2.3 Cryo-EM studies of the tubes formed by the deformation of LUVs by ESCRT-III core complex proteins

In order to examine the tubes, formed by the triple complex of Vps2ΔNC/Vps24/Snf7 upon their interaction with liposomes, under cryo-EM, the tubes were manually plunge-frozen on Quantifoil R2/2 grids using backside blotting and 8 or 10s of blot time. In addition, the tubes were plunge-frozen on a vitrobot using graphene oxide grids with 3s blotting time. Screening of the grids showed a single graphene oxide grid had good ice, although the particle density was very high with many overlapping tubes (Figure 4.13A). A dataset consisting of 400 movies was collected, motion corrected in WARP and imported into RELION for CTF estimation and manual particle picking. Due to the high density, only ~20 tubes could be picked. In addition, the tubes had very high heterogeneity in their width, ranging from less than 200 Å wide to over 400 Å wide. Another issue was the lack of the striations and visible protein coat seen on the tubes previously (Figure 4.13A). The only useful information that could be obtained was that the tube walls consisted of a double membrane (Figure 4.13B) Due to these problems, it was decided to try to biochemically optimize the tubes.

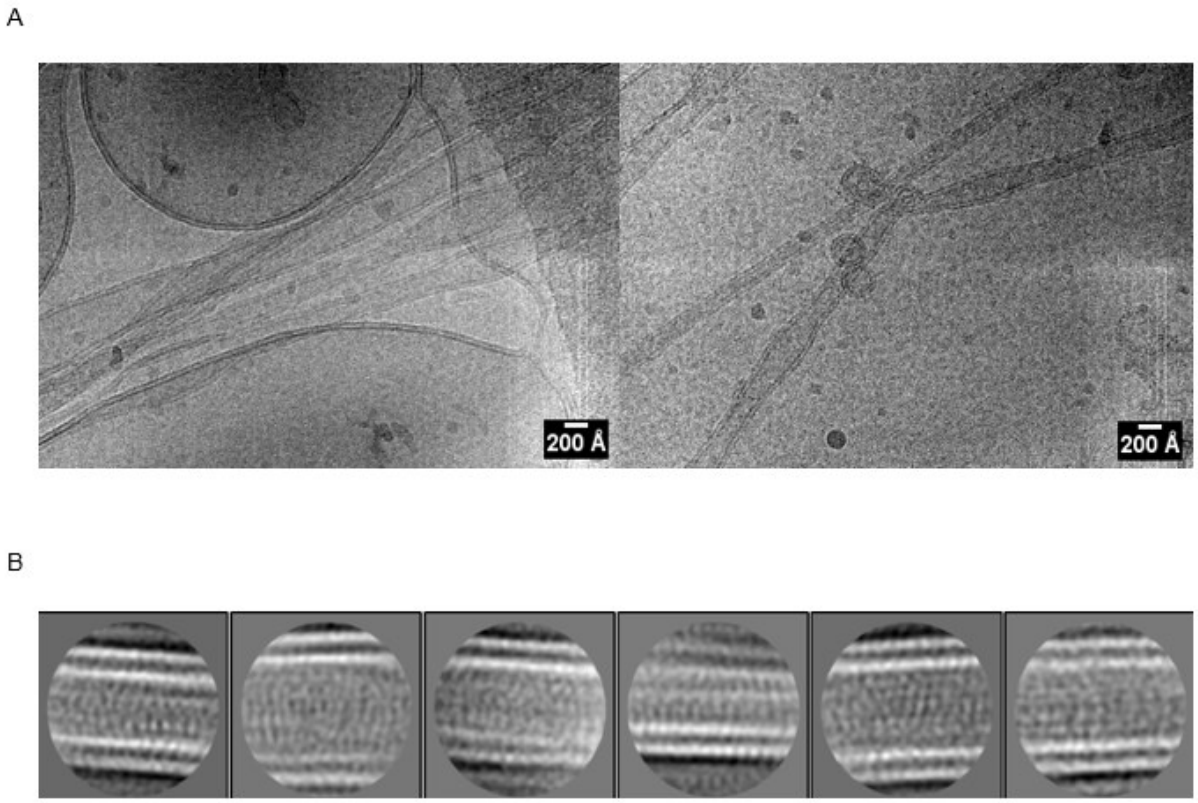

Figure 4.13: LUVs deformed by the ESCRT-III core complex show a double membrane under cryo-EM
(A) Example micrographs showing the heterogeneity in width present among the tubes, as well as the apparent lack of striations on the tube surface. (B) Results of 2D classification from manually picked particles showing the presence of a double membrane in the tubes, but no other distinguishing features.

4.2.3.1 Optimization of tubes to enable high resolution structure determination

While the tubes formed from the initial experiments were interesting, the lack of homogeneity would preclude structure determination. For this reason, several approaches to improve their properties were taken. The first step was the addition of Vps20 into the reaction mixture, alongside a pH and ionic strength screen, as well as switching to DOPS-only LUVs. In this approach, the triple complex of Vps2ΔNC/Vps24/Snf7 consisting of Vps2ΔNC, Vps24 and 6xHis-Snf7 concentrated to either 0.3 or 0.6 mg/mL per protein, and LUVs were prepared in either MES pH 6, or HEPES pH 8, and with 50 or 300mM NaCl (Figure 4.14). The

results showed that for the triple complex of Vps2ΔNC/Vps24/Snf7, at pH 6 and 300mM the tubes formed were longer, denser, and seemed to have some regularity along their length (Figure 4.14). Protein concentration seemed to have little effect, however both samples with 300mM NaCl were faster to concentrate and showed little sign of aggregation visible to the eye. The addition of Vps20 seemed to create more heterogenous tubes and was not considered helpful (Figure 4.14).

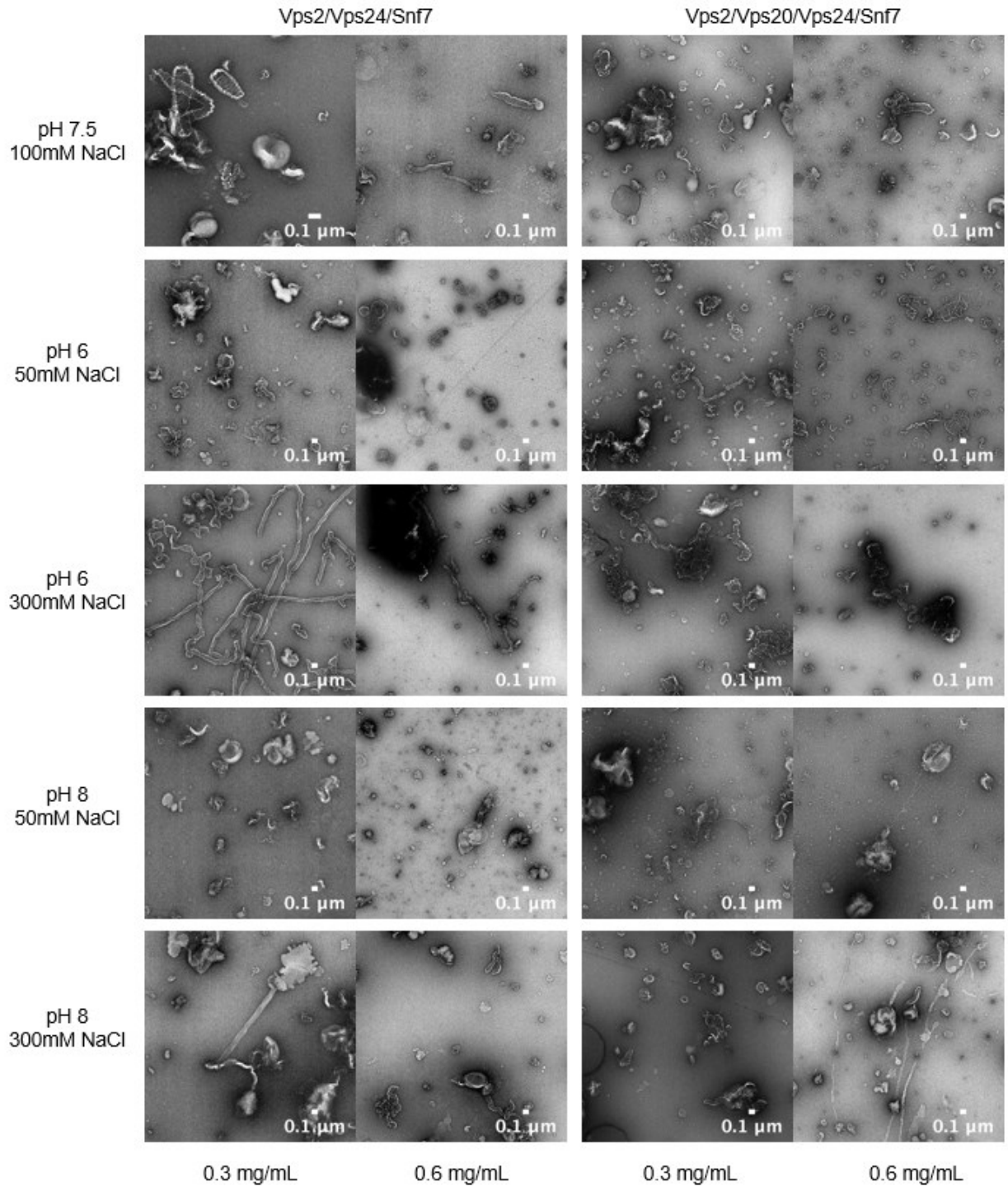

Figure 4.14: Results of buffer screening and Vps20 addition on ESCRT-III/LUV tubes
The screening of buffer conditions showed that the biggest improvements were made at both higher salt, as well as at pH 6 in the case of the triple complex of Vps2ΔNC/Vps24/Snf7. This conclusion is based on the overall density and appearance of the tubes formed. In contrast to the triple complex of Vps2ΔNC/Vps24/Snf7, the addition of Vps20 seems to lead to more

heterogeneous samples, with fewer tubes and more liposomes and other Irregular structures present.

4.2.3.1.1 Effects of nucleotides and Vps4 on tube morphology

It has been previously reported that N-terminally truncated Vps4 forms a hexamer in its active state, whereas the full-length protein is in an auto-inhibited state [151, 156]. In order to determine whether a similar behavior is present with the full-length protein, samples of Vps4 were prepared with either 1mM or 5mM AppNHp, a non-hydrolysable ATP analog, or 5mM ATP and examined by negative staining, which showed either monomers or other small proteinaceous particles with either nucleotide, and no higher order structures present (Figure 4.15A).

In order to test the effects of Vps4 on tube morphology, 5mM ATP or AppNHp was added to Vps4 at 0.5 mg/mL, after which it was added to the triple complex tubes formed at pH 6, 300mM NaCl. The sample was examined by negative staining, showing that in the reaction containing both Vps4 and ATP, the tubes had been depolymerized (Figure 4.15B). Even though no higher order structures of full-length Vps4 were observed in these experiments, the fact that the tubes were depolymerized suggests that the Vps4 protein in its full-length, non-oligomerized form is still catalytically active. In addition, since Vps24 is not known to bind to Vps4 [131], and the Vps2ΔNC construct used is missing the MIM domain required for Vps4 interaction, the interaction of Vps4 with the tubes must be driven by Snf7. Previously, truncations of Snf7, but not the full-length protein were shown to interact with Vps4 [145], which was hypothesized to be due to the closed conformation of the full-length protein.

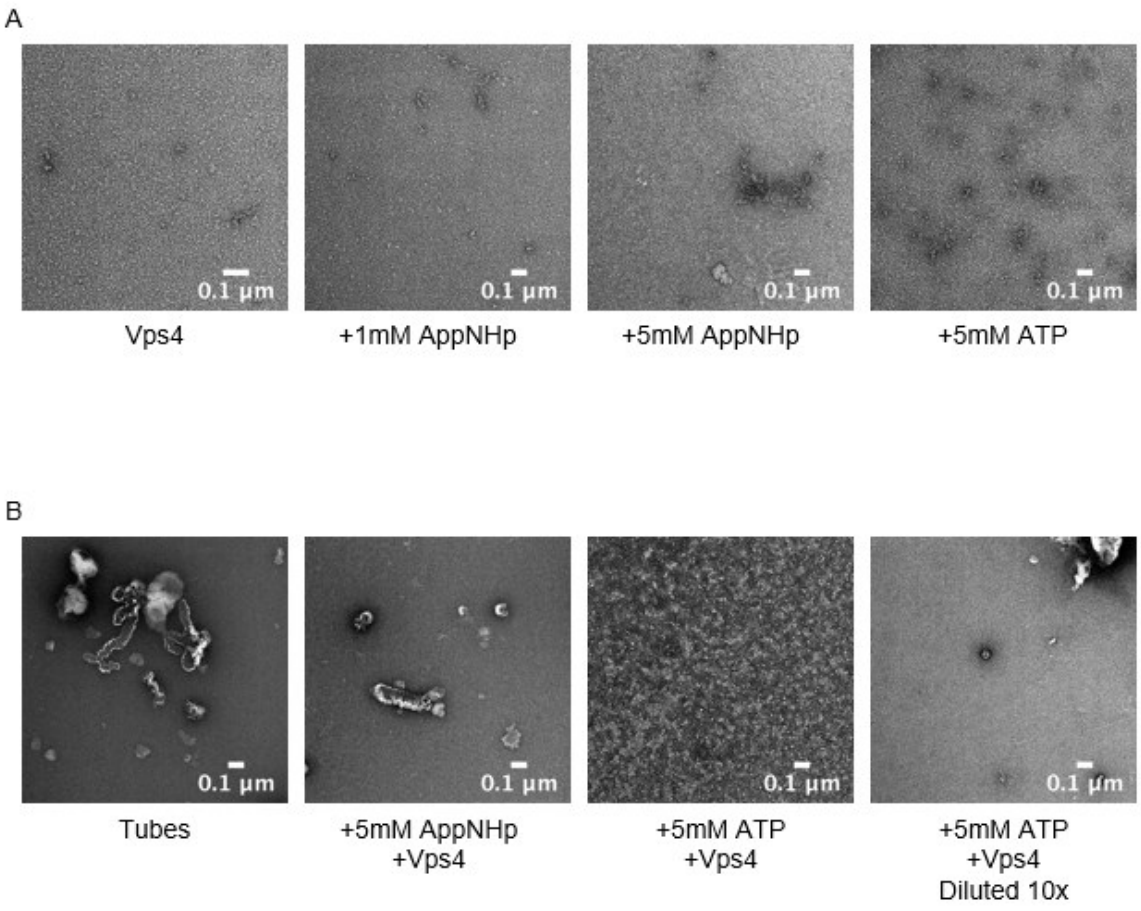

Figure 4.15: Vps4 causes the disassembly of tubes formed by the ESCRT-III core complex upon interaction with LUVs
(A) Full-length Vps4 does not form higher order oligomeric structures either alone or in combination with ATP or the non-hydrolysable ATP analog AppNHp. (B) The addition of Vps4 to pre-formed ESCRT-III triple complex of Vps2ΔNC/Vps24/Snf7 tubes does not cause depolymerization of the tubes with AppNHp, however the inclusion of ATP as the nucleotide causes depolymerization of the tubes, indicating that full-length Vps4 is catalytically active and is able to interact with the ESCRT-III tubes.

4.2.3.1.2 Divalent metal screening and Snf7 tag removal improve tube morphology

While the Vps2ΔNC and Vps24 proteins being used did not carry an N-terminal 6xHis tag, the Snf7 protein still had this tag attached. It was not removed previously since tag removal would reduce protein yield by ~80%. After scale-up, it was decided to work with the cleaved Snf7. In addition, since divalent metal cations are capable of binding to the

negatively charged lipids and modulate their properties such as fluidity, it was decided to screen the effect of a series of divalent cations on the tubes.

In order to form the tubes, the triple complex of Vps2ΔNC/Vps24/Snf7 proteins were mixed and concentrated to 0.3 mg/mL per protein. Separately, liposomes were prepared from DOPS lipid films. The distinction between these liposomes and LUVs is that the LUVs are extruded with a 200 nM membrane after the freeze-thaw step, but the liposomes are not extruded. This will create a wider variety of liposome sizes; however, the larger liposomes have lower membrane curvature which might make it easier for the proteins to begin the remodeling process. The following metals were added to the protein solution at 1 μM, 10 μM and 100 μM concentrations: $BaCl_2$, $Cacl_2$, $CoCl_2$, $CuCl_2$, $MgCl_2$, $MnCl_2$, $NiSO_4$, $PtCl_2$, VCl_2, $ZnCl_2$. The samples were then incubated for 15 minutes, after which the LUVs were added, and the sample was incubated overnight at 4 °C before being examined by negative staining. The results showed no improvement with most of the screened metals (Figure 4.16A), however the samples with $MnCl_2$ at 1 μM looked marginally better than the buffer control (Figure 4.17B). In addition, at 100 μM, $MnCl_2$ seemed to create odd, circular shaped structures out of what appear to be liposomes (Figure 4.16A). The largest improvement compared to previous preparations was in fact the tag removal of Snf7. Even in the buffer control without any metals added, the tubes looked substantially more homogeneous and regular compared to before (Figure 4.17). It was thus decided to use tag-free Snf7 as well as 1 μM $MnCl_2$ in future preparations.

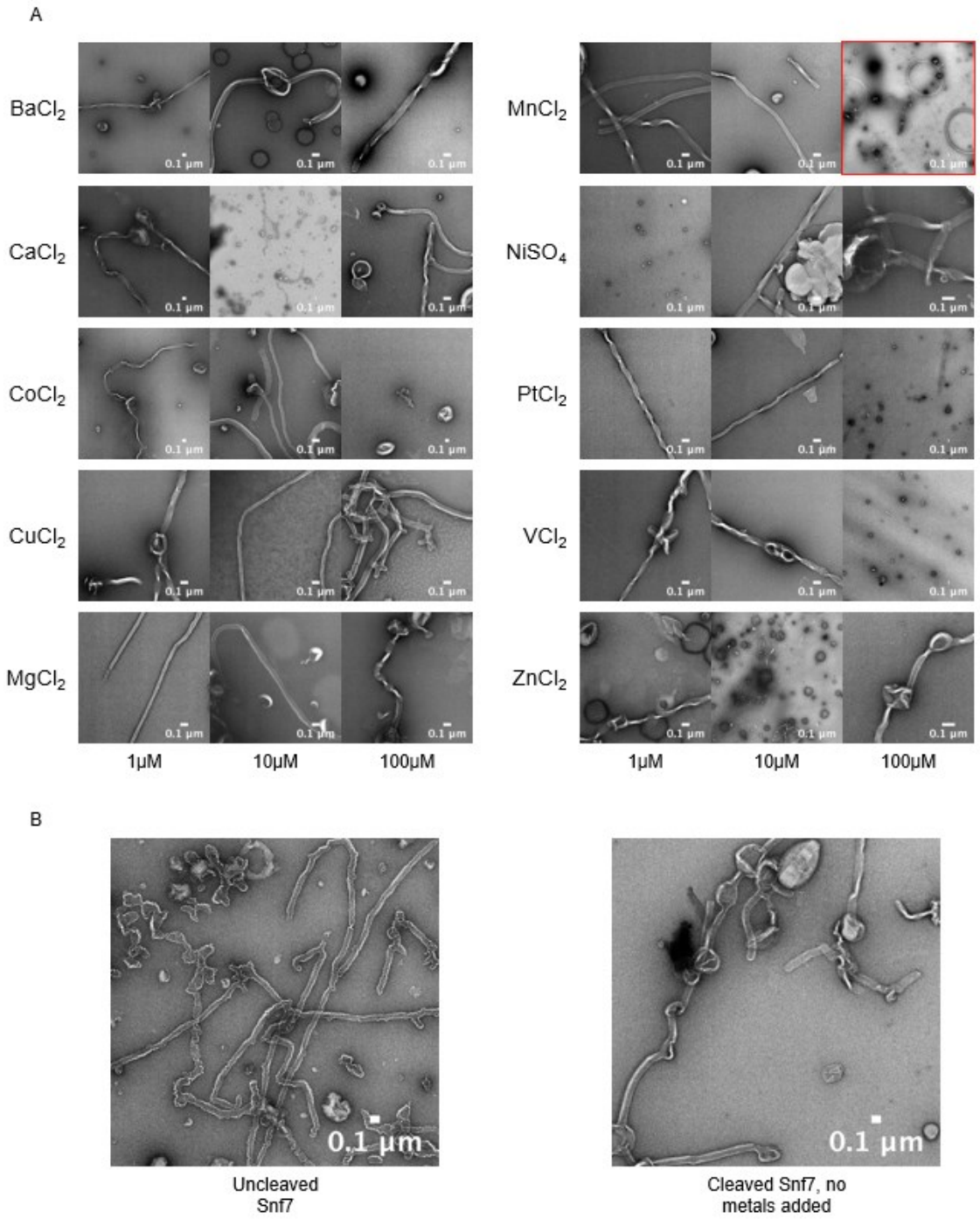

Figure 4.16: Effect of divalent cations and Snf7 cleavage on ESCRT-III tubes
(A) Most of the screened divalent cations did not substantially improve tube morphology compared to the no-metals control (panel B, right), and in fact high concentrations of $MnCl_2$ induced the formation of large ring-like structures (highlighted in red), (B) comparison of tube morphology of tubes formed with cleaved or uncleaved Snf7 shows substantial improvement in morphology in the sample with cleaved Snf7.

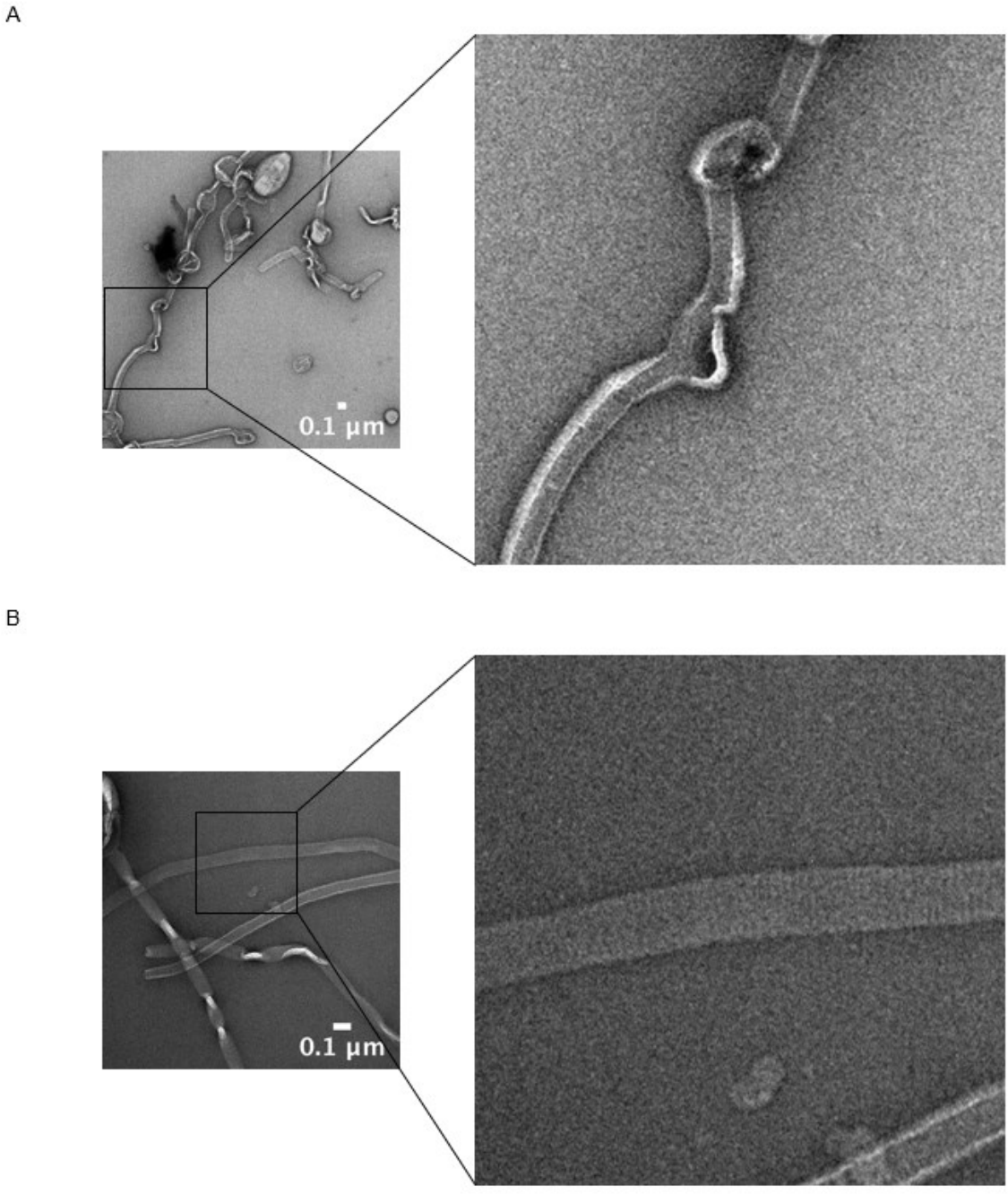

Figure 4.17: Effect of $MnCl_2$ on ESCRT-III tubes
(A) The tubes formed from the interaction of the triple complex Vps2ΔNC/Vps24/Snf7 with liposomes in the absence of divalent cations show some irregularity in their width and do not have visible striations, however tubes formed in the presence of 1 µM $MnCl_2$ (panel B), are straighter, appear to show a potential double membrane on their edges, and have visible striations along their length.

4.2.3.1.3 ESCRT-III core complex/lipid tubes can be concentrated and cleaned up by centrifugation

While the new tubes looked better, the concentration of the tubes was far too low to be suitable for cryo-EM grid preparation, since even undiluted sample on negatively stained grids still only contained only a handful of good tubes per grid square. In addition, it remained to be shown that using liposomes instead of LUVs was the prudent course of action.

As a first step, 400 µL of the tubes were prepared using DOPS liposomes with 1 µM $MnCl_2$. This sample was then centrifuged at 16,000 × *g* for 10 minutes, and the pellet was resuspended in 40 µL of buffer (pellet 1, Figure 4.18) and the supernatant was then centrifuged at 50,000 × *g* for 30 minutes, and the pellet was resuspended in 40 µL of buffer (pellet 2, Figure 4.18). Both pellets were examined by negative staining, which showed that much of the longer filaments as well as contaminating liposomes and large mats formed from intertwined tubes were in pellet 1 (Figure 4.19). In comparison, pellet 2 looked a bit better, however there were still smaller liposomes present (Figure 4.19). Both pellets were used to plunge-freeze Quantifoil and UltrAuFoil R 1.2/1.3 grids. The remaining sample from pellet 1 was used to perform a finer centrifugation screen (Figure 4.19). The results showed that most of the contaminants were pelleted at 5,000 × *g*, and there were no tubes remaining in the supernatant fraction of the last centrifugation step (Figure 4.19). Going forward, it was decided to centrifuge future samples at 5,000 × *g*, and then centrifuge the supernatant at 50,000 × *g* and use the pellet for plunging grids.

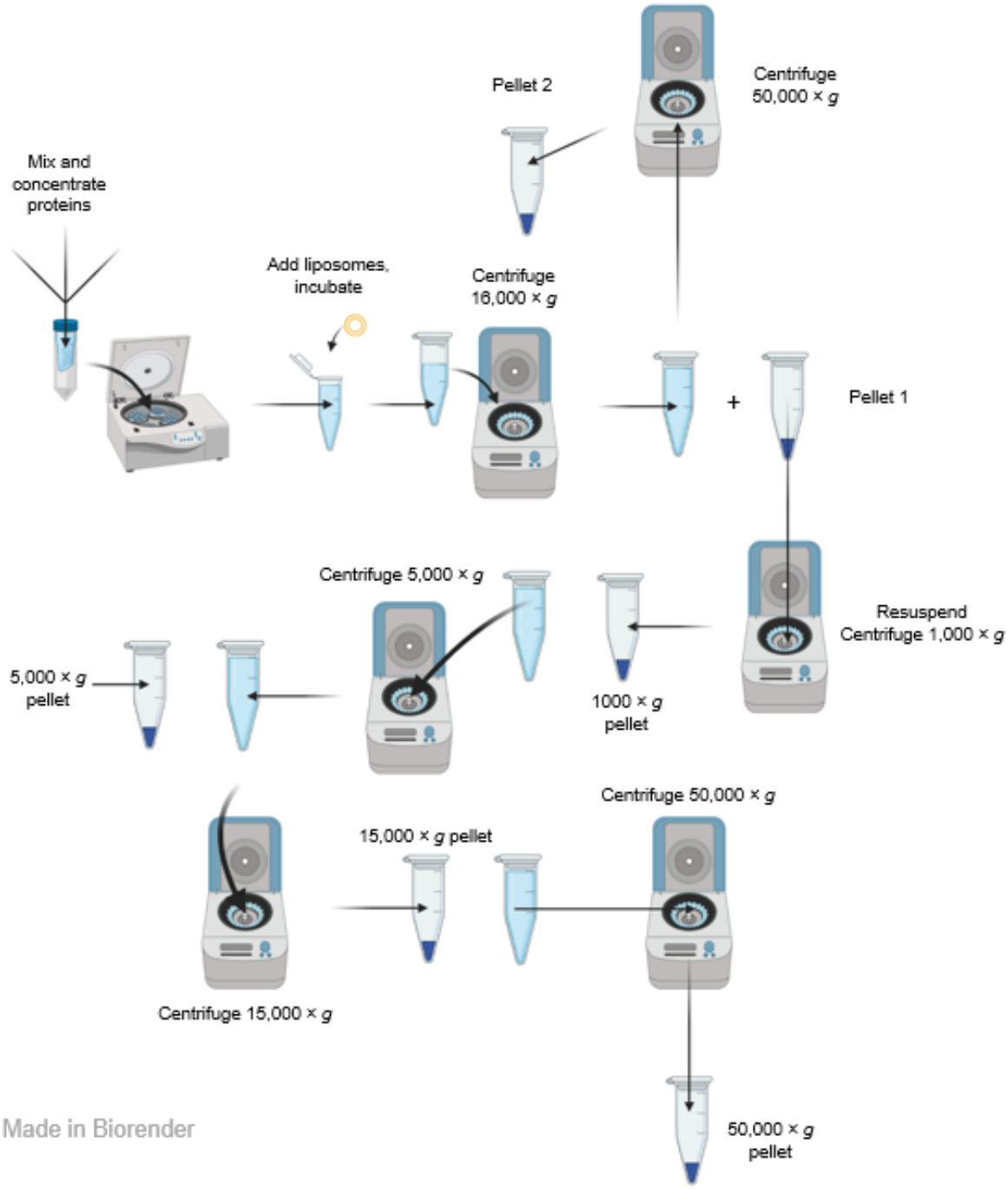

Figure 4.18: Protocol for concentration and cleanup of tubes
The tubes were initially concentrated by centrifugation at 16,000 × *g*, yielding Pellet 1. The supernatant of this centrifugation step was then centrifuged at 50,000 × *g*, which yielded Pellet 2. Pellet 1 was then resuspended, and the sample (30 µL) was diluted to 500µL and subjected to fractionation using centrifugation at 1,000 × *g*, 5,000 × *g*, 15,000 × *g*, and 50,000 × *g*. At each step, the pellet was saved for screening by negative stain, and the supernatant was centrifuged in the subsequent step.

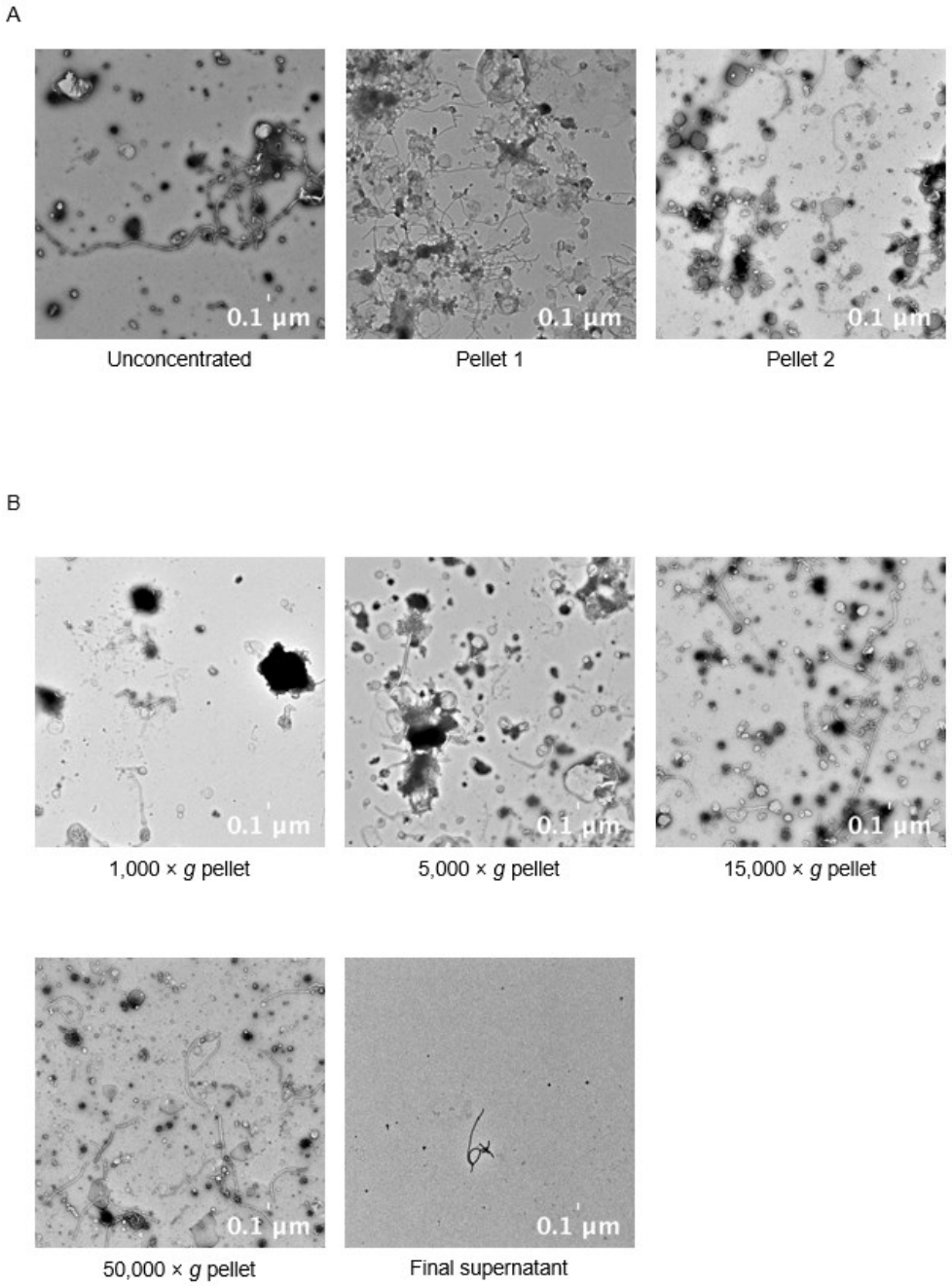

Figure 4.19: Results of concentration and cleanup of tubes
(A) The tubes are effectively concentrated by centrifugation; however, Pellet 1 contains many aggregated proteins and liposomes and other contaminating species. Pellet 2 looks slightly better but there are still many liposomes present in addition to the tubes. (B) A finer screen of centrifugation shows that many of the contaminating species in Pellet 1 are effectively removed by centrifugation at 5000 × *g*, and the subsequent two pellets look fairly clean. In addition, there is almost nothing left in the final supernatant, showing that there is good sample recovery at the final step.

4.2.3.1.3.1 Cryo-EM grid screening and dataset collection on ESCRT-III core complex/DOPS tubes

Cryo-EM grids were prepared using the Vitrobot mark IV (Thermo Fisher Scientific). In short, 3.5 µL of pellet 1 and pellet 2 were pipetted on either Quantifoil R2/2 or UltrAuFoil R1.2/1.3 grids and vitrified using plunge freezing. When imaged in the 200 kV Talos Arctica (Thermo Fisher Scientific) the micrographs of the grids prepared from pellet 1 appeared black; indicating an ice thickness that is too thick for the electron beam to penetrate. The grids prepared using pellet 2 looked much better and were used for subsequent analysis. The Quantifoil grids were mostly empty, but the AUfoil grids had decent particle density (Figure 4.20). A small dataset of 2400 movies was collected from this sample, motion corrected in WARP and imported into RELION for manual particle picking. The 2D classes showed extreme heterogeneity in tube width (Figure 4.20A), however a clear protein coat was visible on the edges of tubes in the form of 'teeth', as well as striations on the inside of the tubes (Figure 4.20B). Due to this heterogeneity, processing was stopped at this step.

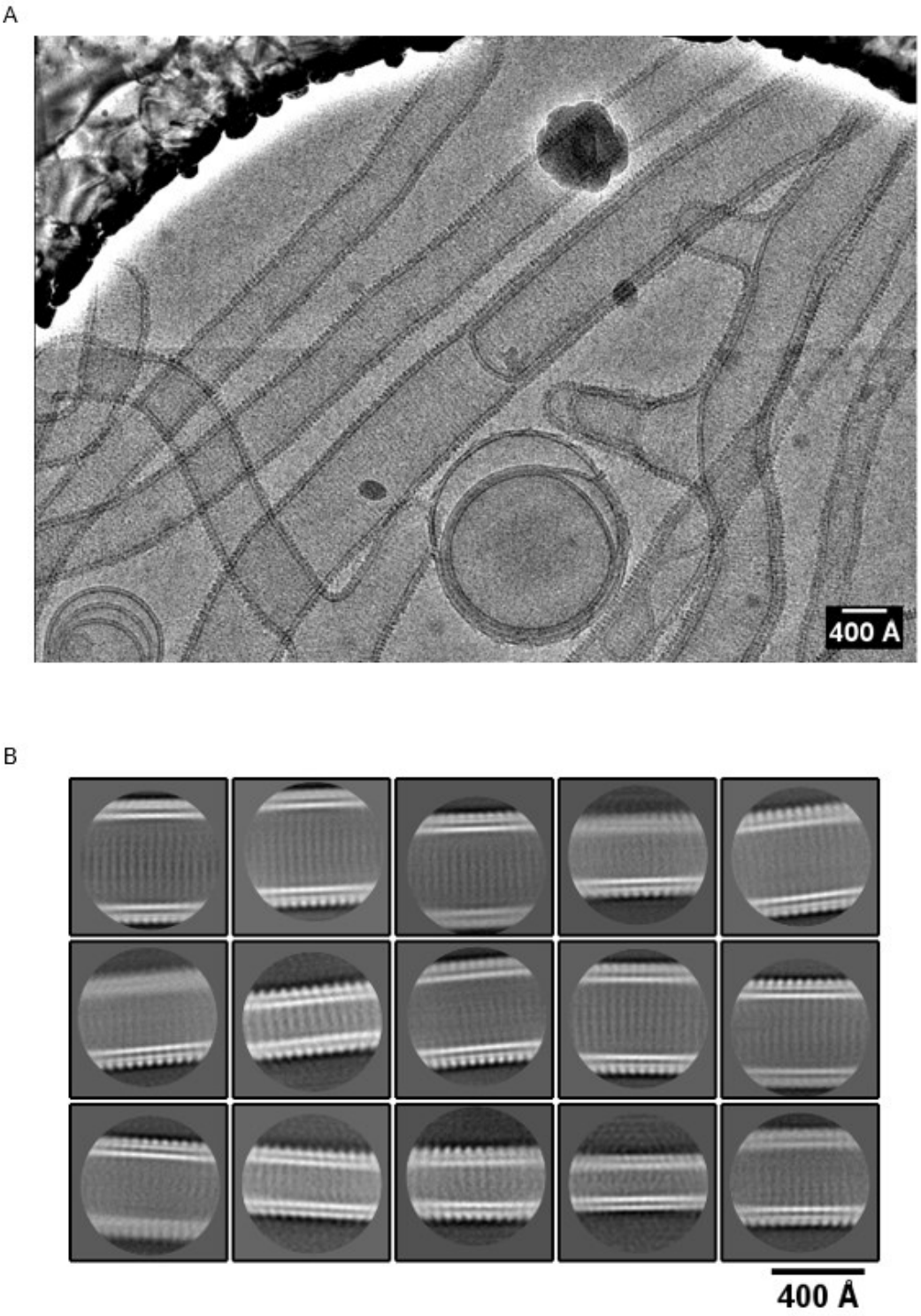

Figure 4.20: Overview of first dataset collected after optimization of DOPS/ESCRT-III core complex tubes

(A) Micrograph example showing the typical variation in tube width and morphology, as well as a visible protein coat on the tubes. (B) Results of 2D classification (~30,000 segments) after manual particle picking show visible teeth on the sides of the tubes, as well as variation

in width ranging from 300 Å to 600 Å. It should be noted that particularly wide tubes with widths over 800 Å were prevalent in the dataset, however they were not included in the manual particle picking.

4.2.3.1.3.2 Liposome extrusion and the effects of order of addition of the proteins

In order to determine whether using liposomes or LUVs resulted in more homogeneous samples, tubes were prepared using DOPS LUVs that were extruded with a 200 nm membrane. The sample was then spun at 5,000 × g and the pellet resuspended in 10% of the original volume. The supernatant was then spun at 50,000 × g and the pellet resuspended in 10% of the original volume. The results showed that the first pellet was mostly empty, and the large contaminating species were no longer present (Figure 4.21). The second pellet also looked fairly clean; however, the length of the tubes was substantially shorter than samples prepared using unextruded liposomes (Figure 4.21). There also appeared to be more variation in the width of the tubes (Figure 4.21). This pellet was used for plunge-freezing on UltrAuFoil R1.2/1.3 grids, and a small dataset of 800 movies was collected, motion corrected in WARP and imported into RELION for manual particle picking. The 2D classes looked very similar to the sample prepared from unextruded liposomes, however, the variation in width was still too high for high resolution 3D refinement (Figure 4.22).

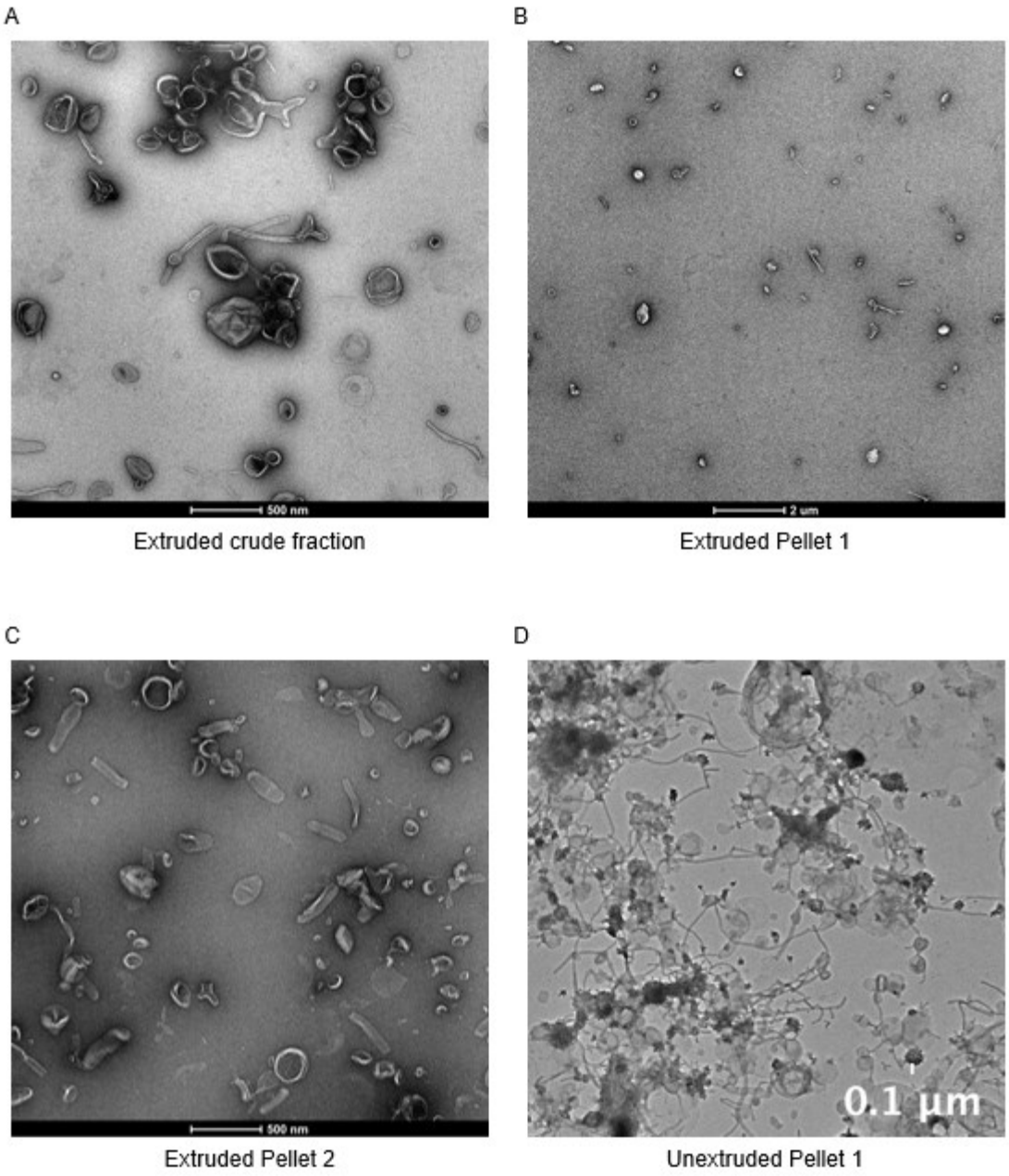

Figure 4.21: Effect of using LUVs instead of liposomes on tube morphology
(A) Shows the crude reaction mixture of the triple complex of Vps2ΔNC/Vps24/Snf7 and 200 nm extruded LUVs, about half of the LUVs have been remodeled into tubes of varying width and length. (B) Shows the contents of the first pellet after centrifugation at 5,000 × *g*, and (C) shows the pellet after centrifugation at 50,000 × *g*. In both of these pellets there is very little contaminating species and most of the LUVs and tubes are present in the second pellet. For comparison, (D) shows the pellet obtained after centrifugation at 16,000 × *g* from a tube preparation using unextruded liposomes instead of LUVs which contains longer tubes, but substantially more contamination.

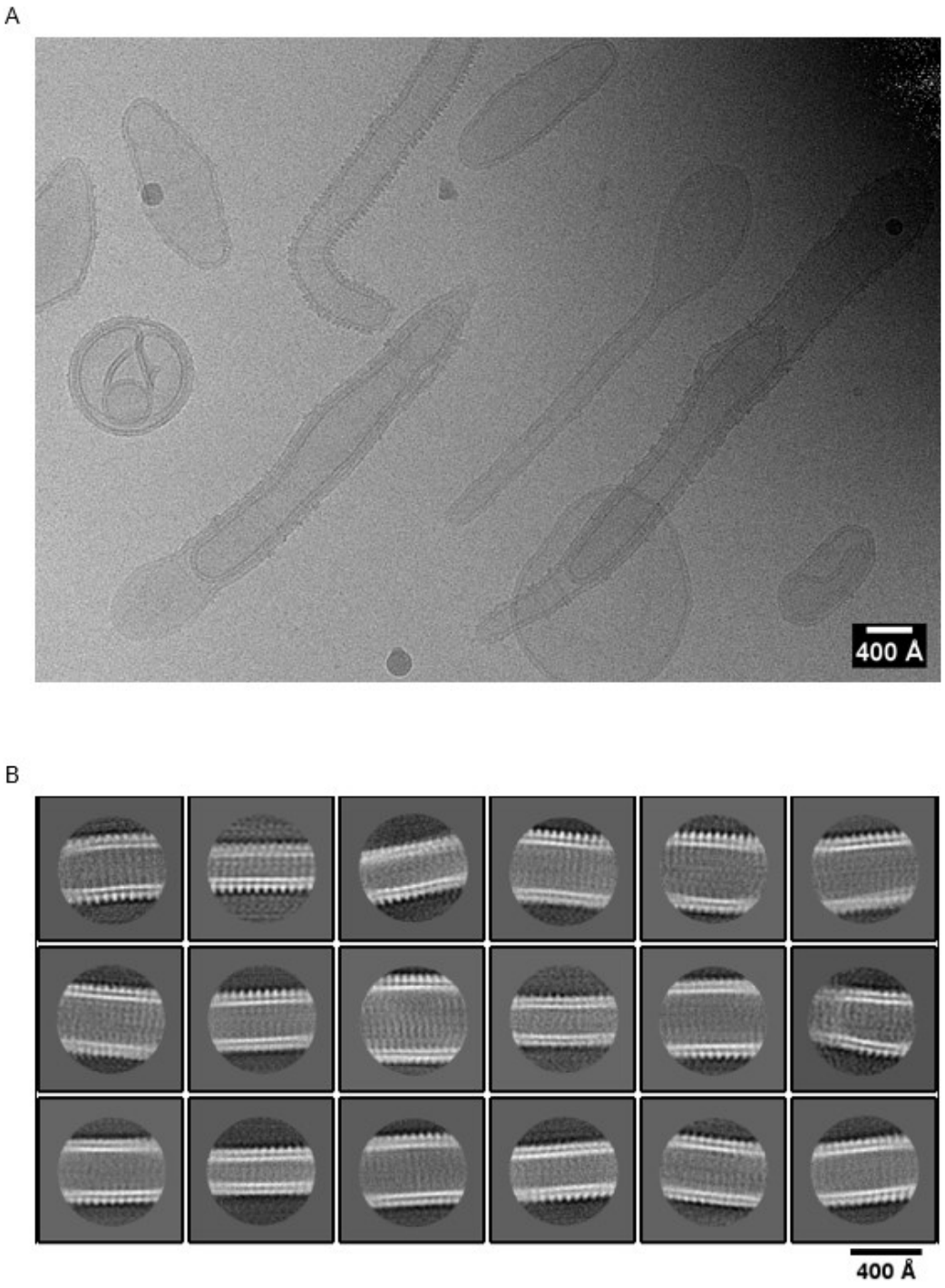

Figure 4.22: Extruded LUVs form heterogeneous and shorter tubes upon interaction with ESCRT-III core complex proteins
(A) Shows an example micrograph from this dataset, which compared to the dataset with unextruded liposomes (Figure 4.20) shows substantially shorter tubes. (B) results of 2D classification from manually picked particles (~7,000 segments) show that the tubes still

have large variation in width, however this variation does not seem to be as extreme as before (Figure 4.20).

4.2.3.1.4 ESCRT-III core complex proteins interact with membranes composed of yeast polar lipids to form structurally homogeneous tubes

As the next step, it was decided to use a more native lipid mixture by using yeast polar lipid (YPL) extract and yeast total lipid extract (YTL). The proteins were mixed and concentrated as before and mixed with liposomes prepared from either YTL or YPL and compared to a sample prepared from DOPS liposomes. The results showed odd-looking, irregular shapes in the YTL sample (Figure 4.23). In comparison, the YPL sample looked substantially better than the DOPS sample, with tubes that were straighter, more homogenous in width and with more visible structure under negative stain (Figure 4.23). From this sample, AUfoil R 1.2/1.3 grids were prepared after cleanup and concentration of the sample by centrifugation and resuspension of the pellet. After screening by cryo-EM, a dataset of 4000 movies was collected.

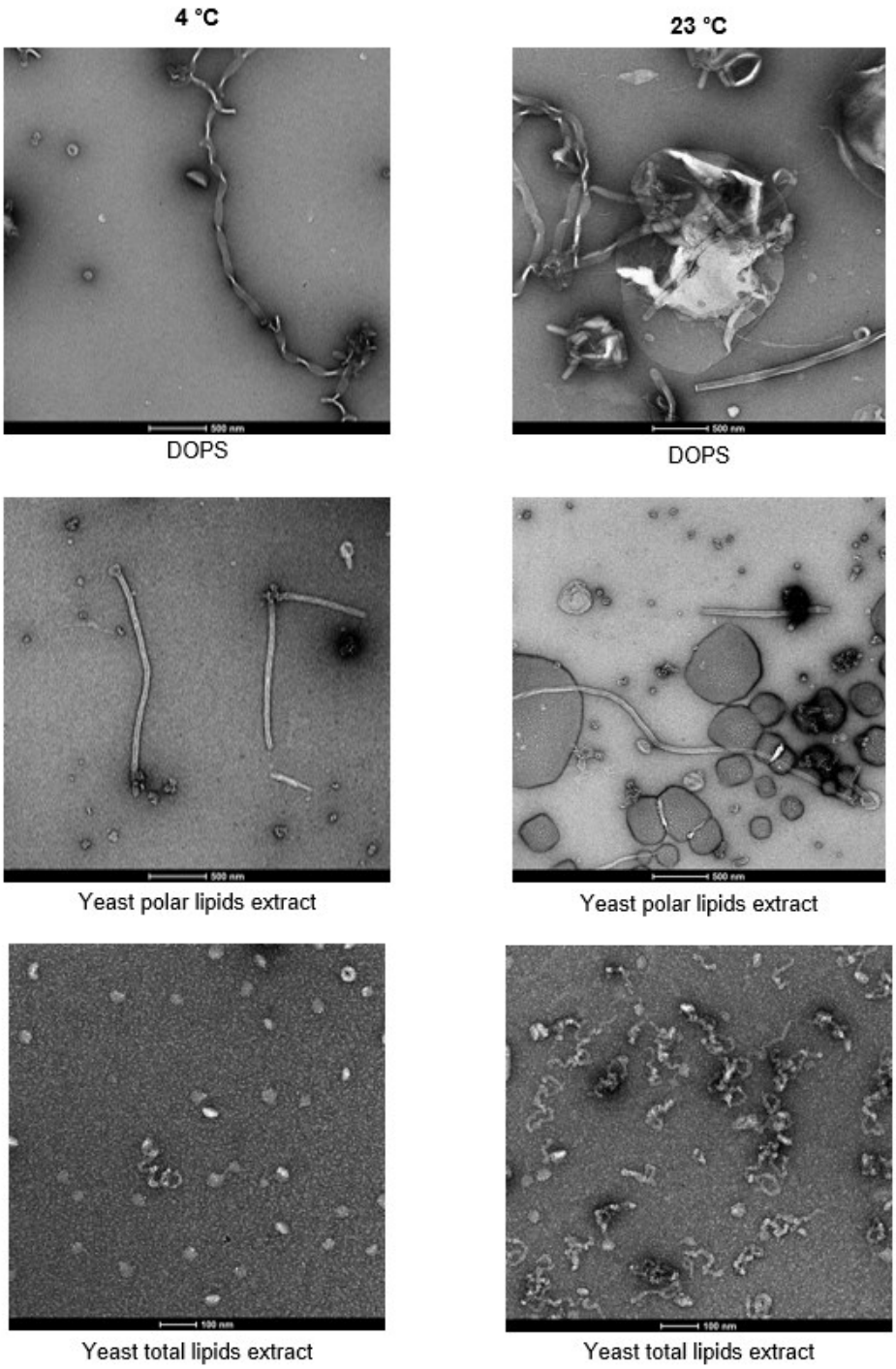

Figure 4.23: Yeast polar lipids interacts with the ESCRT-III core complex to form homogeneous tubes

The tubes prepared from yeast polar lipids extract (middle row) are substantially straighter and seem to have little width variation compared to tubes prepared from DOPS (top row). In contrast, the tubes prepared from yeast total lipids extract (bottom row) show substantial flexibility and even more heterogeneity than the DOPS sample. Note the different scale bars on the bottom row (100nm) compared to the other two rows (500nm).

In parallel, it was decided to test the effects of $MnCl_2$ and $MgCl_2$ on YPL and YTL tubes, as well as the effect of pH and the use of LUVs extruded with either a 200 nm or 1000 nm membrane. The results showed that tube formation is substantially worse at pH 6 compared to pH 7.5, the use of LUVs as opposed to unextruded liposomes is not helpful, and neither is the addition of $MnCl_2$ or $MgCl_2$ (Figure 4.24).

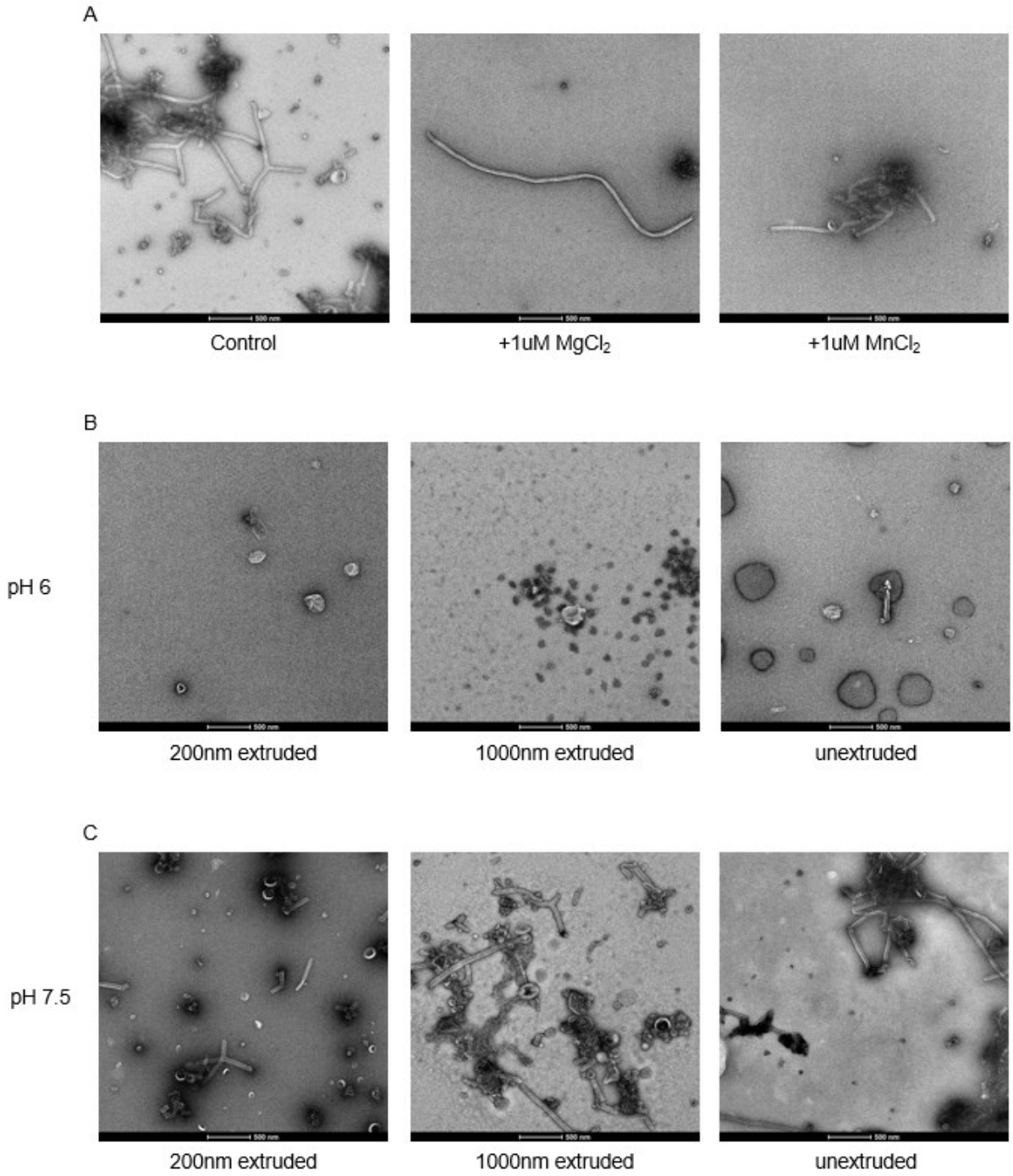

Figure 4.24: Effects of divalent cations and extruded LUVs on tube morphology
(A) The control tubes were prepared using YPL liposomes in 20 mM Tris-HCl pH 7.5, 300 mM NaCl as before. For divalent cation screening, after protein mixing and concentration, either 1 µM $MgCl_2$ or $MnCl_2$ was added to the protein mixture and incubated for 15 minutes before YPL liposomes were added and the samples incubated overnight at 4 °C. The results showed that both metals failed to substantially alter tube morphology, however the number of tubes was significantly decreased. (B) The proteins were mixed, and buffer exchanged into

20 mM MES pH 6, 300 mM NaCl and mixed with either LUVs extruded with a 200 nm or 1000 nm membrane, or unextruded liposomes in the same buffer. The results showed a substantial deleterious effect on the sample and the lack of any tubes. (C) In comparison, at pH 7.5, the use of 200 nm extruded LUVs led to substantially shorter tubes compared to the sample using 1000 nm extruded LUVs or unextruded liposomes, which looked similar.

The 4000 movies were imported into RELION for motion correction. The motion corrected micrographs showed that there was substantial radiation damage present on many of the tubes, even at a dose of 40 $e^-/Å^2$. For this reason, only the first 25 of 40 total frames were used for the next round of motion correction. Additionally, while particle density was good in some holes, most of the holes were either empty or too dense, meaning that only a small subset of the data collected was Useful. After CTF estimation, tubes were manually picked in RELION from all micrographs and overlapping (90%) segments were extracted with box sizes of either 700 Å or 1000 Å. The results of the 2D classification showed that the tubes still had some variation in width, which was nonetheless a substantial improvement over the previous preparations (Figure 4.25). The 2D classes also showed a protein coat on the outside of the lipid tube as well as striations along the inside of the tube, however no protein secondary structure could be seen. The use of a much smaller mask (250 Å) that focused on the central portion of the tube showed what appeared to be either secondary structure or individual subunits (Figure 4.25). Manual counting and back-Calculation of the number of subunits based on a tube width of 400 Å (thus circumference of ~1250 Å), suggested ~36 units per turn.

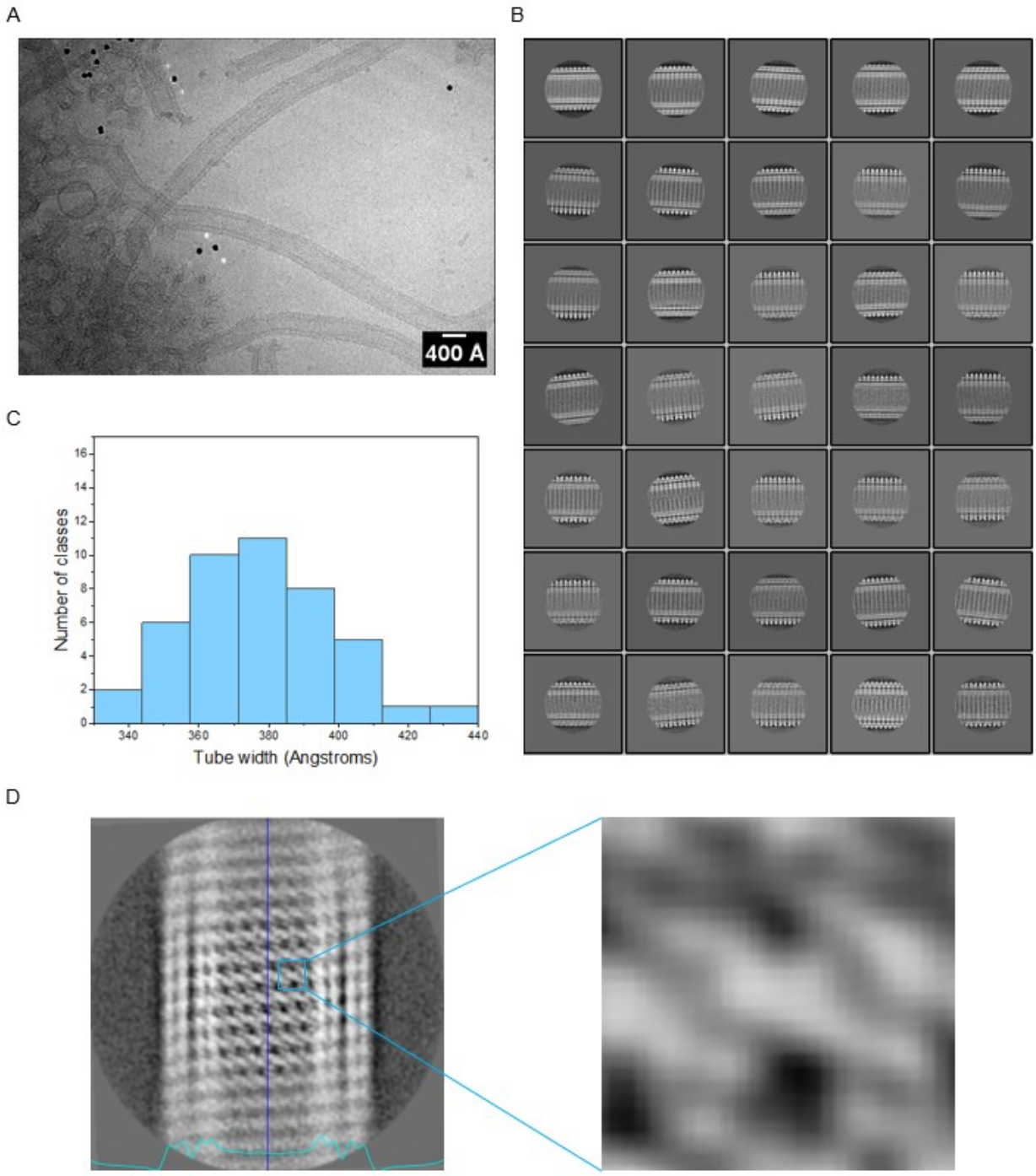

Figure 4.25: Tubes prepared from YPL and the ESCRT-III core complex show medium-resolution structural details

(A) An example micrograph showing overall tube morphology. The black dots are gold fiducials, the streaks on the top right are due to a problem with the gain on the camera. (B) Results of 2D classification in RELION after cleanup, showing the presence of striations along the tubes as well as indentations resembling teeth on the outside of the tube, corresponding to the protein coat. The circular mask diameter is 500 Å, and there are ~47,000 segments among the classes in total. (C) A histogram of the measured tube widths shows there is still

some heterogeneity, however it is substantially more uniform than in any of the DOPS datasets (compare with Figures 3.20 and 3.22) (D) After classification with a 250 Å circular mask, the unmasked class average shows what appear to be individual subunits.

The extracted segments were then imported into CryoSPARC. The 2D classes in CryoSPARC showed much better detail and high-resolution features, however no secondary structure could be observed (Figure 4.26). Analysis of the power spectra suggested a repeat distance of ~80 Å. Attempts were made through 2D classification to select a good subset of particles with higher resolution features, however in the end the single best 2D class only had ~6000 particles (Figure 4.26), which could not be enough for high-resolution structure determination. In addition, there were no classes present that showed a protein coat on the inside of the tube (Figure 4.26), which contradicted the generally accepted mechanism of action of ESCRT-III proteins, i.e., invagination of the membrane surface [135]. It was thus decided to alter the tube formation protocol and to also collect a much larger dataset.

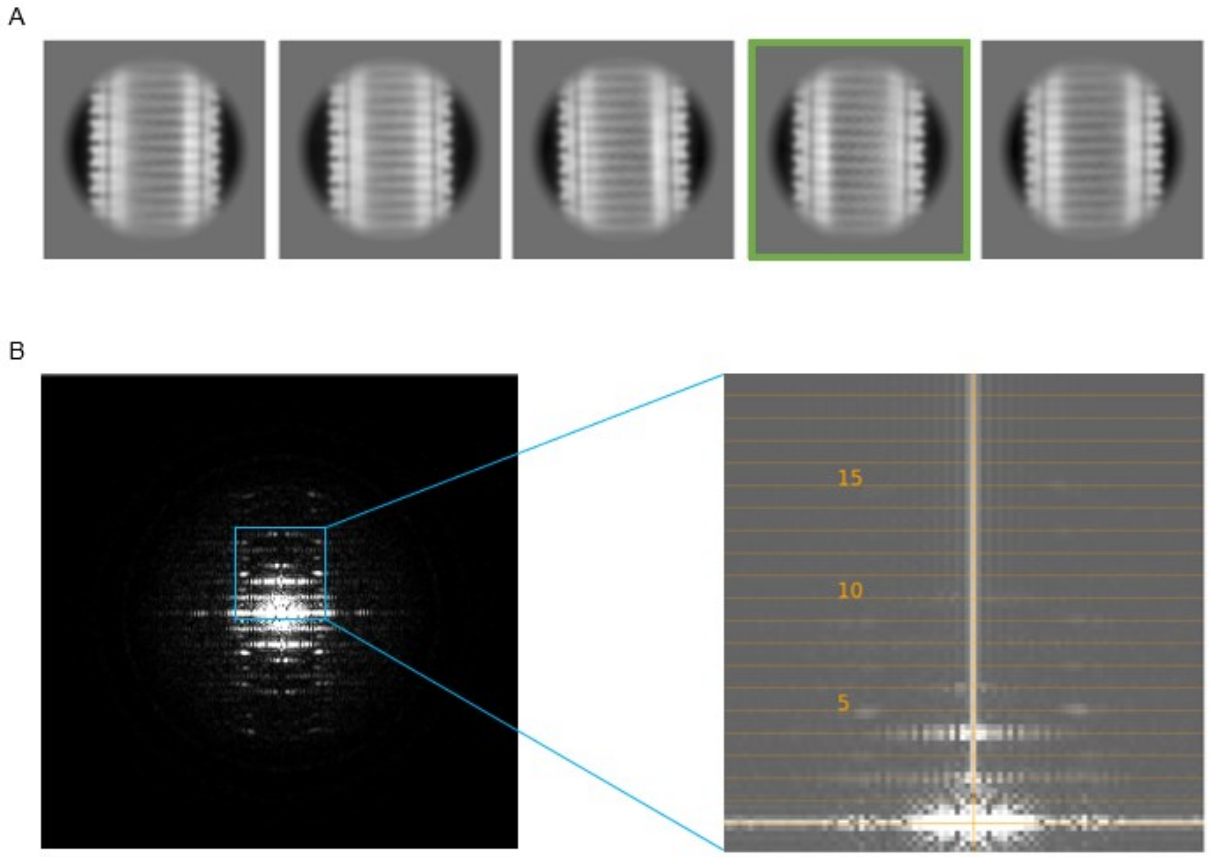

Figure 4.26: The tubes formed by YPL/ESCRT-III interaction show a repeat distance of 80 Å
(A) The best five classes from CryoSPARC show more detail than the classes in RELION. (B) The power spectra of the class highlighted in green in panel A, layer lines drawn every 4.25 pixels, corresponding to a repeat distance of 80 Å, are shown.

4.2.3.1.5 Direct resuspension preparation method

Previous publications [157] have shown that proteins can be trapped inside liposomes if the lipid film is resuspended directly in the protein solution, although the efficiency is not very high [157]. In order to examine whether the yeast ESCRT-III proteins could also drive membrane remodeling from the inside of the liposome, and thus remodel positively curved membranes, the YPL lipid film was directly resuspended in a mixture containing Vps24/Vps2ΔNC/Snf7 at a concentration of 0.15 mg/mL per protein. The results as visualized by negative staining initially showed a significant increase in the number, length, and flexibility of the tubes formed (Figure 4.27A). This method of sample preparation will be referred to as the direct resuspension protocol.

Since it appeared that the direct resuspension protocol is more efficient at producing tubes, an experiment was performed to quantify this increase in efficiency. The rationale was that a series of reactions could be set up using both protocols, with decreasing protein concentration. At some concentration, tube formation would not happen, and this concentration would be different for the two protocols. For this experiment, the amount of lipid used by mass was kept constant and only protein concentration was varied. Furthermore, since there is a smaller lipid to protein ratio in the liposome-addition protocol compared to the direct resuspension protocol, the lipid amount was increased by a factor of 4.5 for the liposome-addition protocol in order to match the lipid to protein ratio of the direct resuspension protocol. The three proteins (Vps2ΔNC/Vps24/Snf7) were mixed and concentrated and either added to liposomes or a lipid film and incubated at room temperature for one hour before being visualized by negative staining. The results showed that both protocols are equally effective at forming tubes and that the apparent increase in efficiency with the direct resuspension method is solely due to the larger relative ratio of lipids present (Figure 4.27B).

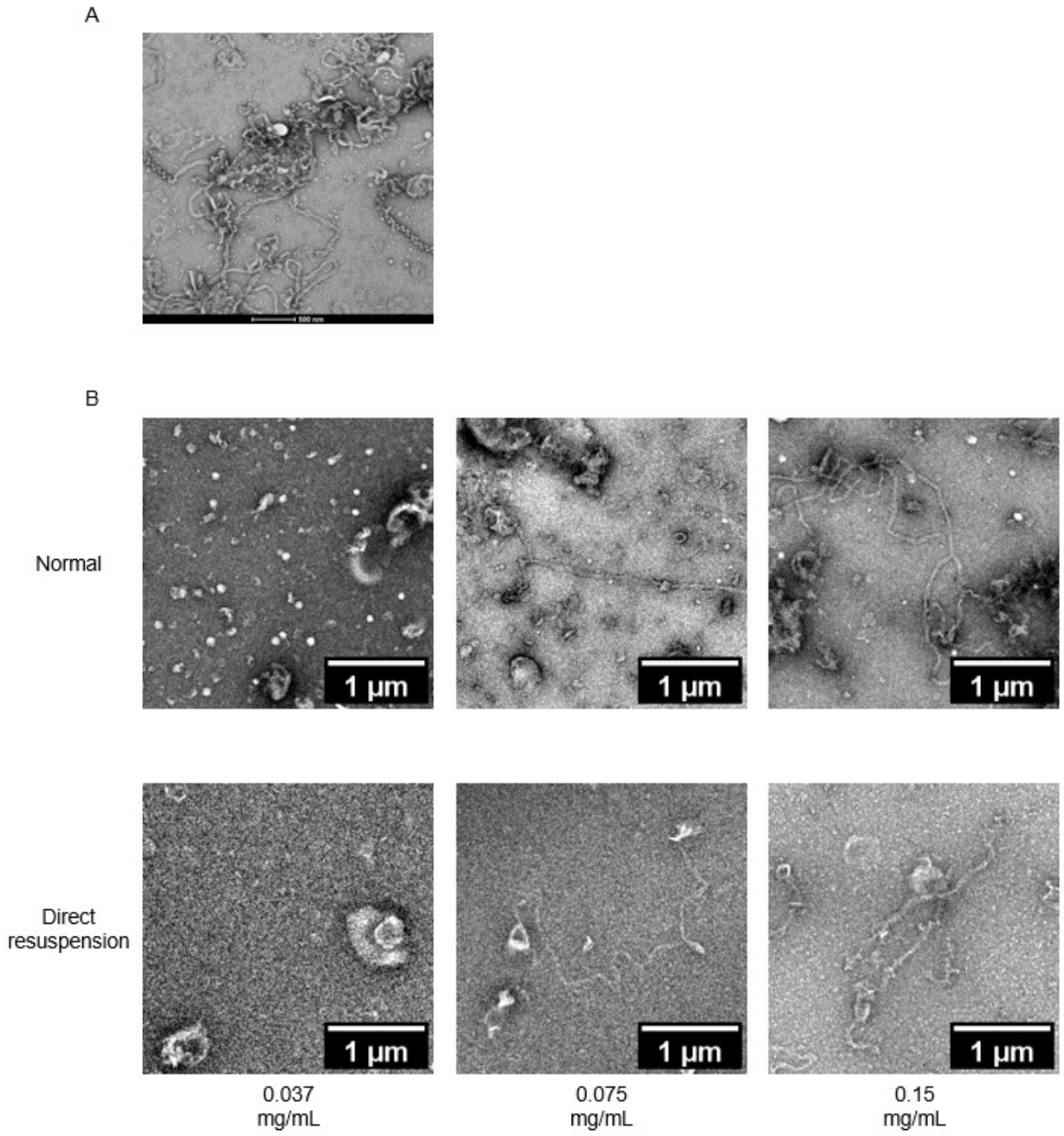

Figure 4.27: Comparison of direct resuspension and traditional tube preparation
(A) A negative stain micrograph showing the general morphology of the tubes prepared using the direct resuspension protocol. (B) For comparison of tube formation efficiency, the proteins were mixed and concentrated, and subsequently either a 10x mass excess of liposomes were added to the protein solution (top row), or the protein solution was used to directly resuspend a lipid film containing the same amount of lipids (i.e., a 10x mass excess, bottom row). The concentrations in the figure are the final concentration of protein in solution after lipid addition. The results are the same for both preparation methods, at the

lowest protein concentration no tubes are formed, however at higher concentrations both methods produce a similar number of tubes.

4.2.4 Cryo-EM structure determination of membranes remodeled by ESCRT-III proteins

For high resolution structure determination, the tubes were prepared using the direct resuspension protocol. Despite the apparent increase in the flexibility of the tubes, the direct resuspension protocol was used to produce the tubes, with the rationale that a sub-population of the tubes might contain an inner protein coat surrounded by an outer lipid bilayer. The sample was used to plunge-freeze Quantifoil R 1.2/1.3 grids. It was decided to initially use carbon-coated grids instead of AUfoil grids because of the propensity of the tubes to stick to the carbon. Due to their very long length, however, portions of each tube would be anchored to the carbon and the rest of the tube would extend into the ice (Figure 4.28A), a behavior also observed for p62 filaments. The tubes also showed variation along their width, even within the same tube (Figure 4.28A). This sample was used to collect a large dataset of ~30,000 movies with a total dose of 25 $e^-/Å^2$ in order to avoid radiation damage.

4.2.4.1 Large dataset pre-processing

After motion correction in WARP, the micrographs were imported into CryoSPARC for CTF estimation and automated particle picking using the filament tracer. The 2D classes from the previous dataset were used as a template. In order to avoid picking a single leaflet of each tube, as CryoSPARC was prone to do, the micrographs were low pass filtered to 200 Å. The resulting particle locations (7 x 10^6 segments) were extracted as overlapping segments (96%) with a box size of 980 Å and subjected to six rounds of 2D classification for cleanup. The remaining 2D classes (Figure 4.28B), consisting of ~600,000 particles were then separated based on tube width, as measured in PyHI [88]. The classes showed at least five different, discrete widths at 320 Å, 354 Å, 372 Å, 400 Å and 420 Å. The 2D classes also showed the protein coat exclusively on the outside of the tubes (Figure 4.28C).

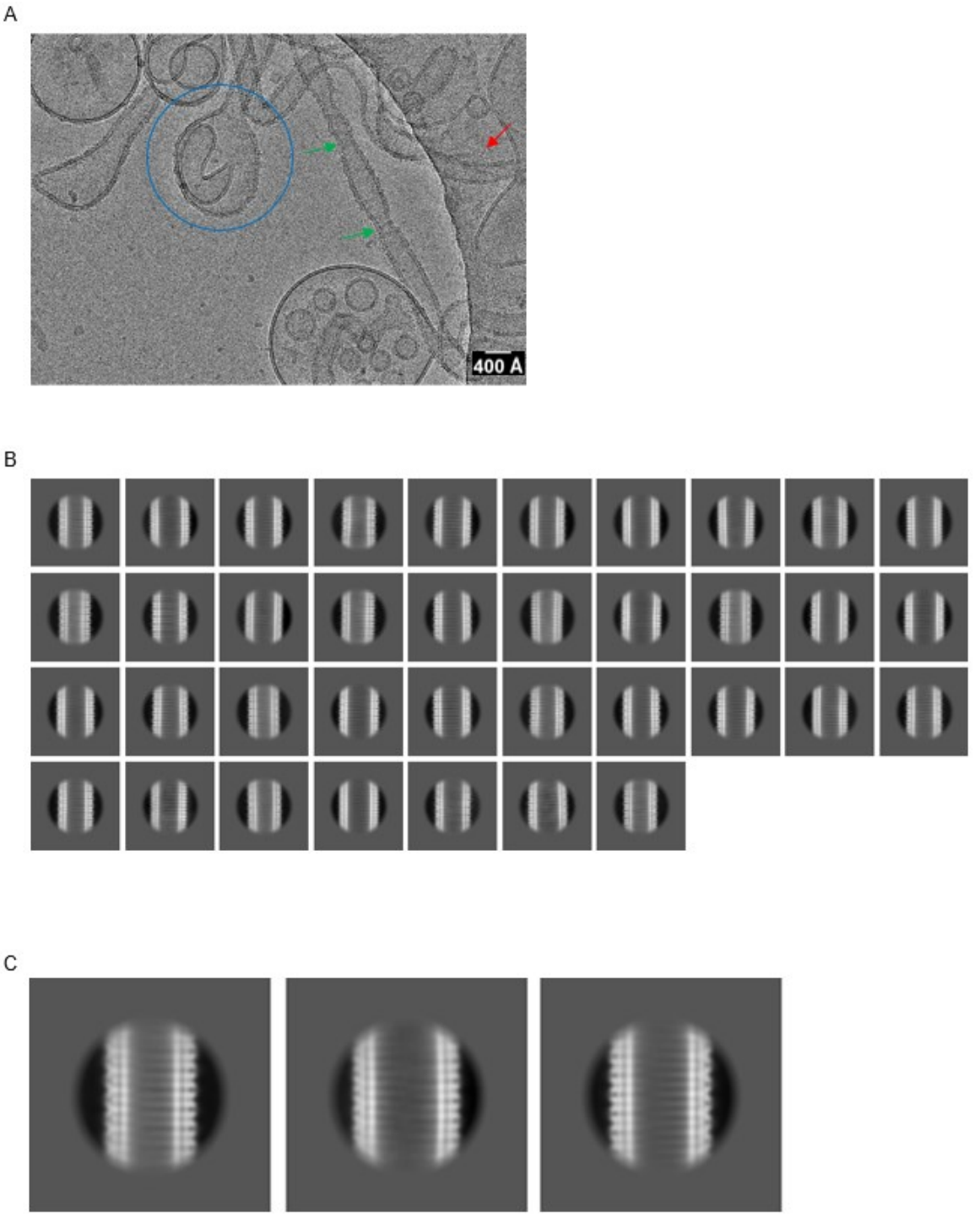

Figure 4.28: Direct resuspension protocol produces more numerous and longer tubes that show medium-resolution structural details

(A) The tubes under cryo-EM show similar morphology to the tubes prepared from liposomes, however their length allows them to remain anchored to the carbon support and extend into the ice (red arrow), thus increasing particle density. In addition, they show variation in width even along the same tube, as indicated by the green arrows. A single

liposome in the process of being remodeled by the protein coat is circled in blue. (B) The remaining 2D classes after six rounds of classification and cleanup. There are multiple tube widths present. All of the classes show the protein density on the outside of the lipid bilayer. (C) Zoomed in view of the first three classes showing the detail present on the tubes.

After separation based on width, the best classes corresponding to a 400 Å width (~31,000 segments, Figure 4.29A) were used for unsymmetrized reconstruction in CryoSPARC, using a featureless cylinder with a width of 400 Å as the starting model. This reconstruction (Figure 4.29B) had a final resolution of 15 Å at FSC=0.143.

4.2.4.1.1 Symmetry determination and first structure of ESCRT-III core complex proteins deforming a membrane

In order to determine the symmetry parameters, a single 2D class with a width of 400 Å was imported into SPRING [89] for use in *segclassreconstruct*. The resulting symmetry candidates suggested a wide range for the number of units per turn (Figure 4.29C). These symmetry parameters were then systematically used for reconstruction using the particle pool corresponding to 400 Å diameter tubes. Since the apparent pitch was around 80 Å, and manual counting of the subunits suggested around 36 units per turn, the actual search range was restricted to a pitch of 80 Å, and the number of units per turn restricted to 12-36. From these candidates, a single symmetry pair of 34 units per turn with a pitch of 80 Å led to a 9.2 Å map at FSC=0.143 (Figure 4.29D) with clear secondary structure features (Figure 4.29E). The map showed density for the helices α1, α2 and α3 portions of an ESCRT-III component as well as an anti-parallel, two stranded protein coat with D1 symmetry around a central lipid tube (Figure 4.29F). Due to the relatively low resolution of the map, and the fact that on a secondary structural level all three proteins are virtually identical, it could not be determined which specific protein or protein combination is wrapped around the tubes, however as an example, the computed structure of Vps24 [147] residues 1-138 is rigid body fitted into the map. Further analysis of this map and subsequent structures will be done in section 4.2.6.

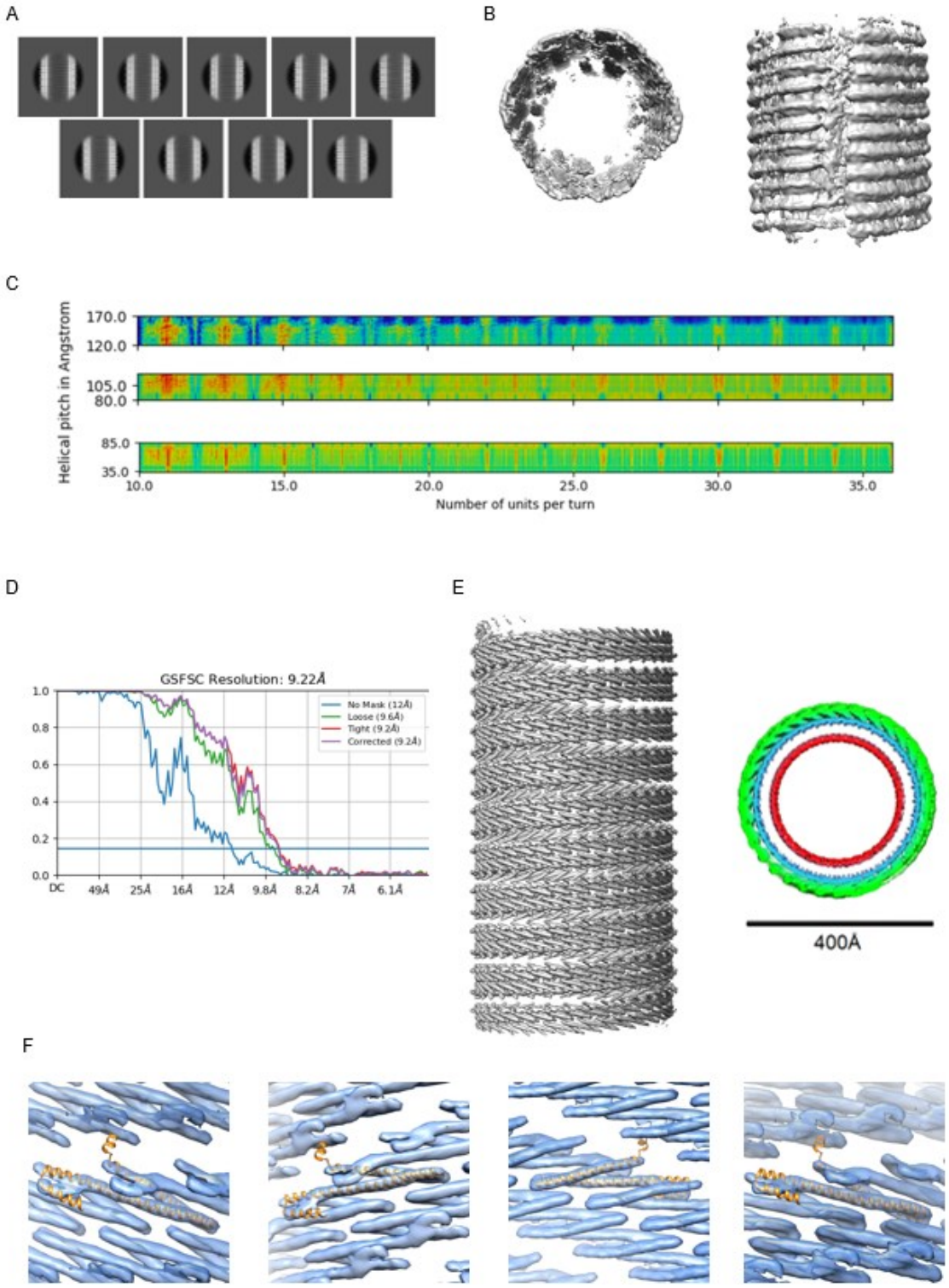

Figure 4.29: Symmetry and structure determination of ESCRT-III tubes
(A) The 2D classes that were selected based on width and used for initial model generation using a featureless cylinder, which led to the initial model in (B). (C) The results of the symmetry search performed using SPRING show a variety of symmetry candidates. (D) The first structure obtained using the symmetry candidate of 80 Å pitch and 34 units per turn

showed convincing secondary structure, at a global resolution of 9.22 Å. (E) The structure shows a large tube composed of a protein coat wrapped around a lipid bilayer. In the top view, the protein coat is colored in green, the outer lipid layer in blue and the inner lipid layer in red. (F) The rigid-body fit of Vps24 residues 1-138 into the map. There is no density present for helix α0, however helices α1, α2 and α3 fit well into the structure.

4.2.4.1.2 Additional symmetry arrangements structures

By extrapolation of the symmetry parameters for the 400 Å tubes, and assuming that a change in the number of units per turn as opposed to tighter packing of subunits was responsible for the smaller and larger diameters of the tubes, a set of symmetry candidates were estimated based on the circumference of various width tubes. The entire particle pool after junk removal (~600,000 segments) were then separated based on width into five clusters and then used for refinement without symmetry enforcement using a featureless cylinder of the appropriate width as the initial model. The resulting reconstructions were then used as the initial models for a further round of reconstruction with the appropriate symmetry candidates. The resulting reconstructions were then used for one round of 3D classification in order to further refine the particle assignments based on tube width. These particles were then used for a final round of symmetrized reconstruction, yielding five structures between 8 and 9 Å resolution. All of the structures showed the same two-stranded anti-parallel arrangement of subunits with clear secondary structure, differing only in width and the number of units per turn in the helix (Figure 4.30).

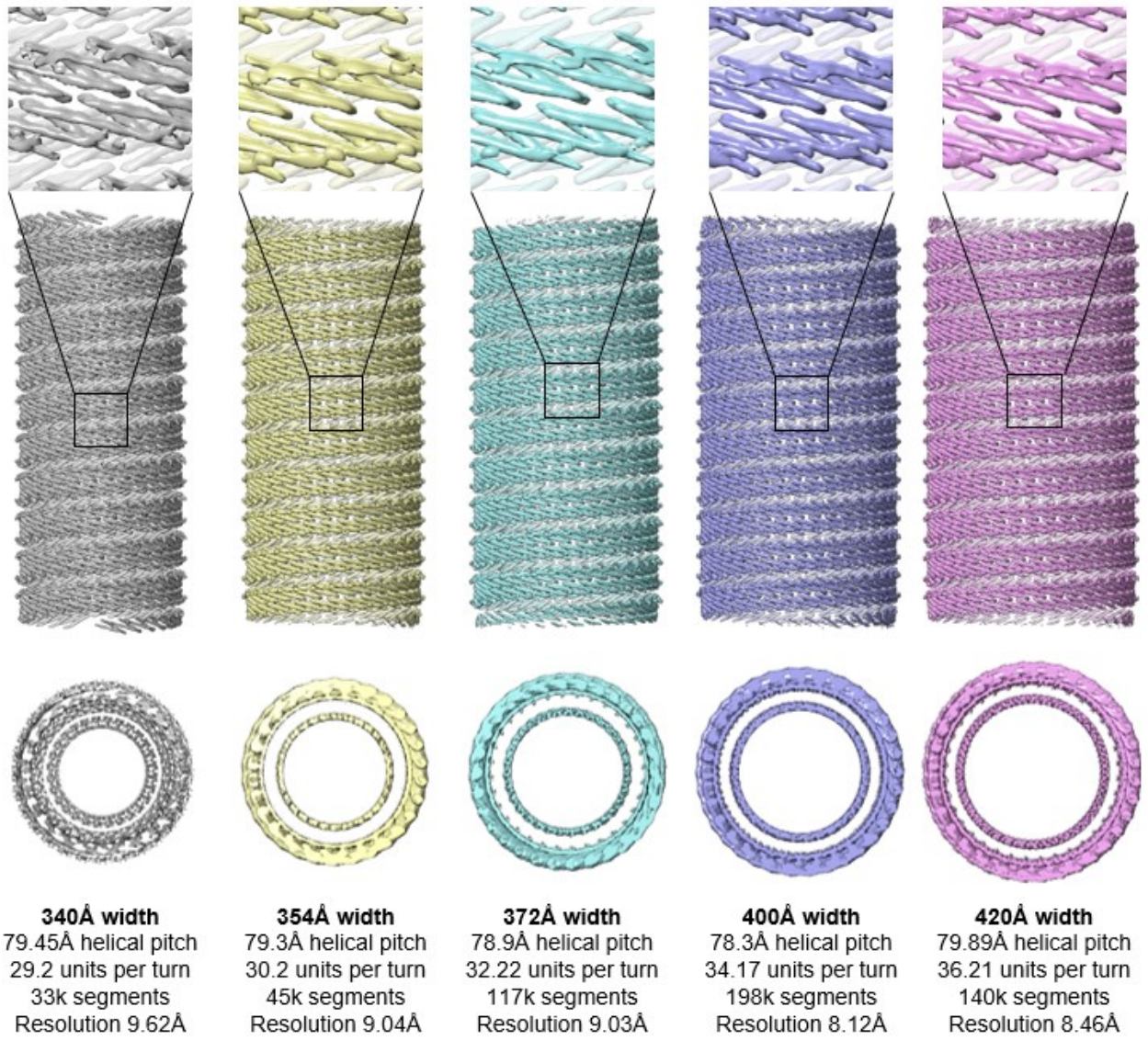

Figure 4.30: Side and top views of the ESCRT-III/YPL structures of tubes with various widths

(A) The resulting five reconstructions of tubes with different widths are shown above. The densities resolved between 8 and 9 Å resolution all show subunits with a hairpin-like secondary structure, arranged in a two-stranded anti-parallel architecture (top). The tubes are composed of a protein coat around a lipid bilayer that is visible at lower thresholds (bottom).

Since in helical reconstruction it is possible that a seemingly reasonable, but entirely incorrect map can be obtained if the symmetry parameters are incorrect, a further refinement using particles belonging to the tubes with 400 Å width was performed, but with the symmetry parameters corresponding to the reconstruction with a tube width of 372 Å.

The resulting map, while nominally at 8.96 Å resolution, did not show clear secondary structure features, and overall did not look like a protein density map (Figure 4.31). This strongly suggests that the symmetry parameters used for the other reconstructions are correct, despite the lack of visible side chain density.

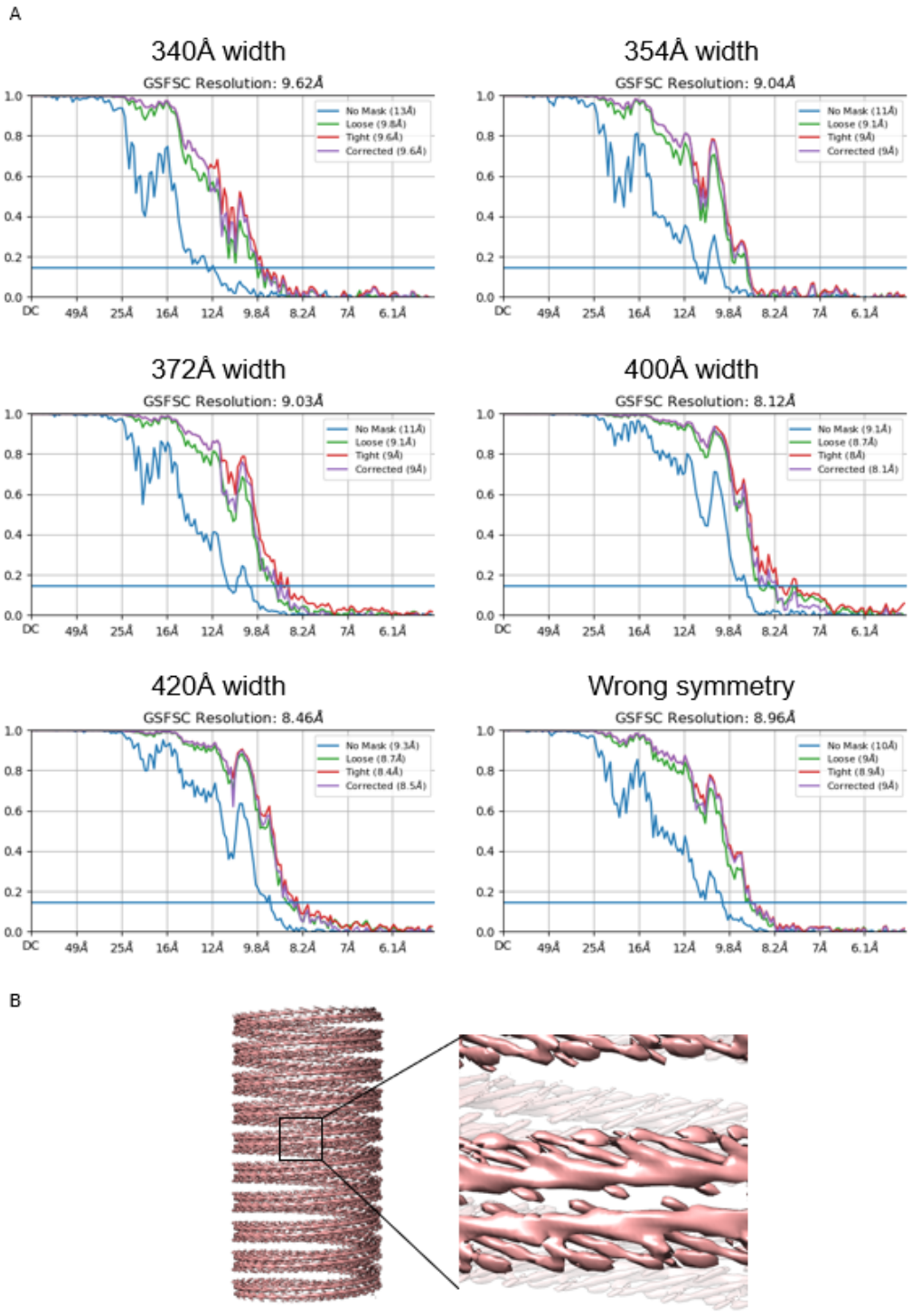

Figure 4.31: FSC curves of the structures obtained and intentionally incorrect reconstruction

(A) The FSC curves outputted by CryoSPARC after refinement of structures are shown. In addition, the FSC curve of the intentionally incorrect structure is shown. (B) The intentionally incorrect structure does not have secondary structure elements and does not look like a proper protein density map.

4.2.5 Roles of individual ESCRT-III subunits in YPL interaction

In order to further characterize the interaction between the ESCRT-III subunits and yeast polar lipids and elucidate the role of each protein in membrane remodeling, individual proteins either alone or in various combinations were mixed with either YPL liposomes or used in the direct resuspension protocol for tube formation. The first experiment was to examine whether Vps2ΔNC/Vps24 without Snf7 present could remodel liposomes into tubes. Vps2ΔNC/Vps24 or Vps2ΔNC/Vps24/Snf7 were mixed and concentrated to 0.3 mg/mL per protein and mixed with YPL liposomes. Separately, the proteins were mixed and concentrated to 0.15 mg/mL per protein and used to directly resuspend a YPL lipid film. It is important to note that in this experiment, the relative amount of lipid to protein is not the same for the two preparation protocols, since the direct-resuspension method uses ~4.5x more lipids. After incubation for two hours at room temperature, the samples were visualized by negative staining. The results showed only liposomes in the first sample as expected, since in previous experiments Snf7 was required for tube formation using this protocol. However, the direct-resuspension sample showed the presence of tubes with similar morphology to the tubes formed by the triple complex of Vps2ΔNC/Vps24/Snf7 of Vps2ΔNC/Vps24/Snf7 (Figure 4.32).

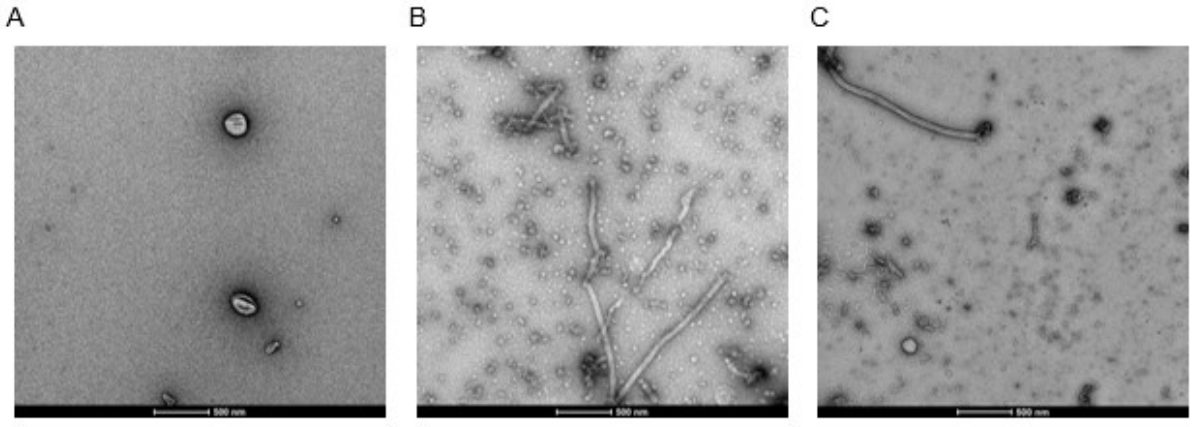

Figure 4.32: Vps2ΔNC and Vps24 are sufficient for membrane remodeling
Vps2ΔNC and Vps24 alone, without Snf7 can also produce tubes when used in the direct-resuspension protocol (panel B), which contains 4.5x as much lipids to protein ratio. In contrast, Vps2ΔNC/Vps24 alone will not form tubes with the liposome-addition protocol (panel A), however once Snf7 is included, tubes will form (panel C). This result strongly suggests that Snf7, while not required, plays a facilitatory role in tube formation and can perhaps reduce the activation energy needed for the remodeling of the lipid membranes.

As this result was unexpected, a series of experiments were performed where each ESCRT-III protein alone or in a binary combination was concentrated to 0.15 mg/mL per protein and used for direct resuspension of a YPL film. The results showed that neither protein alone, nor any combination other than Vps2ΔNC/Vps24 were sufficient to produce tubes (Figure 4.33). Taken together, these results suggest that while Snf7 is not required for membrane remodeling at high lipid concentrations, at low lipid concentrations it seems to play a role as facilitator of remodeling, perhaps by acting as an anchoring point for the polymerization of Vps2ΔNC/Vps24.

Furthermore, there is a lack of any density corresponding to helix α0 in any of the maps. This region of the proteins is thought to be essential for homopolymerization of Vps24 [143] and is thought to function as a membrane anchor in the case of Snf7 [144]. Thus, another question was whether Vps2/Vps24 that both lacked this N-terminal helix could participate in membrane remodeling. To answer this question, Vps2ΔNC and Vps24 protein lacking the first 9 residues were mixed and concentrated to 0.15mg/mL per protein and used to resuspend a YPL film. The results showed that the proteins were still capable of membrane remodeling (Figure 4.33), showing that the α0 portion of neither protein is strictly required for lipid binding or membrane remodeling.

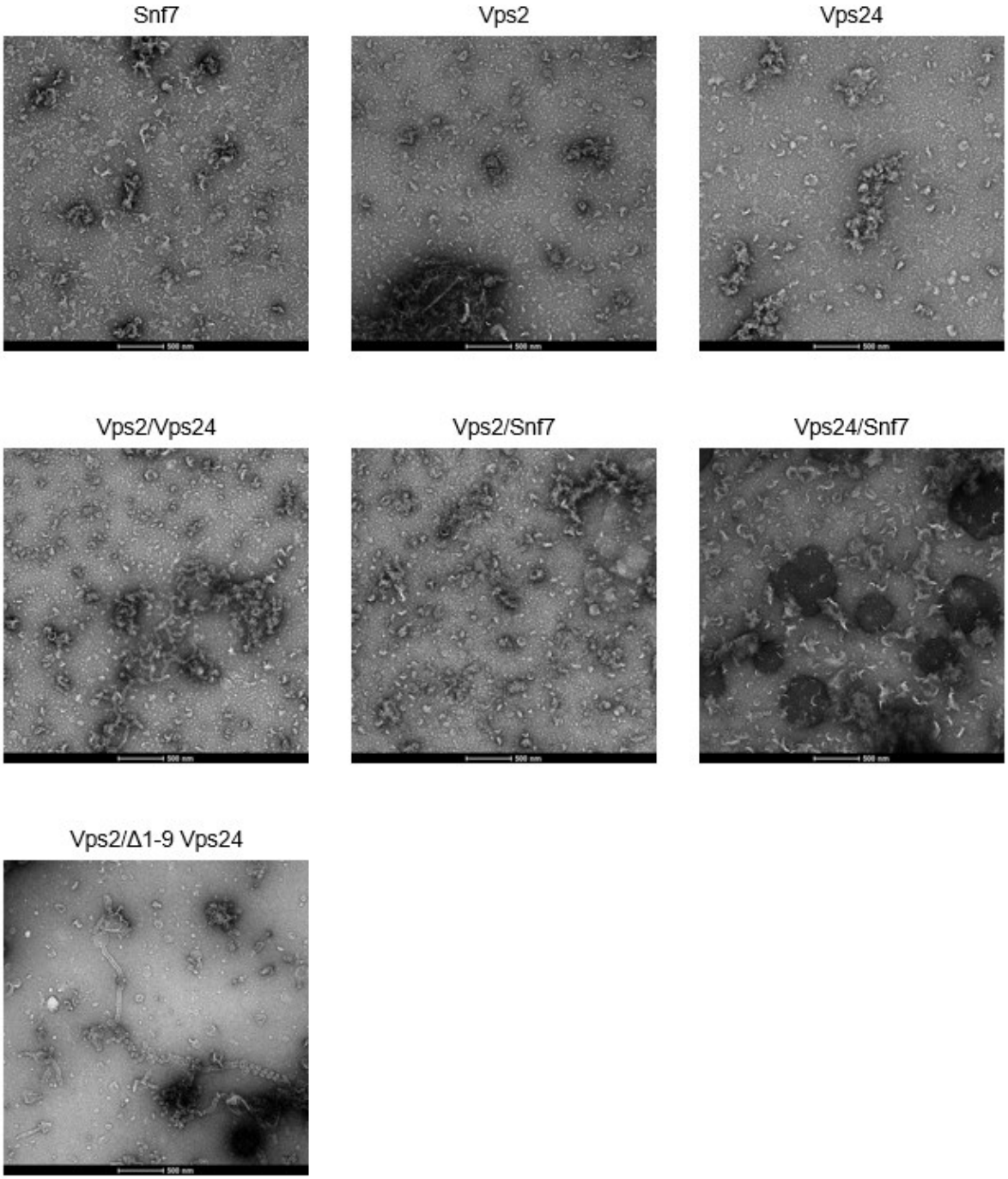

Figure 4.33: Vps2ΔNC and Vps24 are strictly required for membrane remodeling, and the N-terminal 9 residues are not critical for this function
After resuspension of a YPL extract lipid film in protein solutions containing various combinations of the yeast ESCRT-III proteins, none of the proteins either alone or in a binary mixture, except for Vps2ΔNC/Vps24 are capable of tube formation as shown by negative-staining EM. In addition, Vps2ΔNC/Δ1-9 Vps24 can also form tubes, indicating that the N-terminal helix α0 is not required for tube formation.

4.2.5.1 Membrane remodeling by Vps2ΔNC/Vps24

In order to produce a cryo-EM sample consisting of tubes formed by YPL and Vps2ΔNC/Vps24, the proteins were mixed and concentrated to 0.15 mg/mL per protein and used to resuspend a YPL film. The sample was then incubated for two hours at room temperature and plunge frozen on Quantifoil R1.2/1.3 grids. After screening by cryo-EM, a dataset consisting of ~5800 movies was collected on a Talos Arctica 200 keV microscope using EPU and a defocus range of -0.5 to -3 µm. The movies were motion corrected in WARP and imported into CryoSPARC for CTF estimation. Particles were picked using the CryoSPARC filament tracer, and ~850,000 segments were extracted with a box size of 980 Å with a 96% overlap. Following three rounds of 2D classification to remove junk, the remaining ~86,000 particles were separated based on the apparent width of the 2D class averages. Three distinct widths were observed, 400 Å, 372 Å and 340 Å, however the number of segments for the 340 Å wide tubes (7400 segments) was far too low for 3D refinement. The particles from the other two tube widths were first used for refinement without symmetry using a featureless cylinder as an initial model. The resulting map was then used for symmetrized refinement using the corresponding symmetry parameters determined from the triple complex of Vps2ΔNC/Vps24/Snf7 dataset and these maps were used for 3D classification of the particles. The resulting particles were then used for another round of refinement. The resulting maps, as well the final refined symmetries, were virtually identical to the triple complex of Vps2ΔNC/Vps24/Snf7 maps and refined symmetries (Figure 4.34).

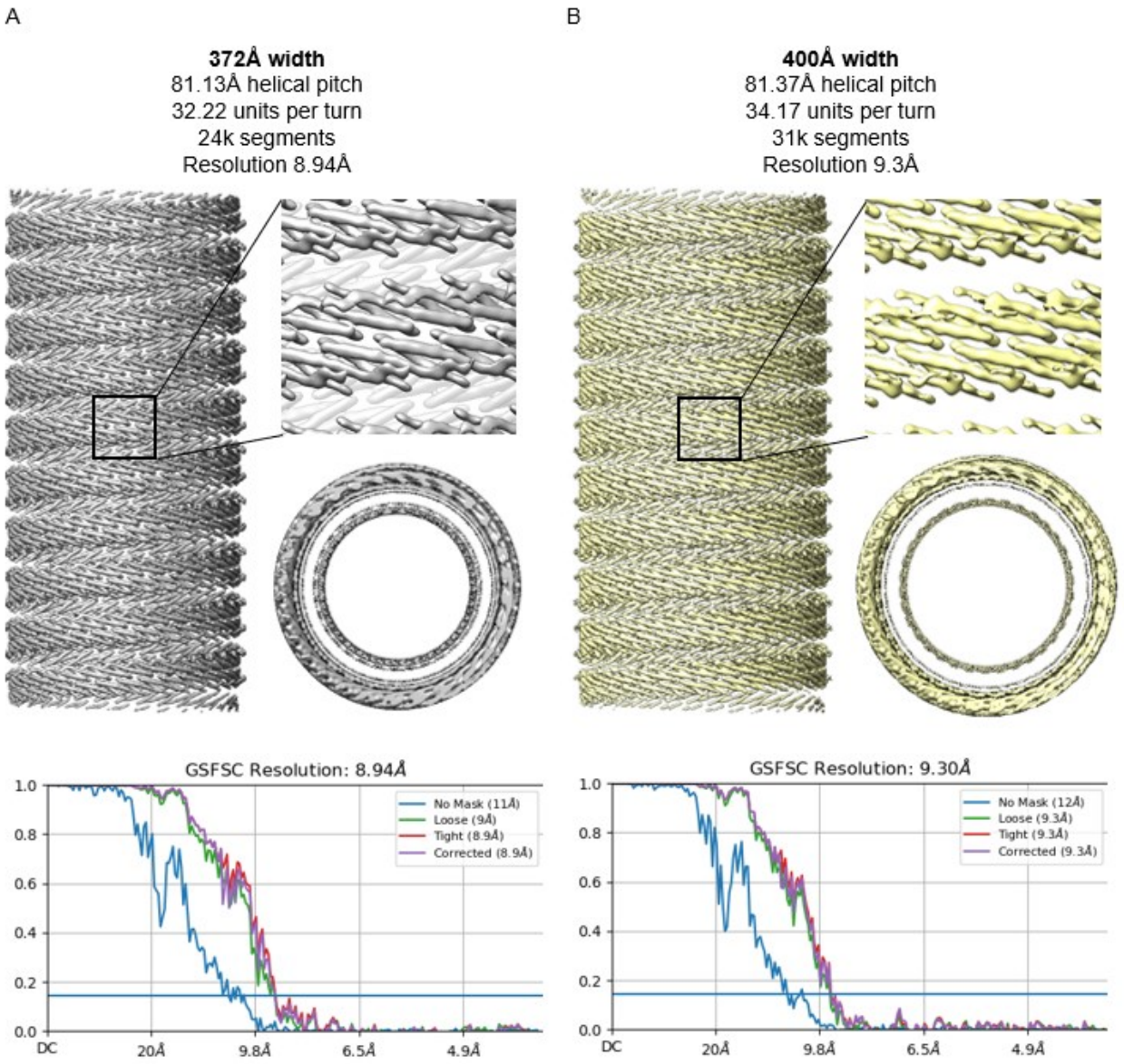

Figure 4.34: Structures of tubes formed by Vps2ΔNC/Vps24
Two structures could be determined to medium resolution from this dataset, one with a width of 372 Å (A) and one with a width of 400 Å (B). The side, top and zoomed in views are shown for each structure as well as the FSC curves. The structures are almost identical aside from a difference in the number of units per turn.

4.2.6 Analysis and comparison of ESCRT-III structures determined in this thesis

While all of the structures obtained are similar, there are some differences in how the subunits are arranged with respect to each other in order to accommodate the differences in

symmetry. In addition, there is still uncertainty about which of the three proteins alone or in combination constitutes the protein coat. The liposome flotation assays show a larger relative amount of Vps24 compared to Vps2ΔNC in the top fraction (Figure 4.10B). Given the fact that the resolution of the structures did not fall below 8 Å and given the high degree of heterogeneity in the local width of each individual tube, it is possible that more than one protein constitutes the protein coat. In such a scenario, the averaging algorithms used in cryo-EM reconstructions would only be able to resolve features common to all of the proteins present in the protein coat, and at below 8 Å resolution it should be expected that the structures of the three (or two) proteins will diverge. Nevertheless, the overall architecture of the tubes can provide insights into how the proteins may interact with the lipid bilayer and deform them into tubes.

As a start, the structures of all three proteins consisting of helices α1, α2, α3 and portions of helix α4 can be rigid-body fitted into the 400 Å wide tubes consisting of Vps2ΔNC/Vps24/Snf7, this is shown below, where Vps2 10-166, Vps24 10-138 (both truncated from the Vps2/Vps24 model published by Humphreys, et al. 2021 [147], and Snf7 18-124 (truncated from PDB: 5FD7 [146]) are fitted into the map (Figure 4.35). The resulting structures show that with Vps2 and Vps24, there are many positively charged residues pointing directly at the outer lipid layer (Figure 4.36A). In the case of Snf7, while there are some positively charged residues that point towards the membrane, there are also many negatively charged residues pointing at the membrane (Figure 4.35). This observation suggests that Snf7 may not be a part of the protein coat, or, that if it is indeed present in the protein coat, it is only marginally involved in lipid binding.

The largest difference between the structures is the difference in the number of units per turn. This difference will cause small variation in how the protein or proteins interact with each other. While it is likely that the same residues are involved in every interaction, at 8-9 Å resolution it is not possible to identify individual residues. At the most extreme ends are the structures with 340 Å tube width (29.2 units per turn) and 420 Å tube width (36.2 units per turn) in which the distance between the Cα of the N-terminal residues increases only by about 2.4 Å, while the C-terminal end of helix α3 moves by about 4.2 Å (Figure 4.36B). Alignment of two monomers of the intermediate structures shows a gradual movement outwards from the axis of the tube as the tube width increases (Figure 4.36C). In addition,

as shown in the radial intensity profiles (Figures 4.37 and 4.38) the structures show a gradual constriction of the membrane, with the distance between the inner leaflets reducing from 292 Å to 192 Å when the tube width changes from 420 Å to 340 Å (Figure 4.39). In addition, despite the slightly different symmetry parameters and more noisy radial intensity profiles, there is no difference between the individual subunit densities of the tubes with 372 Å width when prepared from Vps2ΔNC/Vps24 and Vps2ΔNC/Vps24/Snf7 (Figure 4.40A). However, in the maps of the tubes with 400 Å width, possibly due to the noisier Vps2ΔNC/Vps24 map, there are some differences, especially in the region corresponding to helix α4. At these resolutions, it is not possible to definitively say that these differences are real or an artifact of map sharpening.

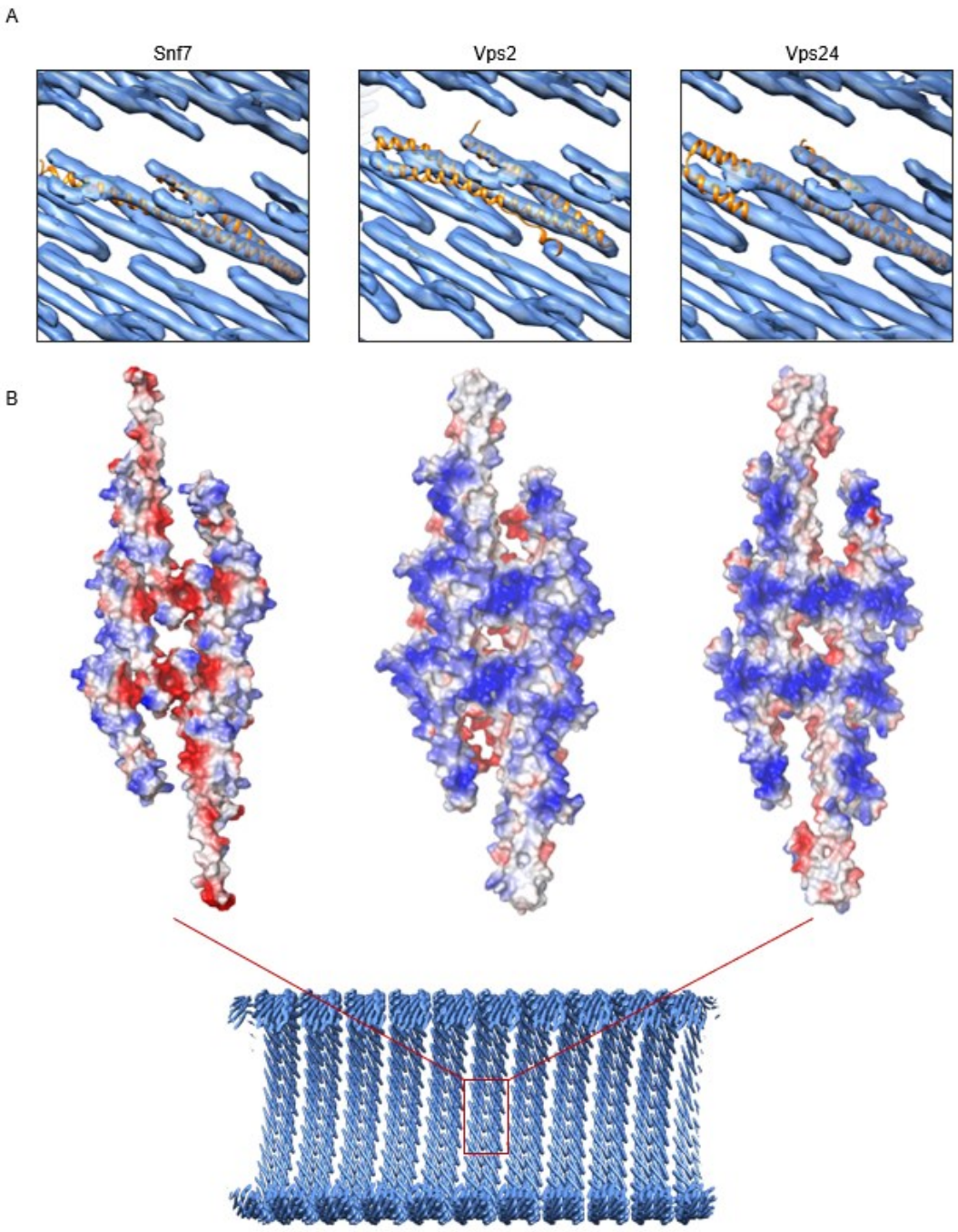

Figure 4.35: Rigid-body fitting of ESCRT-III subunits into the maps
(A) The three ESCRT-III subunits can all be rigid-body fitted into the map which shows density for helices α1, α2 and α3. (B) Six monomers of each protein were fit into the map and displayed as a surface colored by electrostatic potential as calculated in Pymol. In this view, the membrane is on the front of the screen. Both Vps2 and Vps24 have a substantially positive surface that points towards the membrane, however the Snf7 surface pointing towards the membrane has a few positively charged patches interspaced with large negatively charged or neutral patches.

A

Snf7	Vps24	Vps2
R7	R18	K19
R41	R21	R23
R52	R25	R30
	R29	R34
	R36	R37
	K50	K44
	K51	K51
	K54	K55
	R89	R97
	R97	

B

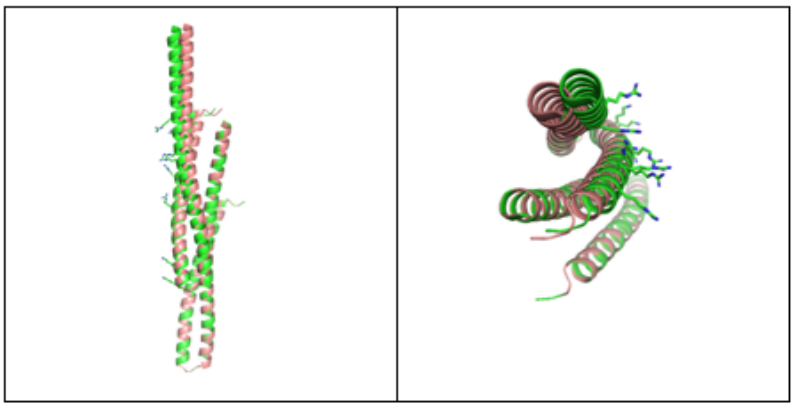

C

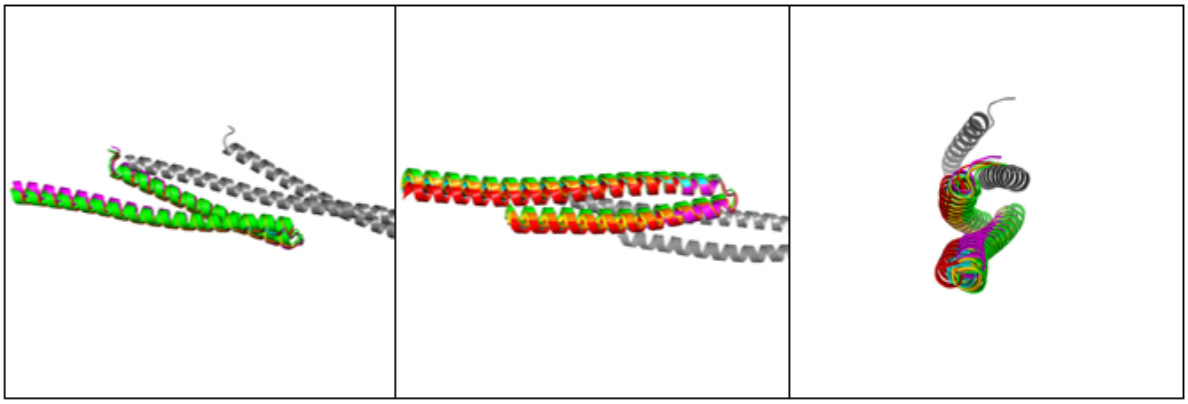

Figure 4.36: Positively charged residues on Vps2 and Vps24 are positioned to contact the lipid membrane

(A) This table shows the positively charged residues on all three proteins that are pointing towards the membrane and have Cαs that are less than 10 Å away from the lipid membrane. Snf7 does not have many contacts, while Vps2 and Vps24 make extensive contact with the lipid membrane. (B) Alignment of two subunits in the helical scaffold from the structures with 340 Å (green) and 420 Å (pink) tube width shows small differences in how the monomers are packed together, despite the large difference in tube diameter. The structure shown is that of Vps24 helix α1, α2 and α3 (residues 10-118). The side chains of the residues hypothesized to contact the lipid membrane are shown. In the left figure in this panel, the membrane is located in the front of the screen, and in the right panel the membrane is located to the right of the structure. (C) The alignment from all structures, with the fixed monomer of Vps24 in grey. The alignment shows the gradual rotation of the monomers are tube width increases. The structures are colored as follows: triple complex, 340 Å wide tubes in red, triple complex 354 Å wide tubes in green, triple complex 372 Å wide tubes in blue, triple complex 400 Å wide tubes in yellow, triple complex 420 Å wide tubes in magenta, Vps2ΔNC/Vps24 372 Å wide tubes in cyan, Vps2ΔNC/Vps24 400 Å wide tubes in orange. In the left panel, the membrane is located on the bottom of the structure, while in the center panel the membrane is located in front of the screen, and on the right panel the membrane is located to the right of the structure.

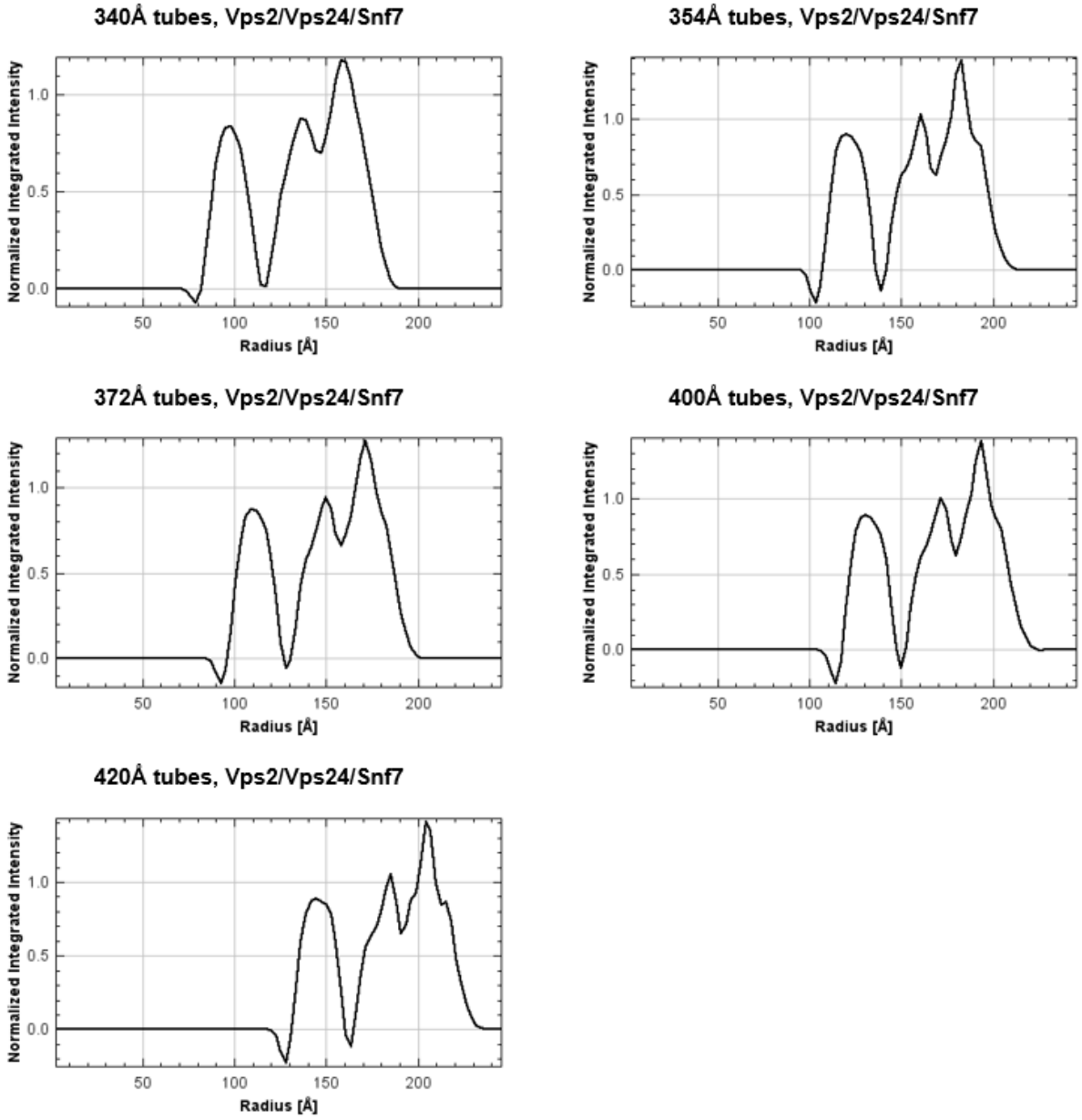

Figure 4.37: Radial intensity profiles of Vps2ΔNC/Vps24/Snf7 tubes
The radial intensity profiles of the Vps2ΔNC/Vps24/Snf7 structures determined in this work is shown. The intensity profile is calculated based on a Z-axis projection of the central 30% of the final maps and shows three distinct intensity peaks corresponding to the inner membrane leaflet, outer membrane leaflet and the protein coat. See Figure 4.39 for more information.

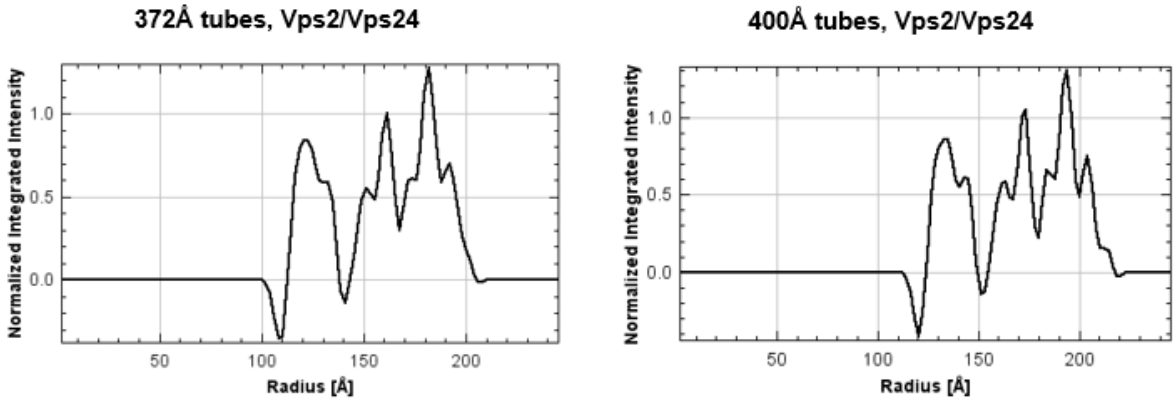

Figure 4.38: Radial intensity profiles of Vps2ΔNC/Vps24 tubes
The radial intensity profiles of the Vps2ΔNC/Vps24 structures determined in this work is shown. The intensity profile is calculated based on a Z-axis projection of the central 30% of the final maps and shows three distinct intensity peaks corresponding to the inner membrane leaflet, outer membrane leaflet and the protein coat. See Figure 4.39 for more information.

A

Protein coat	Tube radius	Bilayer width (Å)	Inner leaflet width (Å)
Vps2/Vps24/Snf7			
	340Å	41	192
	354Å	40	218
	372Å	41	240
	400Å	42	260
	420Å	39	292
Vps2/Vps24			
	372Å	39	244
	400Å	39	268

B

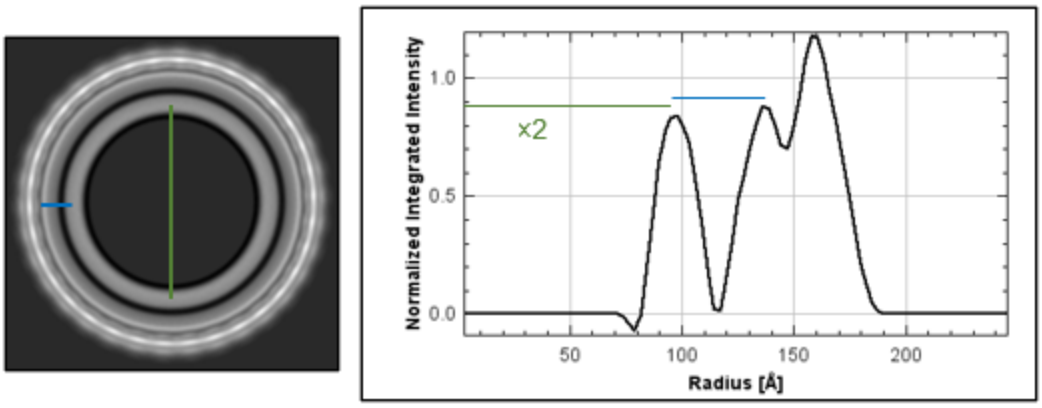

Figure 4.39: Radial intensity profiles show constriction of membrane tube
(A) Tabulated measurements of the lipid bilayer width from the various structures, as well as the inner leaflet width. The results clearly show a gradual constriction of the membrane surrounded by the protein coat, while the bilayer width does not change. (B) The bilayer width was calculated as the distance between the highest intensity regions of each lipid leaflet from the radial intensity profiles (blue lines) while the inner leaflet width was measured as the distance between the highest intensity region of the inner lipid leaflet from opposite sides of the tube (green lines).

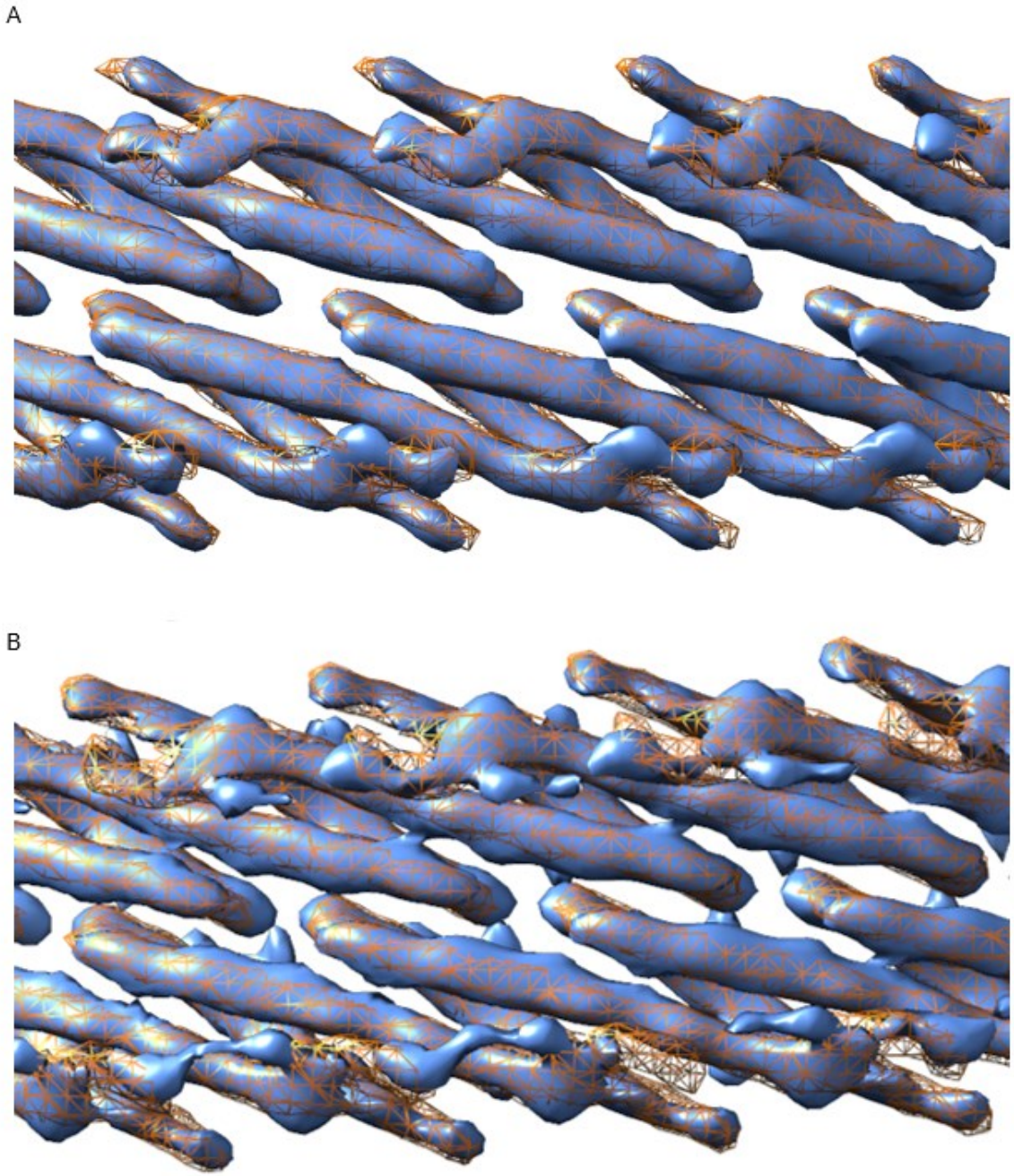

Figure 4.40: Comparison of the Vps2ΔNC/Vps24 map with the corresponding Vps2ΔNC/Vps24/Snf7 maps of the same width
(A) shows the Vps2ΔNC/Vps24/Snf7 map with 372 Å width as an orange mesh overlayed on the Vps2ΔNC/Vps24 map with 372 Å width as a blue surface. The two maps can be nearly perfectly superimposed and do not show any notable differences. (B) The overlay of the Vps2ΔNC/Vps24/Snf7 map of the tubes with 400 Å width as an orange mesh and the Vps2ΔNC/Vps24 map of the same width as a blue surface. This overlay shows that while the regions corresponding to helices α1, α2 and α3 can be perfectly superimposed, there are still minor differences in the region corresponding to helix α4.

4.3 Discussion

4.3.1 Membranes are remodeled and constricted by the helical co-polymer assembly of yeast ESCRT-III proteins

The yeast ESCRT-III subunits Vps2 and Vps24 have been shown to be sufficient for the remodeling of LUVs, liposomes, and even lipid films into tubular structures. The structures show clear density for helices α1, α2 and α3, and additional density that possibly corresponds to helix α4. Depending on the composition of the lipid, the width of these tubular structures can range from less than 300 Å to over 600 Å. The two proteins form a helical co-polymer coat around the lipid bilayer and gradually constrict the membrane bilayer by a mechanism involving the reduction in the number of units per turn in the helical lattice. The structures determined in this work show that even though the number of units per turn in the helical lattice can range between 29 and 36 units, the relative packing of the monomers in the helical lattice is remarkably consistent. In addition, the proteins are shown to bind to the membrane using a large positively charged patch mostly composed of residues on helix α1.

4.3.2 Identity of the proteins in the helical coat and the role of Snf7

Due to the limited resolution of the structures, and the high level of similarity between the secondary structure composition of Vps2 and Vps24, it is not possible to determine which of the two proteins forms the protein coat. Nevertheless, the fact that all of the structures converge to ~9 Å resolution regardless of the number of particles suggests that the protein coat may be composed of a complex and possibly non-uniform arrangement of both proteins. Previous results from the flotation assays suggest that Vps24 is present in higher amounts in top fraction, which contained the remodeled tubes, compared to Vps2 (See figure 4.10, panel B). This suggests that even though the protein mixture added to the lipids had a 1:1 molar ratio stoichiometry, Vps2 and Vps24 may not necessarily be in a 1:1 ratio once bound to the remodeled membranes. The architecture of the helical assembly is consistent with how Vps2 and Vps24 are thought to interact, as shown by the fact that the computed Vps2/Vps24 dimer [147] can be rigidly fitted into the maps (Figure 4.41). The tubes also show substantial flexibility, both in a global scale as demonstrated by the high curvature

of the tubes, as well as local scale, as demonstrated by the frequent change in the width along each tube (Figure 4.28A). This could be a consequence of locally higher or lower density of Vps2 or Vps24.

While Snf7 is not required for this remodeling activity, it seems to play the role of a facilitator of the remodeling activity, perhaps by acting as a membrane anchoring point around which Vps2 and Vps24 can begin assembly. This is evident from the fact that at low lipid to protein ratios, Snf7 is required for tube formation, while at higher lipid to protein ratios, it is dispensable.

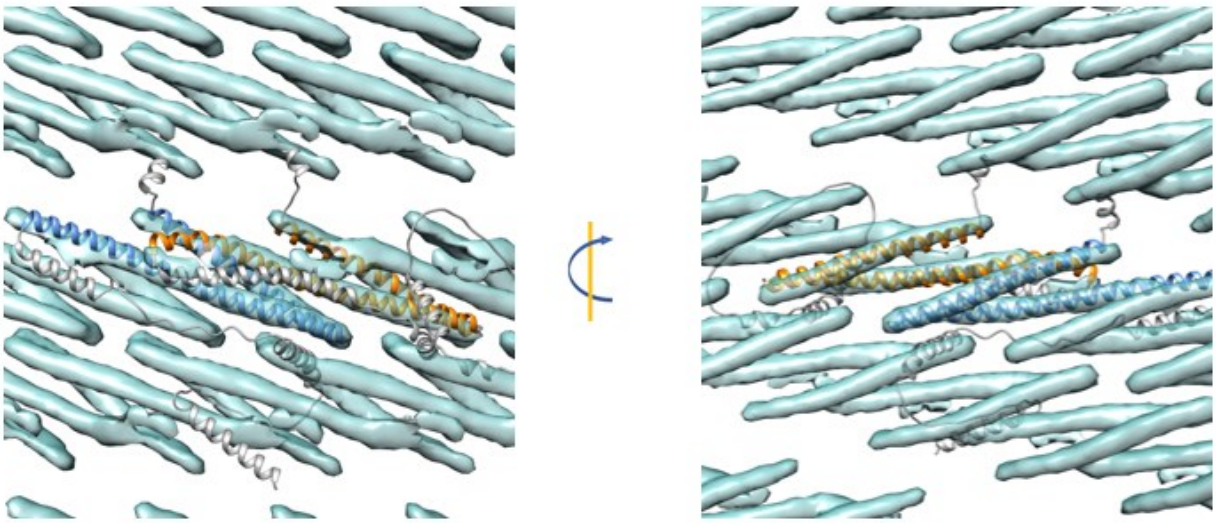

Figure 4.41: Rigid body fitting of Vps2/Vps24 dimer
The computed dimer of Vps2 and Vps24 can be fit easily into the maps. This particular figure shows the structure determined from tubes remodeled by Vps2ΔNC/Vps24/Snf7 with a width of 400 Å. The regions corresponding to helices α1-α3 are colored in orange for Vps2 and blue for Vps24, while the rest of the protein is colored in grey.

4.3.3 Binding dynamics of Vps24/Vps2 to lipids

The α0 helix of Snf7 is thought to function as an anchor to the membrane surface [144], and the N-terminal helix α0 of Vps24 is involved in the formation of homo-polymeric filaments [49], however the LUV flotation assay carried out in this work shows that the α0 helix of Vps24 and Vps2ΔNC are not required for lipid interaction. In addition, Vps2 and Vps24 that are α0 helix truncated are still able to deform YPL liposomes into tubes. Furthermore, the Vps24 helix α4 charge reversal mutant (K133D/E134A/K137D) studied in

this work retains its lipid interaction ability, and the structures solved show that a large, positively charged patch on the α1 and α2 helices of either Vps2, Vps24 or both, is in contact with the membrane surface. Taken together, these results suggest that the interaction between Vps2/Vps24 and lipids occurs mainly through the charged patches present on helices α1 and α2.

While the Vps2ΔNC/Vps24/Snf7 complex is capable of remodeling liposomes prepared from DOPS, Yeast Polar Lipids extract (YPL) and Yeast Total Lipids extract (YTL), the morphology of these tubes varies significantly (Figure 4.23). Whereas the YTL tubes appear as thinner, more irregular structures under negative stain, the DOPS and YPL tubes appear more similar, and the main difference between them is the variability in width. These differences in remodeling behavior can be explained by three factors: membrane fluidity due to the presence of uncharged lipids, lipids with different tail lengths, unsaturated lipids, and cholesterol in YPL and YTL compared to DOPS; the presence of Phosphatidylinositol (that may be phosphorylated to PI3P) in YPL and YTL; and preferential binding of Vps2ΔNC/Vps24 to different negatively charged lipids. In the case of DOPS and YPL, there seems to be little difference between tubes prepared at 4 °C and 23 °C (Figure 4.23). Since temperature can substantially modulate membrane fluidity, this seems to suggest that the differences between the tubes made from DOPS and YPL are driven by a different factor, most likely preferential binding to different lipid head groups by Vps2ΔNC/Vps24. Furthermore, since human Vps24 is known to specifically bind to PI3P [126], PI3P binding is a good candidate for the mechanism that may cause the differences between DOPS and YPL tubes.

4.3.4 Comparison to other ESCRT-III and ESCRT-III-like helical assemblies

There are several comparable structures from different organisms that show a protein coat remodeling membranes (Figure 4.42). The human ESCRT-III homolog CHMP1B is also capable of binding to and remodeling membranes into tubular structures with diameters of 26-30nm [125] in a very similar fashion as the ESCRT-III proteins discussed in this thesis. In addition, upon binding to the human ESCRT-III homolog IST1, the CHMP1B/IST1 complex is capable of restricting the membrane tubes into diameters of 24-

25nm [125]. Interestingly, the ESCRT-III-like protein PspA from the cyanobacterium *Synechocystis* sp. PCC 6803, which is involved in membrane repair, was recently shown to also be capable of remodeling membranes into tubular shapes [158] with diameters of 27.5nm. In both cases, the individual protein subunits adopt a canonical ESCRT-III fold, with helix α1 involved in lipid binding. In the case of PspA, there is additional density present for helix α0 that seems to be protruding into the membrane [158]. This particular feature is absent from the yeast ESCRT-III structures presented in this thesis and also from the CHMP1B and CHMP1B/IST1 structures as CHMP1B does not possess a helix α0. One additional difference is the presence of D1 symmetry in the yeast ESCRT-III structures, which is lacking in the CHMP1B, CHMP1B/IST1 and PspA structures. Nevertheless, the presence of similar membrane tubes remodeled by proteins with low primary structure homology, but high structural homology demonstrates an evolutionarily conserved mechanism for membrane remodeling processes throughout very diverse species.

4.4 Outlook

Due to the medium resolution of the structures solved, as well as the uncertainty surrounding the identity of the proteins present in the coat, the first path forward will be to determine a structure at below 4 Å resolution, which would allow the identification of side chain residues. An alternative approach to identifying the components of the protein coat is the preparation of the tubes using C-terminally tagged Vps2, Vps24 and Snf7, which can then be probed by anti-hexahistidine fiducial markers under cryo-EM. Such an approach may be able to identify the localization of every protein and may provide clues regarding the function of each protein. Other approaches may include mutagenesis of the ESCRT-III core proteins, as well as using truncated forms of the proteins, or using the full-length form of Vps2.

While the results strongly suggest that the mechanism of membrane constriction involves removal of protein subunits from the helical lattice, the driving force behind this mechanism is not known. More detailed studies of the interaction of Vps4 with the ESCRT-III subunits may shed some light on this. In addition, other ESCRT-III proteins such as IST1 and Vps20 may be included in the protein/lipid mixture to study their effects.

The structures solved in this work all show an outer protein scaffold wrapped around an inner lipid membrane. Within the context of autophagy, MVB genesis and especially cytokinesis, it may make more sense for the protein to form an inner scaffold with an outer membrane coat formed around it. It is currently unknown whether Vps2/Vps24/Snf7 require another binding partner in order to form such a scaffold, or whether another set of proteins entirely is responsible for this architecture. FIB-milled cellular slices studied by Cryo-electron tomography may shed some light on this.

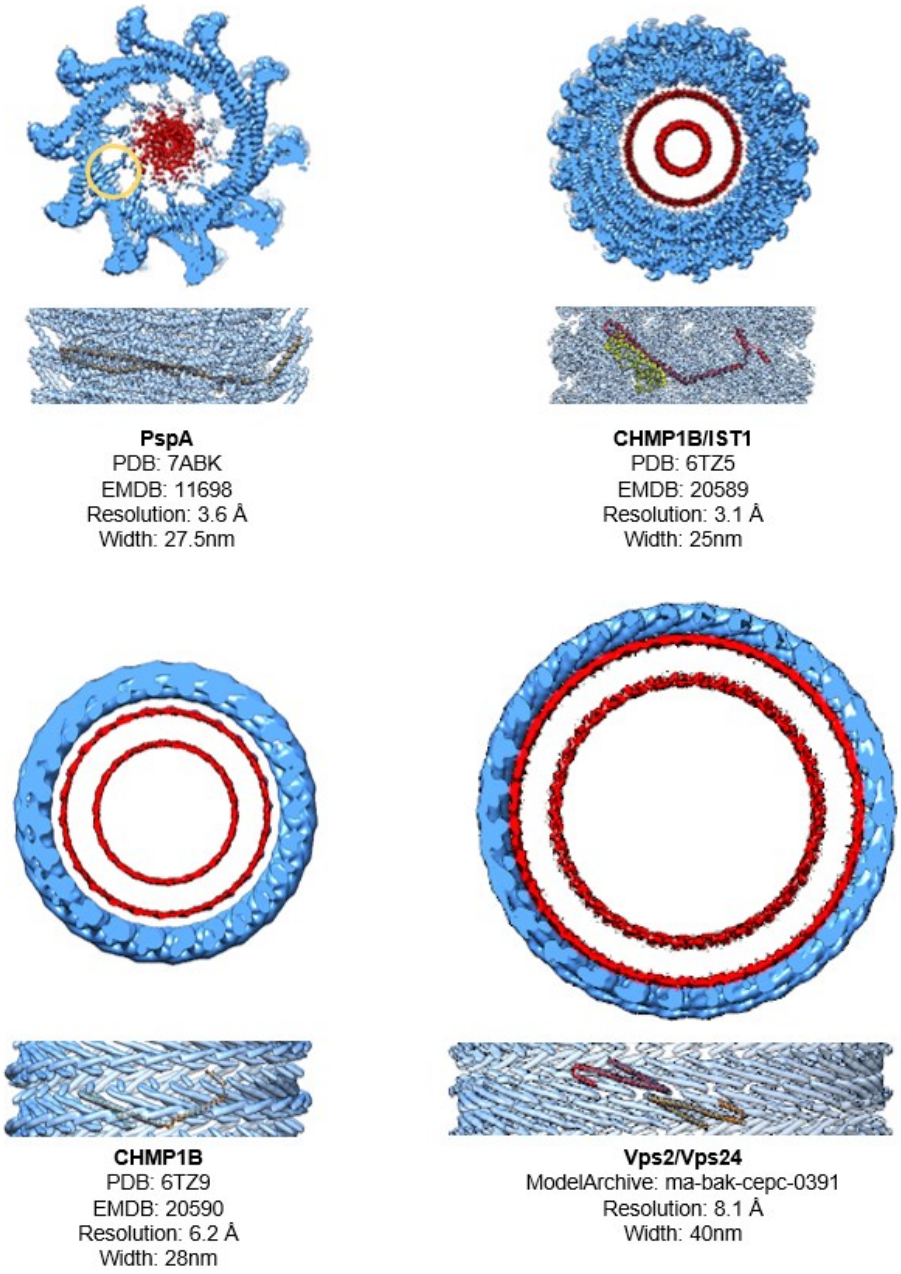

Figure 4.42: Comparison of structures of membrane remodeling complexes
The top and side views of the structures of PspA [158], CHMP1B [125], CHMP1B/IST1 [125] and Vps2ΔNC/Vps24 forming a protein coat around a membrane are shown. A single protein subunit is shown in orange for PspA and CHMP1B, while for the CHMP1B/IST1 complex, CHMP1B is shown in red and IST1 in yellow. The model fit into the Vps2ΔNC/Vps24 structure is that of Vps24 from [147], and truncated to show only residues 10-138. The membrane region is colored in red, while the protein coat is in blue. The PspA map shows density corresponding to helix α0 that protrudes into the lipid region (circled in yellow). All of the structures show helical symmetry with no additional point group symmetry, except for the Vps2ΔNC/Vps24 structure which shows D1 symmetry.

5 Materials and Methods

5.1 Cloning and generation of expression constructs

All of the proteins expressed and purified in this thesis were produced in *E. coli*. The bacterial expression constructs for full-length MBP-p62 was made by Dr. Abul Tarafder prior to my arrival in the lab. Expression constructs for full length Vps24 and MBP-Vps2 (10-166) were made by the lab of Dr. Roger Williams and generously shared with the lab prior to my arrival. The expression construct for Snf7 and MBP-Vps4 were ordered and synthesized by Genscript Biotech Corporation. To make the expression construct for GST-Vps20, the vector pET41b was then linearized using NcoI-HF (New England Biolabs cat# R3193S) and SalI-HF restriction enzymes (New England Biolabs cat# R3138S) using the manufacturer's protocol. The gene coding for Vps20 was synthesized as a double stranded gBlock fragment by Integrated DNA Technologies corporation along with 5' and 3' overhangs of 30bp each that have complementarity with the linearized vector. The gene and vector were assembled by Gibson assembly using the NEBuilder master mix (New England Biolabs, cat# E2621S) using the manufacturer's protocol. For all cloning purposes, NEB 5-α chemically competent cells (New England Biolabs cat# C2987H) were used for the transformation. All transformations were done by adding the DNA to 50µL aliquots of the cells, incubating for 30min on ice, followed by a 30s heat shock at 42 °C, after which the cells were diluted using 450µL of SOC media (New England Biolabs cat# B9020) and allowed to recover for 45min at 37 °C in a shaking incubator before being plated on LB-agar plates to grow at 37 °C overnight.

Construct name	Short name	Vector backbone	Selection marker	N-terminal tags	N-terminal tag removal	Insert	C-terminal tags	C-terminal tag removal
C125: pETM43-p62 FL	p62-FL	pETM43	Kanamycin	MBP	3C protease	human SQSTM1/p62 full length	6x His	-
C544: pMAL-C5x-scVps4	Vps4	pMAL-C5x	Ampicillin	MBP	TEV protease	full length Saccharomyces cerevisiae Vps4	6x His	TEV protease
C106: pOP547 scVps2 aa 10-166	Vps2	pOP547	Ampicillin	6x His, MBP	TEV protease	Saccharomyces cerevisiae Vps2, residues 10-166	-	-
C545: scVps20-pET41b	Vps20	pET41b	Kanamycin	GST, 6x His	TEV protease	full length Saccharomyces cerevisiae Vps20	-	-
C103: pOPTH scVps24	Vps24	pOPTH	Ampicillin	6x His	TEV protease	full length Saccharomyces cerevisiae Vps24	-	-
C565: pET30a-His-Snf7	Snf7	pET30a	Kanamycin	6x His	TEV protease	full length Saccharomyces cerevisiae Snf7	-	-

Figure 5.1: List of constructs used for bacterial protein expression

5.2 Protein expression and purification

5.2.1 Expression protocols:

All proteins were expressed in BL21 (DE3) chemically competent *E. coli* (New England Biolabs, cat# C2527H). After transformation of the cells with the target construct, using the same protocol as for the cells used for cloning, a single colony is picked from the plate. The colony is used for a 10mL starter culture of Terrific Broth media (MP Biomedicals, cat# 113046022-CF) supplanted with the selection antibiotic and grows overnight at 37 °C in a shaking incubator. The starter culture is then used to inoculate 500-1000mL of the main culture, also in Terrific broth media. The cells are grown to an OD600 of between 2 and 3. For SQSTM1/p62 and Vps4, the media is allowed to cool to 23 °C and induced using 1mM IPTG and left to incubate/shake overnight before being harvested by centrifugation at 6000 × *g* for 10 minutes, after which the pellet is frozen at -80 °C. For Vps24, Vps2ΔNC and Vps20,

after the main culture has reached OD600 of 2-3, the cells are induced with 1mM IPTG and left in the incubator/shaker at 37 °C for 3 hours before being harvested by centrifugation.

5.2.2 Purification of SQSTM1/p62

The cell pellet from 500mL of original culture volume is thawed in a room temperature water bath, resuspended in 50mL of Lysis buffer consisting of 20mM HEPES pH 8.0, 1000mM NaCl, 2.5mM $MgSO_4$, 10µM $ZnCl_2$, 0.5mM TCEP and 1x EDTA-free protease inhibitor cocktail (Thermo Fischer Scientific, cat# A32965). The cells are lysed using three passages through a microfluidizer at 1.5 Bar. The lysate is clarified by centrifugation at 30,000 × *g* for 30 minutes. The clarified lysate is then added to 5mL of Ni-NTA beads and allowed to incubate with gentle shaking for 30 minutes at 4 °C, after which the flowthrough is drained by gravity. The beads are washed sequentially with 5x 5mL of the lysis buffer, 5x 5mL of the lysis buffer with 10mM imidazole, and 5x 5mL of lysis buffer with 20mM imidazole. The protein is eluted with the lysis buffer with 300mM imidazole. The protein is then buffer exchanged either by dialysis or a desalting column into the lysis buffer, aliquoted and flash frozen.

For filament formation, the protein is thawed and concentrated to 2 mg/mL, and 1 1:5 mass ratio of 3C protease to protein is added. The sample is allowed to incubate at room temperature for 3 hours, and then moved to 4 °C overnight to remove the MBP tag. The following day, the filaments are isolated by centrifugation at 20,000 × *g* for 30 minutes and resuspended in either pH 6 buffer consisting of 50mM Sodium Acetate pH 6.0, 50mM NaCl, or pH 8 buffer consisting of 20mM HEPES pH 8.0, 50mM NaCl.

5.2.3 Purification of Vps2ΔNC, Vps4, Vps20, Vps24 and Snf7

The cell pellet corresponding to 500mL of original culture volume is thawed and resuspended in lysis buffer consisting of 20mM Tris-HCl pH 7.5, 300mM NaCl and 1x protease inhibitor cocktail, in the case of Vps4, an additional 2mM $MgCl_2$ is also included in all buffers. The cells are lysed by 3 passes at 1.5 Bar through a microfluidizer and the lysate is clarified by centrifugation at 30,000 × *g* for 30 minutes. The clarified lysate is then added to 5mL of Ni-NTA resin (or 5mL of Amylose resin for Vps2ΔNC) and incubated for 30 minutes

at 4 °C. The column is drained by gravity and the beads are washed with 5x 5mL of the lysis buffer with 10mM imidazole, followed by 5x 5mL of lysis buffer with 20mM imidazole (for Vps2ΔNC, only one wash consisting of 5x 5mL of lysis buffer without imidazole is performed). The protein is eluted from the beads in lysis buffer with 300mM imidazole and 0.5mM TCEP (for Vps2ΔNC, instead of 300mM imidazole, 25mM maltose is used).

A 1:10 mass ratio of TEV protease to protein is added for tag removal, and the sample is dialyzed overnight against lysis buffer to remove the imidazole and complete tag removal. The next day, the sample is loaded onto 2mL of Ni-NTA beads for the reverse nickel step. The sample is incubated with the beads for one hour at 4 °C, after which the flowthrough is drained and collected. The beads are washed with 3x 5mL of lysis buffer with 20mM imidazole. The uncleaved protein, contaminants, and protease are eluted from the column in lysis buffer with 300mM imidazole.

Following the reverse nickel step, the protein is divided into 5mL batches. Each batch is then centrifuged at 12,000 × g for 10 minutes and then injected onto a HiLoad 16/600 Superdex 75 pg size exclusion column (Cytiva, cat# 28989333) equilibrated with 20mM HEPES pH 8.0, 300mM NaCl (and 1mM $MgCl_2$ for Vps4).

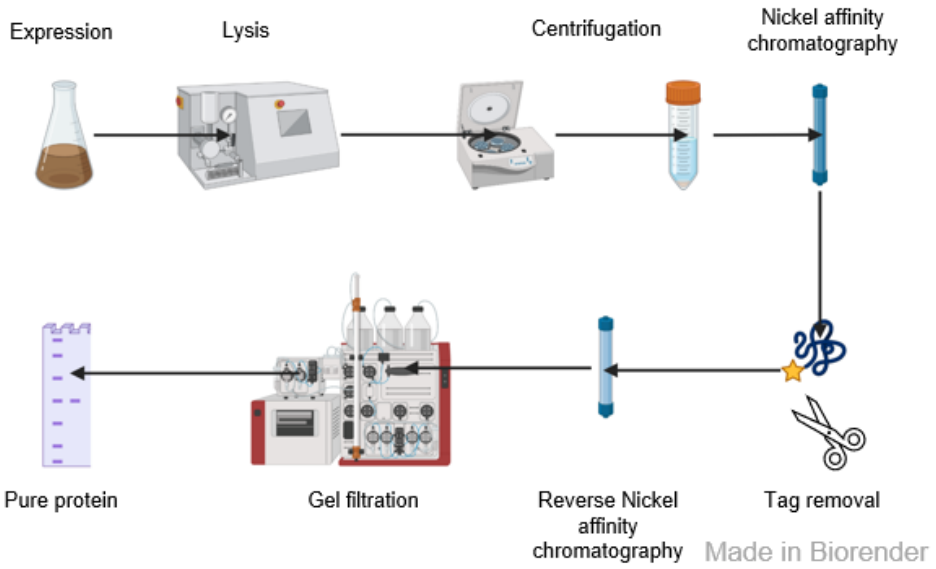

Figure 5.2: Protein purification strategy for ESCRT-III proteins
Following bacterial expression, the cells are lysed, cell debris is pelleted, and the soluble fraction is subjected to nickel affinity chromatography. Following elution of the protein bound to the resin, the protein tag is removed by protease digestion and the sample is subjected to a second round of nickel affinity chromatography in which the protease as, uncleaved protein and contaminants bind to the resin, while the protein of interest flows through the column. This relatively pure protein is loaded onto a gel filtration column for polishing and is then ready for use.

5.2.4 Other proteins used in this work

Several proteins that were purified by other lab members or acquired from other labs in purified form were used in this work. These are listed below in Figure 5.3.

Protein	Description	Source organism	Expression organism	Source
Vps24 Δ1-9	Vps24 lacking helix α0	*Saccharomyces cerevisiae*	*E. coli*	Roger Williams Lab
Vps24 K5D/K6D	Vps24 charge reversal mutant	*Saccharomyces cerevisiae*	*E. coli*	Roger Williams Lab
Vps24 K133D/E134A/K137D	Vps24 charge reversal mutant	*Saccharomyces cerevisiae*	*E. coli*	Roger Williams Lab
Ams1	Alphamannosidase-1	*Saccharomyces cerevisiae*	*Spodoptera frugiperda* (Insect cells)	Dr. Abul Tarafder
LC3b	high affinity mutant of LC3b (MAP1LC3B), I23A, Q26L mutation	*Homo sapiens sapiens*	*E. coli*	Dr. Audrey Guesdon

Figure 5.3: List of externally supplied proteins used in this work

5.3 Sample preparation for electron microscopy

In order to make grids for negative staining, 3.5µL of the sample is added to freshly glow discharged 300 mesh copper backed, carbon coated grids (Electron Microscopy Services, cat# CF300-Cu) and allowed to incubate for 30 seconds before being blotted away using Whatman paper. The grid is then dipped into 5µL of the sample buffer and blotted. This is repeated one more time. The grid is then dipped into 5µL of 2% uranyl acetate stain and blotted. The sample is again dipped into 5µL of 2% uranyl acetate stain and allowed to incubate for 1 minute before being blotted and allowed to dry. For negatively stained grid screening a Talos 120C (Thermo Fischer Scientific) electron microscope at 120 KeV is used. The sample is visualized either by the florescent screen or by a CETA CCD camera.

For preparation of vitrified specimens, 2-5µL of the protein sample is applied to a freshly glow discharged grid (glow discharging is skipped for graphene oxide grids) in a Vitrobot mark IV (Thermo Fischer Scientific). The sample chamber is maintained at 70-100% humidity and 4-10 °C. The sample is then automatically blotted for 2-6 seconds and plunged into liquid ethane or ethane/propane mixture. Screening and data collection for vitrified specimens was performed after clipping the grids and loading them on a Talos Arctica 200 KeV instrument (Thermo Fischer Scientific), equipped with a K3 direct electron detector camera and Quantum GIF filter (Gatan, Inc). Maps were rendered in UCSF Chimera [159] and atomic models in Pymol (Schrodinger LLC).

5.4 Protocols and materials for experiments involving lipids

5.4.1 Liposome/LUV preparation

In order to prepare liposomes, a lipid film is hydrated in a buffer solution. To prepare the film, 0.5mg of the appropriate lipid dissolved in 100µL of chloroform is slowly dried under nitrogen in a glass vial tilted at about 45° and slowly rotated. The semi-dry lipid film is then dried further under 100 mBar vacuum overnight. The lipid film is then resuspended in the appropriate buffer to a final concentration of 2 mg/mL, corresponding roughly to 3µM. Unless otherwise noted in the results section, the buffer used for this resuspension is 20mM Tris-HCl pH 7.5, 300mM NaCl. The resuspended lipids are then subjected to 8 freeze thaw cycles using liquid nitrogen and a 37 °C water bath. In order to produce LUVs, the liposome solution is then subjected to 21 cycles of extrusion against a 200nm membrane. The lipids used in this work were **DOPS** (Full name: 18:1 PS, Avanti cat# 840035), **YPL** (Full name: Yeast Polar Extract, Avanti Cat# 190001), **YTL** (Full name: Yeast Total Extract, Avanti cat# 190000), and **DOPC** (Full name 18:1 (Δ9-Cis) PC, Avanti cat# 850375). The lipids were received either as a solution in chloroform, or as powder that was subsequently dissolved in chloroform and stored.

5.4.2 LUV flotation and pelletation assay

For the flotation assays, 11.25µL of LUVs prepared in 20mM Tris-HCl pH 7.5, 100mM NaCl were mixed with 11.25µL of protein mixtures at 3 mg/mL per protein in the same buffer and allowed to incubate for one hour at room temperature. This mixture was then mixed with 22.5µL of 60% sucrose dissolved in the same buffer. From this mixture, 45uL was added to the bottom of a 250µL ultracentrifuge tube. On top of this layer, 56.25µL of 25% sucrose was slowly added. On top of that layer 11.25µL of the buffer was added. The samples were then spun at 174,000 × g for one hour using the minimum acceleration and deceleration speeds. The fractions were extracted using a thin pipette tip from the bottom of the tube, and consisted of 45µL for the bottom fraction, 45µL for the middle fraction and 22.5µL for the top fraction. The pellet was dissolved in 20µL of the buffer solution. The samples were then analyzed by SDS-PAGE.

For the pelletation assays, 25µL of the protein solution at 2 mg/mL was mixed with 25µL of LUV solution, both in the same buffer as above. The sample was then incubated for one hour at 4 °C, and subjected to centrifugation at 175,000 × *g* for one hour. The pellet was then resuspended in 25µL of buffer, and the pellet and supernatant were analyzed by SDS-PAGE.

6 References

[1] R. Khandia *et al.*, "A Comprehensive Review of Autophagy and Its Various Roles in Infectious, Non-Infectious, and Lifestyle Diseases: Current Knowledge and Prospects for Disease Prevention, Novel Drug Design, and Therapy," *Cells*, vol. 8, no. 7, p. 674, Jul. 2019, doi: 10.3390/cells8070674.

[2] A. Lilienbaum, "Relationship between the proteasomal system and autophagy," *Int J Biochem Mol Biol*, vol. 4, no. 1, pp. 1–26, Mar. 2013.

[3] W.-X. Ding and X.-M. Yin, "Sorting, recognition and activation of the misfolded protein degradation pathways through macroautophagy and the proteasome," *Autophagy*, vol. 4, no. 2, pp. 141–150, Feb. 2008, doi: 10.4161/auto.5190.

[4] K. Leyva-Paredes, N. S. Castrejón-Jiménez, H. IvánArrieta-Oliva, S. L. Baltierra-Uribe, and B. EstelaGarcía-Pérez, *Choosing Lunch: The Role of Selective Autophagy Adaptor Proteins*. IntechOpen, 2016. doi: 10.5772/63977.

[5] K. Okamoto, "Organellophagy: Eliminating cellular building blocks via selective autophagy," *J Cell Biol*, vol. 205, no. 4, pp. 435–445, May 2014, doi: 10.1083/jcb.201402054.

[6] Y. Wei, M. Liu, X. Li, J. Liu, and H. Li, "Origin of the Autophagosome Membrane in Mammals," *Biomed Res Int*, vol. 2018, p. 1012789, Sep. 2018, doi: 10.1155/2018/1012789.

[7] G. Zaffagnini and S. Martens, "Mechanisms of Selective Autophagy," *Journal of Molecular Biology*, vol. 428, no. 9, Part A, pp. 1714–1724, May 2016, doi: 10.1016/j.jmb.2016.02.004.

[8] K. Suzuki and Y. Ohsumi, "Current knowledge of the pre-autophagosomal structure (PAS)," *FEBS Letters*, vol. 584, no. 7, pp. 1280–1286, 2010, doi: 10.1016/j.febslet.2010.02.001.

[9] J. Moscat and M. T. Diaz-Meco, "p62 at the Crossroads of Autophagy, Apoptosis, and Cancer," *Cell*, vol. 137, no. 6, pp. 1001–1004, Jun. 2009, doi: 10.1016/j.cell.2009.05.023.

[10] R. Ciuffa *et al.*, "The selective autophagy receptor p62 forms a flexible filamentous helical scaffold," *Cell Rep*, vol. 11, no. 5, pp. 748–758, May 2015, doi: 10.1016/j.celrep.2015.03.062.

[11] B. Caramés, N. Taniguchi, S. Otsuki, F. J. Blanco, and M. Lotz, "Autophagy is a Protective Mechanism in Normal Cartilage and its Aging-related Loss is Linked with Cell Death and Osteoarthritis," *Arthritis Rheum*, vol. 62, no. 3, pp. 791–801, Mar. 2010, doi: 10.1002/art.27305.

[12] R. A. Nixon, "The role of autophagy in neurodegenerative disease," *Nat Med*, vol. 19, no. 8, pp. 983–997, Aug. 2013, doi: 10.1038/nm.3232.

[13] E. Turco and S. Martens, "Insights into autophagosome biogenesis from in vitro reconstitutions," *J Struct Biol*, vol. 196, no. 1, pp. 29–36, Oct. 2016, doi: 10.1016/j.jsb.2016.04.005.

[14] Y. Chen and D. J. Klionsky, "The regulation of autophagy – unanswered questions," *J Cell Sci*, vol. 124, no. 2, pp. 161–170, Jan. 2011, doi: 10.1242/jcs.064576.

[15] K. Suzuki, Y. Kubota, T. Sekito, and Y. Ohsumi, “Hierarchy of Atg proteins in pre-autophagosomal structure organization,” *Genes Cells*, vol. 12, no. 2, pp. 209–218, Feb. 2007, doi: 10.1111/j.1365-2443.2007.01050.x.

[16] R. L. Knorr, H. Nakatogawa, Y. Ohsumi, R. Lipowsky, T. Baumgart, and R. Dimova, “Membrane Morphology Is Actively Transformed by Covalent Binding of the Protein Atg8 to PE-Lipids,” *PLoS One*, vol. 9, no. 12, p. e115357, Dec. 2014, doi: 10.1371/journal.pone.0115357.

[17] H. Nakatogawa, K. Suzuki, Y. Kamada, and Y. Ohsumi, “Dynamics and diversity in autophagy mechanisms: lessons from yeast,” *Nat Rev Mol Cell Biol*, vol. 10, no. 7, Art. no. 7, Jul. 2009, doi: 10.1038/nrm2708.

[18] K. Matoba *et al.*, “Atg9 is a lipid scramblase that mediates autophagosomal membrane expansion,” *Nat Struct Mol Biol*, vol. 27, no. 12, pp. 1185–1193, Dec. 2020, doi: 10.1038/s41594-020-00518-w.

[19] W. R. Parrish, C. J. Stefan, and S. D. Emr, “Essential role for the myotubularin-related phosphatase Ymr1p and the synaptojanin-like phosphatases Sjl2p and Sjl3p in regulation of phosphatidylinositol 3-phosphate in yeast,” *Mol Biol Cell*, vol. 15, no. 8, pp. 3567–3579, Aug. 2004, doi: 10.1091/mbc.e04-03-0209.

[20] S. Baskaran, M. J. Ragusa, E. Boura, and J. H. Hurley, “Two-Site Recognition of Phosphatidylinositol 3-Phosphate by PROPPINs in Autophagy,” *Mol Cell*, vol. 47, no. 3, pp. 339–348, Aug. 2012, doi: 10.1016/j.molcel.2012.05.027.

[21] L. Juris, M. Montino, P. Rube, P. Schlotterhose, M. Thumm, and R. Krick, “PI3P binding by Atg21 organises Atg8 lipidation,” *EMBO J*, vol. 34, no. 7, pp. 955–973, Apr. 2015, doi: 10.15252/embj.201488957.

[22] T. Kotani, H. Kirisako, M. Koizumi, Y. Ohsumi, and H. Nakatogawa, “The Atg2-Atg18 complex tethers pre-autophagosomal membranes to the endoplasmic reticulum for autophagosome formation,” *Proc Natl Acad Sci U S A*, vol. 115, no. 41, pp. 10363–10368, Oct. 2018, doi: 10.1073/pnas.1806727115.

[23] I. Tanida *et al.*, “Apg7p/Cvt2p: A novel protein-activating enzyme essential for autophagy,” *Mol Biol Cell*, vol. 10, no. 5, pp. 1367–1379, May 1999, doi: 10.1091/mbc.10.5.1367.

[24] T. Shintani, N. Mizushima, Y. Ogawa, A. Matsuura, T. Noda, and Y. Ohsumi, “Apg10p, a novel protein-conjugating enzyme essential for autophagy in yeast,” *EMBO J*, vol. 18, no. 19, pp. 5234–5241, Oct. 1999, doi: 10.1093/emboj/18.19.5234.

[25] A. Kuma, N. Mizushima, N. Ishihara, and Y. Ohsumi, “Formation of the approximately 350-kDa Apg12-Apg5.Apg16 multimeric complex, mediated by Apg16 oligomerization, is essential for autophagy in yeast,” *J Biol Chem*, vol. 277, no. 21, pp. 18619–18625, May 2002, doi: 10.1074/jbc.M111889200.

[26] T. Hanada *et al.*, “The Atg12-Atg5 conjugate has a novel E3-like activity for protein lipidation in autophagy,” *J Biol Chem*, vol. 282, no. 52, pp. 37298–37302, Dec. 2007, doi: 10.1074/jbc.C700195200.

[27] A. Kaufmann, V. Beier, H. G. Franquelim, and T. Wollert, “Molecular mechanism of autophagic membrane-scaffold assembly and disassembly,” *Cell*, vol. 156, no. 3, pp. 469–481, Jan. 2014, doi: 10.1016/j.cell.2013.12.022.

[28] M. Fu, J. J. Nirschl, and E. L. F. Holzbaur, “LC3 Binding to the Scaffolding Protein JIP1 Regulates Processive Dynein-Driven Transport of Autophagosomes,” *Dev Cell*, vol. 29, no. 5, pp. 577–590, Jun. 2014, doi: 10.1016/j.devcel.2014.04.015.
[29] F. Zhou *et al.*, “Rab5-dependent autophagosome closure by ESCRT,” *Journal of Cell Biology*, vol. 218, no. 6, Apr. 2019, doi: 10.1083/jcb.201811173.
[30] F. Reggiori and C. Ungermann, “Autophagosome Maturation and Fusion,” *Journal of Molecular Biology*, vol. 429, no. 4, pp. 486–496, Feb. 2017, doi: 10.1016/j.jmb.2017.01.002.
[31] U. Nair *et al.*, “A role for Atg8-PE deconjugation in autophagosome biogenesis,” *Autophagy*, vol. 8, no. 5, pp. 780–793, May 2012, doi: 10.4161/auto.19385.
[32] E. Cebollero *et al.*, “Phosphatidylinositol-3-Phosphate Clearance Plays a Key Role in Autophagosome Completion,” *Current Biology*, vol. 22, no. 17, pp. 1545–1553, Sep. 2012, doi: 10.1016/j.cub.2012.06.029.
[33] J.-C. Farré, A. Burkenroad, S. F. Burnett, and S. Subramani, “Phosphorylation of mitophagy and pexophagy receptors coordinates their interaction with Atg8 and Atg11,” *EMBO Rep*, vol. 14, no. 5, pp. 441–449, May 2013, doi: 10.1038/embor.2013.40.
[34] K. Mochida *et al.*, “Receptor-mediated selective autophagy degrades the endoplasmic reticulum and the nucleus,” *Nature*, vol. 522, no. 7556, pp. 359–362, Jun. 2015, doi: 10.1038/nature14506.
[35] K. Okamoto, N. Kondo-Okamoto, and Y. Ohsumi, “Mitochondria-anchored receptor Atg32 mediates degradation of mitochondria via selective autophagy,” *Dev Cell*, vol. 17, no. 1, pp. 87–97, Jul. 2009, doi: 10.1016/j.devcel.2009.06.013.
[36] K. Suzuki, C. Kondo, M. Morimoto, and Y. Ohsumi, “Selective transport of alpha-mannosidase by autophagic pathways: identification of a novel receptor, Atg34p,” *J Biol Chem*, vol. 285, no. 39, pp. 30019–30025, Sep. 2010, doi: 10.1074/jbc.M110.143511.
[37] M. A. Lynch-Day and D. J. Klionsky, “The Cvt pathway as a model for selective autophagy,” *FEBS Lett*, vol. 584, no. 7, pp. 1359–1366, Apr. 2010, doi: 10.1016/j.febslet.2010.02.013.
[38] J.-C. Farré and S. Subramani, “Mechanistic insights into selective autophagy pathways: lessons from yeast,” *Nat Rev Mol Cell Biol*, vol. 17, no. 9, Art. no. 9, Sep. 2016, doi: 10.1038/nrm.2016.74.
[39] J. M. T. Hyttinen, M. Amadio, J. Viiri, A. Pascale, A. Salminen, and K. Kaarniranta, “Clearance of misfolded and aggregated proteins by aggrephagy and implications for aggregation diseases,” *Ageing Res Rev*, vol. 18, pp. 16–28, Nov. 2014, doi: 10.1016/j.arr.2014.07.002.
[40] S. M. Cloonan, H. C. Lam, S. W. Ryter, and A. M. Choi, “‘Ciliophagy’: The consumption of cilia components by autophagy,” *Autophagy*, vol. 10, no. 3, pp. 532–534, Mar. 2014, doi: 10.4161/auto.27641.
[41] R. O. Watson, P. S. Manzanillo, and J. S. Cox, “Extracellular M. tuberculosis DNA targets bacteria for autophagy by activating the host DNA-sensing pathway,” *Cell*, vol. 150, no. 4, pp. 803–815, Aug. 2012, doi: 10.1016/j.cell.2012.06.040.
[42] Z. Lipatova and N. Segev, “A Role for Macro-ER-Phagy in ER Quality Control,” *PLoS Genet*, vol. 11, no. 7, p. e1005390, Jul. 2015, doi: 10.1371/journal.pgen.1005390.

[43] T. Kanki, K. Furukawa, and S. Yamashita, “Mitophagy in yeast: Molecular mechanisms and physiological role,” *Biochim Biophys Acta*, vol. 1853, no. 10 Pt B, pp. 2756–2765, Oct. 2015, doi: 10.1016/j.bbamcr.2015.01.005.
[44] D. Mijaljica and R. J. Devenish, “Nucleophagy at a glance,” *J Cell Sci*, vol. 126, no. Pt 19, pp. 4325–4330, Oct. 2013, doi: 10.1242/jcs.133090.
[45] E. Deosaran *et al.*, “NBR1 acts as an autophagy receptor for peroxisomes,” *J Cell Sci*, vol. 126, no. Pt 4, pp. 939–952, Feb. 2013, doi: 10.1242/jcs.114819.
[46] G. A. Wyant *et al.*, “NUFIP1 is a ribosome receptor for starvation-induced ribophagy,” *Science*, vol. 360, no. 6390, pp. 751–758, May 2018, doi: 10.1126/science.aar2663.
[47] C. Bertipaglia *et al.*, “Higher-order assemblies of oligomeric cargo receptor complexes form the membrane scaffold of the Cvt vesicle,” *EMBO Rep*, vol. 17, no. 7, pp. 1044–1060, Jul. 2016, doi: 10.15252/embr.201541960.
[48] A. J. Jakobi *et al.*, “Structural basis of p62/SQSTM1 helical filaments and their role in cellular cargo uptake,” *Nat Commun*, vol. 11, no. 1, Art. no. 1, Jan. 2020, doi: 10.1038/s41467-020-14343-8.
[49] S. T. Huber, S. Mostafavi, S. A. Mortensen, and C. Sachse, “Structure and assembly of ESCRT-III helical Vps24 filaments,” *Sci Adv*, vol. 6, no. 34, p. eaba4897, Aug. 2020, doi: 10.1126/sciadv.aba4897.
[50] W. M. Henne, N. J. Buchkovich, and S. D. Emr, “The ESCRT Pathway,” *Developmental Cell*, vol. 21, no. 1, pp. 77–91, Jul. 2011, doi: 10.1016/j.devcel.2011.05.015.
[51] D. J. Katzmann, M. Babst, and S. D. Emr, “Ubiquitin-dependent sorting into the multivesicular body pathway requires the function of a conserved endosomal protein sorting complex, ESCRT-I,” *Cell*, vol. 106, no. 2, pp. 145–155, Jul. 2001, doi: 10.1016/s0092-8674(01)00434-2.
[52] R. C. Piper and D. J. Katzmann, “Biogenesis and Function of Multivesicular Bodies,” *Annu Rev Cell Dev Biol*, vol. 23, pp. 519–547, 2007, doi: 10.1146/annurev.cellbio.23.090506.123319.
[53] M. S. Bhutta, C. J. McInerny, and G. W. Gould, “ESCRT Function in Cytokinesis: Location, Dynamics and Regulation by Mitotic Kinases,” *Int J Mol Sci*, vol. 15, no. 12, pp. 21723–21739, Nov. 2014, doi: 10.3390/ijms151221723.
[54] A. J. Jimenez, P. Maiuri, J. Lafaurie-Janvore, S. Divoux, M. Piel, and F. Perez, “ESCRT machinery is required for plasma membrane repair,” *Science*, vol. 343, no. 6174, p. 1247136, Feb. 2014, doi: 10.1126/science.1247136.
[55] J. R. Mayers and A. Audhya, “Vesicle formation within endosomes: An ESCRT marks the spot,” *Commun Integr Biol*, vol. 5, no. 1, pp. 50–56, Jan. 2012, doi: 10.4161/cib.18208.
[56] A. L. Schuh and A. Audhya, “The ESCRT machinery: From the plasma membrane to endosomes and back again,” *Crit Rev Biochem Mol Biol*, vol. 49, no. 3, pp. 242–261, 2014, doi: 10.3109/10409238.2014.881777.
[57] B. Meng and A. M. L. Lever, “The Interplay between ESCRT and Viral Factors in the Enveloped Virus Life Cycle,” *Viruses*, vol. 13, no. 2, p. 324, Feb. 2021, doi: 10.3390/v13020324.
[58] C. Lefebvre, R. Legouis, and E. Culetto, “ESCRT and autophagies: Endosomal functions and beyond,” *Seminars in Cell & Developmental Biology*, vol. 74, pp. 21–28, Feb. 2018, doi: 10.1016/j.semcdb.2017.08.014.

[59] M. Vietri, M. Radulovic, and H. Stenmark, “The many functions of ESCRTs,” *Nat Rev Mol Cell Biol*, vol. 21, no. 1, Art. no. 1, Jan. 2020, doi: 10.1038/s41580-019-0177-4.
[60] J.-A. Lee, A. Beigneux, S. T. Ahmad, S. G. Young, and F.-B. Gao, “ESCRT-III Dysfunction Causes Autophagosome Accumulation and Neurodegeneration,” *Current Biology*, vol. 17, no. 18, pp. 1561–1567, Sep. 2007, doi: 10.1016/j.cub.2007.07.029.
[61] L. Reimer and H. Kohl, *Transmission electron microscopy: physics of image formation*, 5th ed. New York, NY: Springer, 2008.
[62] E. Nogales and S. H. W. Scheres, “Cryo-EM: A Unique Tool for the Visualization of Macromolecular Complexity,” *Molecular Cell*, vol. 58, no. 4, pp. 677–689, May 2015, doi: 10.1016/j.molcel.2015.02.019.
[63] K. S. Subramanian, *TEXTBOOK ON FUNDAMENTALS AND APPLICATIONS OF NANOTECHNOLOGY.* S.l.: DAYA PUB HOUSE, 2018.
[64] K. Naydenova *et al.*, “CryoEM at 100 keV: a demonstration and prospects,” *IUCrJ*, vol. 6, no. 6, Art. no. 6, Nov. 2019, doi: 10.1107/S2052252519012612.
[65] Z. L. Wang, *Elastic and inelastic scattering in electron diffraction and imaging*. New York: Plenum Press, 1995.
[66] J. Dubochet *et al.*, “Cryo-electron microscopy of vitrified specimens,” *Q Rev Biophys*, vol. 21, no. 2, pp. 129–228, May 1988, doi: 10.1017/s0033583500004297.
[67] S. G. Wolf, L. Houben, and M. Elbaum, “Cryo-scanning transmission electron tomography of vitrified cells,” *Nat Methods*, vol. 11, no. 4, pp. 423–428, Apr. 2014, doi: 10.1038/nmeth.2842.
[68] J. R. Harris, *Negative staining and cryoelectron microscopy: the thin film techniques*. Oxford: BIOS Scientific, 1997.
[69] R. Danev, H. Iijima, M. Matsuzaki, and S. Motoki, “Fast and accurate defocus modulation for improved tunability of cryo-EM experiments,” *IUCrJ*, vol. 7, no. 3, Art. no. 3, May 2020, doi: 10.1107/S205225252000408X.
[70] J. A. Mindell and N. Grigorieff, “Accurate determination of local defocus and specimen tilt in electron microscopy,” *Journal of Structural Biology*, vol. 142, no. 3, pp. 334–347, Jun. 2003, doi: 10.1016/S1047-8477(03)00069-8.
[71] Y. Cheng, N. Grigorieff, P. A. Penczek, and T. Walz, “A Primer to Single-Particle Cryo-Electron Microscopy,” *Cell*, vol. 161, no. 3, pp. 438–449, Apr. 2015, doi: 10.1016/j.cell.2015.03.050.
[72] V. Raimondi, A. Grinzato, V. Raimondi, and A. Grinzato, “A basic introduction to single particles cryo-electron microscopy,” *AIMSBPOA*, vol. 9, no. 1, Art. no. biophy-09-01-002, 2022, doi: 10.3934/biophy.2022002.
[73] K. H. Downing and R. M. Glaeser, “RESTORATION OF WEAK PHASE-CONTRAST IMAGES RECORDED WITH A HIGH DEGREE OF DEFOCUS: THE ‘TWIN IMAGE’ PROBLEM ASSOCIATED WITH CTF CORRECTION,” *Ultramicroscopy*, vol. 108, no. 9, pp. 921–928, Aug. 2008, doi: 10.1016/j.ultramic.2008.03.004.
[74] P. B. Rosenthal and R. Henderson, “Optimal Determination of Particle Orientation, Absolute Hand, and Contrast Loss in Single-particle Electron Cryomicroscopy,” *Journal of Molecular Biology*, vol. 333, no. 4, pp. 721–745, Oct. 2003, doi: 10.1016/j.jmb.2003.07.013.

[75] G. McMullan, S. Chen, R. Henderson, and A. R. Faruqi, “Detective quantum efficiency of electron area detectors in electron microscopy,” *Ultramicroscopy*, vol. 109, no. 9, pp. 1126–1143, Aug. 2009, doi: 10.1016/j.ultramic.2009.04.002.
[76] A. F. Brilot *et al.*, “Beam-induced motion of vitrified specimen on holey carbon film,” *J Struct Biol*, vol. 177, no. 3, pp. 630–637, Mar. 2012, doi: 10.1016/j.jsb.2012.02.003.
[77] A. Punjani, J. L. Rubinstein, D. J. Fleet, and M. A. Brubaker, “cryoSPARC: algorithms for rapid unsupervised cryo-EM structure determination,” *Nat Methods*, vol. 14, no. 3, Art. no. 3, Mar. 2017, doi: 10.1038/nmeth.4169.
[78] D. Tegunov and P. Cramer, “Real-time cryo-electron microscopy data preprocessing with Warp,” *Nat Methods*, vol. 16, no. 11, Art. no. 11, Nov. 2019, doi: 10.1038/s41592-019-0580-y.
[79] S. H. W. Scheres, “RELION: Implementation of a Bayesian approach to cryo-EM structure determination,” *Journal of Structural Biology*, vol. 180, no. 3, pp. 519–530, Dec. 2012, doi: 10.1016/j.jsb.2012.09.006.
[80] T. Wagner *et al.*, “SPHIRE-crYOLO is a fast and accurate fully automated particle picker for cryo-EM,” *Commun Biol*, vol. 2, no. 1, Art. no. 1, Jun. 2019, doi: 10.1038/s42003-019-0437-z.
[81] F. J. Sigworth, “Principles of cryo-EM single-particle image processing,” *Microscopy*, vol. 65, no. 1, pp. 57–67, Feb. 2016, doi: 10.1093/jmicro/dfv370.
[82] M. Serna, “Hands on Methods for High Resolution Cryo-Electron Microscopy Structures of Heterogeneous Macromolecular Complexes,” *Frontiers in Molecular Biosciences*, vol. 6, 2019, doi: 10.3389/fmolb.2019.00033.
[83] S. H. W. Scheres and S. Chen, “Prevention of overfitting in cryo-EM structure determination,” *Nat Methods*, vol. 9, no. 9, pp. 853–854, Sep. 2012, doi: 10.1038/nmeth.2115.
[84] C. Sachse, J. Z. Chen, P.-D. Coureux, M. E. Stroupe, M. Fändrich, and N. Grigorieff, “High-resolution electron microscopy of helical specimens: a fresh look at tobacco mosaic virus,” *J Mol Biol*, vol. 371, no. 3, pp. 812–835, Aug. 2007, doi: 10.1016/j.jmb.2007.05.088.
[85] M. P. M. H. Benoit, A. B. Asenjo, and H. Sosa, “Cryo-EM reveals the structural basis of microtubule depolymerization by kinesin-13s,” *Nat Commun*, vol. 9, no. 1, p. 1662, Apr. 2018, doi: 10.1038/s41467-018-04044-8.
[86] J. McCullough *et al.*, “Structure and membrane remodeling activity of ESCRT-III helical polymers,” *Science*, vol. 350, no. 6267, pp. 1548–1551, Dec. 2015, doi: 10.1126/science.aad8305.
[87] C. Sachse and C. Sachse, “Single-particle based helical reconstruction—how to make the most of real and Fourier space,” *AIMSBPOA*, vol. 2, no. 2, pp. 219–244, 2015, doi: 10.3934/biophy.2015.2.219.
[88] X. Zhang, “Python-based Helix Indexer: A graphical user interface program for finding symmetry of helical assembly through Fourier–Bessel indexing of electron microscopic data,” *Protein Science*, vol. 31, no. 1, pp. 107–117, 2022, doi: 10.1002/pro.4186.
[89] A. Desfosses, R. Ciuffa, I. Gutsche, and C. Sachse, “SPRING – An image processing package for single-particle based helical reconstruction from electron cryomicrographs,” *Journal*

of Structural Biology, vol. 185, no. 1, pp. 15–26, Jan. 2014, doi: 10.1016/j.jsb.2013.11.003.
[90] E. H. Egelman, "Ambiguities in helical reconstruction," *eLife*, vol. 3, p. e04969, Dec. 2014, doi: 10.7554/eLife.04969.
[91] S. He and S. H. W. Scheres, "Helical reconstruction in RELION," *Journal of Structural Biology*, vol. 198, no. 3, pp. 163–176, Jun. 2017, doi: 10.1016/j.jsb.2017.02.003.
[92] S. Berkamp, S. Mostafavi, and C. Sachse, "Structure and function of p62/SQSTM1 in the emerging framework of phase separation," *The FEBS Journal*, vol. 288, no. 24, pp. 6927–6941, 2021, doi: 10.1111/febs.15672.
[93] G. Bjørkøy *et al.*, "p62/SQSTM1 forms protein aggregates degraded by autophagy and has a protective effect on huntingtin-induced cell death," *J Cell Biol*, vol. 171, no. 4, pp. 603–614, Nov. 2005, doi: 10.1083/jcb.200507002.
[94] S. Sukseree *et al.*, "Filamentous Aggregation of Sequestosome-1/p62 in Brain Neurons and Neuroepithelial Cells upon Tyr-Cre-Mediated Deletion of the Autophagy Gene Atg7," *Mol Neurobiol*, vol. 55, no. 11, pp. 8425–8437, Nov. 2018, doi: 10.1007/s12035-018-0996-x.
[95] T. Lamark *et al.*, "Interaction codes within the family of mammalian Phox and Bem1p domain-containing proteins," *J Biol Chem*, vol. 278, no. 36, Art. no. 36, Sep. 2003, doi: 10.1074/jbc.M303221200.
[96] E. Itakura and N. Mizushima, "p62 targeting to the autophagosome formation site requires self-oligomerization but not LC3 binding," *J Cell Biol*, vol. 192, no. 1, pp. 17–27, Jan. 2011, doi: 10.1083/jcb.201009067.
[97] B. Carroll *et al.*, "Oxidation of SQSTM1/p62 mediates the link between redox state and protein homeostasis," *Nat Commun*, vol. 9, no. 1, p. 256, Jan. 2018, doi: 10.1038/s41467-017-02746-z.
[98] J. Teramachi *et al.*, "Blocking the ZZ Domain of Sequestosome1/p62 Suppresses Myeloma Growth and Osteoclast Formation In Vitro and Induces Dramatic Bone Formation in Myeloma-Bearing Bones In Vivo," *Leukemia*, vol. 30, no. 2, pp. 390–398, Feb. 2016, doi: 10.1038/leu.2015.229.
[99] Y. Zhang *et al.*, "ZZ-dependent regulation of p62/SQSTM1 in autophagy," *Nat Commun*, vol. 9, no. 1, Art. no. 1, Oct. 2018, doi: 10.1038/s41467-018-06878-8.
[100] R. Horos *et al.*, "The Small Non-coding Vault RNA1-1 Acts as a Riboregulator of Autophagy," *Cell*, vol. 176, no. 5, pp. 1054-1067.e12, Feb. 2019, doi: 10.1016/j.cell.2019.01.030.
[101] A. Duran *et al.*, "p62 is a key regulator of nutrient sensing in the mTORC1 pathway," *Mol Cell*, vol. 44, no. 1, pp. 134–146, Oct. 2011, doi: 10.1016/j.molcel.2011.06.038.
[102] A. Puissant, N. Fenouille, and P. Auberger, "When autophagy meets cancer through p62/SQSTM1," *Am J Cancer Res*, vol. 2, no. 4, pp. 397–413, Jun. 2012.
[103] L. Herhaus and I. Dikic, "Ubiquitin-induced phase separation of p62/SQSTM1," *Cell Research*, vol. 28, no. 4, Art. no. 4, Apr. 2018, doi: 10.1038/s41422-018-0030-x.
[104] G. Zaffagnini *et al.*, "p62 filaments capture and present ubiquitinated cargos for autophagy," *EMBO J*, vol. 37, no. 5, p. e98308, Mar. 2018, doi: 10.15252/embj.201798308.

[105] Å. B. Birgisdottir, T. Lamark, and T. Johansen, “The LIR motif - crucial for selective autophagy,” *J Cell Sci*, vol. 126, no. Pt 15, pp. 3237–3247, Aug. 2013, doi: 10.1242/jcs.126128.
[106] B. T. MacDonald, K. Tamai, and X. He, “Wnt/β-catenin signaling: components, mechanisms, and diseases,” *Dev Cell*, vol. 17, no. 1, pp. 9–26, Jul. 2009, doi: 10.1016/j.devcel.2009.06.016.
[107] Y. Katsuragi, Y. Ichimura, and M. Komatsu, “Regulation of the Keap1–Nrf2 pathway by p62/SQSTM1,” *Current Opinion in Toxicology*, vol. 1, pp. 54–61, Dec. 2016, doi: 10.1016/j.cotox.2016.09.005.
[108] R. A. Saxton and D. M. Sabatini, “mTOR Signaling in Growth, Metabolism, and Disease,” *Cell*, vol. 168, no. 6, pp. 960–976, Mar. 2017, doi: 10.1016/j.cell.2017.02.004.
[109] T. H. Lee *et al.*, “The Death Domain Kinase RIP1 Is Essential for Tumor Necrosis Factor Alpha Signaling to p38 Mitogen-Activated Protein Kinase,” *Mol Cell Biol*, vol. 23, no. 22, pp. 8377–8385, Nov. 2003, doi: 10.1128/MCB.23.22.8377-8385.2003.
[110] S. Jiang, J. B. Fagman, C. Chen, S. Alberti, and B. Liu, “Protein phase separation and its role in tumorigenesis,” *eLife*, vol. 9, p. e60264, Nov. 2020, doi: 10.7554/eLife.60264.
[111] I. B. Wilde, M. Brack, J. M. Winget, and T. Mayor, “Proteomic Characterization of Aggregating Proteins after the Inhibition of the Ubiquitin Proteasome System,” *J. Proteome Res.*, vol. 10, no. 3, pp. 1062–1072, Mar. 2011, doi: 10.1021/pr1008543.
[112] J.-A. Pan *et al.*, “TRIM21 ubiquitylates SQSTM1/p62 and suppresses protein sequestration to regulate redox homeostasis,” *Mol Cell*, vol. 61, no. 5, pp. 720–733, Mar. 2016, doi: 10.1016/j.molcel.2016.02.007.
[113] Z. You *et al.*, “Requirement for p62 acetylation in the aggregation of ubiquitylated proteins under nutrient stress,” *Nat Commun*, vol. 10, p. 5792, Dec. 2019, doi: 10.1038/s41467-019-13718-w.
[114] D. N. Mastronarde, “SerialEM: A Program for Automated Tilt Series Acquisition on Tecnai Microscopes Using Prediction of Specimen Position,” *Microscopy and Microanalysis*, vol. 9, no. S02, pp. 1182–1183, Aug. 2003, doi: 10.1017/S1431927603445911.
[115] A. Rohou and N. Grigorieff, “CTFFIND4: Fast and accurate defocus estimation from electron micrographs,” *Journal of Structural Biology*, vol. 192, no. 2, pp. 216–221, Nov. 2015, doi: 10.1016/j.jsb.2015.08.008.
[116] A. J. Jakobi *et al.*, “Structural basis of p62/SQSTM1 helical filaments and their role in cellular cargo uptake,” *Nat Commun*, vol. 11, no. 1, Art. no. 1, Jan. 2020, doi: 10.1038/s41467-020-14343-8.
[117] M. Beckers and C. Sachse, “Permutation testing of Fourier shell correlation for resolution estimation of cryo-EM maps,” *J Struct Biol*, vol. 212, no. 1, p. 107579, Oct. 2020, doi: 10.1016/j.jsb.2020.107579.
[118] Å. B. Birgisdottir, T. Lamark, and T. Johansen, “The LIR motif - crucial for selective autophagy,” *J Cell Sci*, vol. 126, no. Pt 15, Art. no. Pt 15, Aug. 2013, doi: 10.1242/jcs.126128.
[119] R. Horos *et al.*, “The Small Non-coding Vault RNA1-1 Acts as a Riboregulator of Autophagy,” *Cell*, vol. 176, no. 5, Art. no. 5, Feb. 2019, doi: 10.1016/j.cell.2019.01.030.

[120] Bright, Fisher, Rogowska, and Taylor, “Fluorescence ratio imaging microscopy: temporal and spatial measurements of cytoplasmic pH,” *J Cell Biol*, vol. 104, no. 4, pp. 1019–1033, Apr. 1987, doi: 10.1083/jcb.104.4.1019.
[121] D. H. Kwon, L. Kim, and H. K. Song, “pH-dependent regulation of SQSTM1/p62 during autophagy,” *Autophagy*, vol. 15, no. 1, pp. 180–181, Oct. 2018, doi: 10.1080/15548627.2018.1532264.
[122] R. J. Heath *et al.*, “RNF166 Determines Recruitment of Adaptor Proteins During Antibacterial Autophagy,” *Cell Rep*, vol. 17, no. 9, pp. 2183–2194, Nov. 2016, doi: 10.1016/j.celrep.2016.11.005.
[123] E. Itakura and N. Mizushima, “p62 targeting to the autophagosome formation site requires self-oligomerization but not LC3 binding,” *J Cell Biol*, vol. 192, no. 1, Art. no. 1, Jan. 2011, doi: 10.1083/jcb.201009067.
[124] O. Schmidt and D. Teis, “The ESCRT machinery,” *Curr Biol*, vol. 22, no. 4, pp. R116–R120, Feb. 2012, doi: 10.1016/j.cub.2012.01.028.
[125] H. C. Nguyen *et al.*, “Membrane constriction and thinning by sequential ESCRT-III polymerization,” *Nat Struct Mol Biol*, vol. 27, no. 4, pp. 392–399, Apr. 2020, doi: 10.1038/s41594-020-0404-x.
[126] P. Whitley, B. J. Reaves, M. Hashimoto, A. M. Riley, B. V. L. Potter, and G. D. Holman, “Identification of Mammalian Vps24p as an Effector of Phosphatidylinositol 3,5-Bisphosphate-dependent Endosome Compartmentalization *,” *Journal of Biological Chemistry*, vol. 278, no. 40, pp. 38786–38795, Oct. 2003, doi: 10.1074/jbc.M306864200.
[127] P. S. Bilodeau, J. L. Urbanowski, S. C. Winistorfer, and R. C. Piper, “The Vps27p Hse1p complex binds ubiquitin and mediates endosomal protein sorting,” *Nat Cell Biol*, vol. 4, no. 7, pp. 534–539, Jul. 2002, doi: 10.1038/ncb815.
[128] D. J. Katzmann, C. J. Stefan, M. Babst, and S. D. Emr, “Vps27 recruits ESCRT machinery to endosomes during MVB sorting,” *J Cell Biol*, vol. 162, no. 3, pp. 413–423, Aug. 2003, doi: 10.1083/jcb.200302136.
[129] P. S. Bilodeau, S. C. Winistorfer, W. R. Kearney, A. D. Robertson, and R. C. Piper, “Vps27-Hse1 and ESCRT-I complexes cooperate to increase efficiency of sorting ubiquitinated proteins at the endosome,” *J Cell Biol*, vol. 163, no. 2, pp. 237–243, Oct. 2003, doi: 10.1083/jcb.200305007.
[130] M. S. Kostelansky *et al.*, “Molecular Architecture and Functional Model of the Complete Yeast ESCRT-I Heterotetramer,” *Cell*, vol. 129, no. 3, pp. 485–498, May 2007, doi: 10.1016/j.cell.2007.03.016.
[131] T. Obita *et al.*, “Structural basis for selective recognition of ESCRT-III by the AAA ATPase Vps4,” *Nature*, vol. 449, no. 7163, Art. no. 7163, Oct. 2007, doi: 10.1038/nature06171.
[132] H. Teo *et al.*, “ESCRT-I Core and ESCRT-II GLUE Domain Structures Reveal Role for GLUE in Linking to ESCRT-I and Membranes,” *Cell*, vol. 125, no. 1, pp. 99–111, Apr. 2006, doi: 10.1016/j.cell.2006.01.047.
[133] H. Teo, O. Perisic, B. González, and R. L. Williams, “ESCRT-II, an Endosome-Associated Complex Required for Protein Sorting: Crystal Structure and Interactions with ESCRT-III and Membranes,” *Developmental Cell*, vol. 7, no. 4, pp. 559–569, Oct. 2004, doi: 10.1016/j.devcel.2004.09.003.

[134] M. A. Lemmon, K. M. Ferguson, and J. Schlessinger, “PH Domains: Diverse Sequences with a Common Fold Recruit Signaling Molecules to the Cell Surface,” *Cell*, vol. 85, no. 5, pp. 621–624, May 1996, doi: 10.1016/S0092-8674(00)81022-3.
[135] W. M. Henne, N. J. Buchkovich, Y. Zhao, and S. D. Emr, “The Endosomal Sorting Complex ESCRT-II Mediates the Assembly and Architecture of ESCRT-III Helices,” *Cell*, vol. 151, no. 2, Art. no. 2, Oct. 2012, doi: 10.1016/j.cell.2012.08.039.
[136] M. Alonso Y Adell, S. M. Migliano, and D. Teis, “ESCRT-III and Vps4: a dynamic multipurpose tool for membrane budding and scission,” *The FEBS Journal*, vol. 283, no. 18, pp. 3288–3302, 2016, doi: 10.1111/febs.13688.
[137] P. Horváth and T. Müller-Reichert, “A Structural View on ESCRT-Mediated Abscission,” *Frontiers in Cell and Developmental Biology*, vol. 8, 2020, doi: 10.3389/fcell.2020.586880.
[138] A.-K. Pfitzner, J. M. von Filseck, and A. Roux, “Principles of membrane remodeling by dynamic ESCRT-III polymers,” *Trends in Cell Biology*, vol. 31, no. 10, pp. 856–868, Oct. 2021, doi: 10.1016/j.tcb.2021.04.005.
[139] M. Babst, D. J. Katzmann, E. J. Estepa-Sabal, T. Meerloo, and S. D. Emr, “Escrt-III: An endosome-associated heterooligomeric protein complex required for mvb sorting,” *Developmental Cell*, vol. 3, no. 2, Art. no. 2, Aug. 2002, doi: 10.1016/S1534-5807(02)00220-4.
[140] D. Teis, S. Saksena, and S. D. Emr, “Ordered Assembly of the ESCRT-III Complex on Endosomes Is Required to Sequester Cargo during MVB Formation,” *Developmental Cell*, vol. 15, no. 4, pp. 578–589, Oct. 2008, doi: 10.1016/j.devcel.2008.08.013.
[141] S. Saksena, J. Wahlman, D. Teis, A. E. Johnson, and S. D. Emr, “Functional Reconstitution of ESCRT-III Assembly and Disassembly,” *Cell*, vol. 136, no. 1, pp. 97–109, Jan. 2009, doi: 10.1016/j.cell.2008.11.013.
[142] J. McCullough, A. Frost, and W. I. Sundquist, “Structures, Functions, and Dynamics of ESCRT-III/Vps4 Membrane Remodeling and Fission Complexes,” *Annual Review of Cell and Developmental Biology*, vol. 34, no. 1, pp. 85–109, 2018, doi: 10.1146/annurev-cellbio-100616-060600.
[143] S. Ghazi-Tabatabai *et al.*, “Structure and Disassembly of Filaments Formed by the ESCRT-III Subunit Vps24,” *Structure*, vol. 16, no. 9, pp. 1345–1356, Sep. 2008, doi: 10.1016/j.str.2008.06.010.
[144] N. J. Buchkovich, W. M. Henne, S. Tang, and S. D. Emr, “Essential N-Terminal Insertion Motif Anchors the ESCRT-III Filament during MVB Vesicle Formation,” *Developmental Cell*, vol. 27, no. 2, pp. 201–214, Oct. 2013, doi: 10.1016/j.devcel.2013.09.009.
[145] B. Sciskala and R. Kölling, “Interaction Maps of the Saccharomyces cerevisiae ESCRT-III Protein Snf7,” *Eukaryot Cell*, vol. 12, no. 11, Art. no. 11, Nov. 2013, doi: 10.1128/EC.00241-13.
[146] S. Tang *et al.*, “Structural basis for activation, assembly and membrane binding of ESCRT-III Snf7 filaments,” *eLife*, vol. 4, p. e12548, Dec. 2015, doi: 10.7554/eLife.12548.
[147] I. R. Humphreys *et al.*, “Computed structures of core eukaryotic protein complexes,” *Science*, vol. 374, no. 6573, p. eabm4805, Nov. 2021, doi: 10.1126/science.abm4805.
[148] M. Bajorek *et al.*, “Structural Basis for ESCRT-III Protein Autoinhibition,” *Nat Struct Mol Biol*, vol. 16, no. 7, pp. 754–762, Jul. 2009, doi: 10.1038/nsmb.1621.

[149] T. Muzioł *et al.*, “Structural Basis for Budding by the ESCRT-III Factor CHMP3,” *Developmental Cell*, vol. 10, no. 6, pp. 821–830, Jun. 2006, doi: 10.1016/j.devcel.2006.03.013.
[150] J. Xiao, X.-W. Chen, B. A. Davies, A. R. Saltiel, D. J. Katzmann, and Z. Xu, “Structural Basis of Ist1 Function and Ist1–Did2 Interaction in the Multivesicular Body Pathway and Cytokinesis,” *Mol Biol Cell*, vol. 20, no. 15, pp. 3514–3524, Aug. 2009, doi: 10.1091/mbc.E09-05-0403.
[151] N. Monroe, H. Han, P. S. Shen, W. I. Sundquist, and C. P. Hill, “Structural basis of protein translocation by the Vps4-Vta1 AAA ATPase,” *eLife*, vol. 6, p. e24487, doi: 10.7554/eLife.24487.
[152] B. Yang, G. Stjepanovic, Q. Shen, A. Martin, and J. H. Hurley, “Vps4 disassembles an ESCRT-III filament by global unfolding and processive translocation,” *Nat Struct Mol Biol*, vol. 22, no. 6, pp. 492–498, Jun. 2015, doi: 10.1038/nsmb.3015.
[153] B. E. Mierzwa *et al.*, “Dynamic subunit turnover in ESCRT-III assemblies is regulated by Vps4 to mediate membrane remodelling during cytokinesis,” *Nat Cell Biol*, vol. 19, no. 7, pp. 787–798, Jul. 2017, doi: 10.1038/ncb3559.
[154] M. Babst, B. Wendland, E. J. Estepa, and S. D. Emr, “The Vps4p AAA ATPase regulates membrane association of a Vps protein complex required for normal endosome function.,” *EMBO J*, vol. 17, no. 11, pp. 2982–2993, Jun. 1998, doi: 10.1093/emboj/17.11.2982.
[155] J. Moser von Filseck *et al.*, “Anisotropic ESCRT-III architecture governs helical membrane tube formation,” *Nat Commun*, vol. 11, no. 1, Art. no. 1, May 2020, doi: 10.1038/s41467-020-15327-4.
[156] J. Xiao, H. Xia, K. Yoshino-Koh, J. Zhou, and Z. Xu, “Structural Characterization of the ATPase Reaction Cycle of Endosomal AAA-Protein Vps4,” *J Mol Biol*, vol. 374, no. 3, pp. 655–670, Nov. 2007, doi: 10.1016/j.jmb.2007.09.067.
[157] X. Xu, A. Costa, and D. J. Burgess, “Protein encapsulation in unilamellar liposomes: high encapsulation efficiency and a novel technique to assess lipid-protein interaction,” *Pharm Res*, vol. 29, no. 7, Art. no. 7, Jul. 2012, doi: 10.1007/s11095-012-0720-x.
[158] B. Junglas *et al.*, “PspA adopts an ESCRT-III-like fold and remodels bacterial membranes,” *Cell*, vol. 184, no. 14, pp. 3674-3688.e18, Jul. 2021, doi: 10.1016/j.cell.2021.05.042.
[159] Pettersen EF, Goddard TD, Huang CC, Couch GS, Greenblatt DM, Meng EC, Ferrin TE. J “UCSF Chimera-a visualization system for exploratory research and analysis” *Comput Chem*. 2004 Oct;25(13):1605-12.